POLITECNICO
MILANO 1863

SCUOLA DI INGEGNERIA INDUSTRIALE
E DELL'INFORMAZIONE

Design of a MIMO SAR CubeSat Formation Flight Constellation for Maritime Surveillance

TESI DI LAUREA MAGISTRALE IN
SPACE ENGINEERING - INGENGERIA SPAZIALE

Author: **Lorcan Kelleher**

Student ID: 940255
Advisor: Prof. Andrea Monti-Guarnieri
Co-advisors: Dr. Davide Giudici
Academic Year: 2021-2022

This page is left intentionally blank.

Abstract

This paper covers the design of a constellation of CubeSat formation flights for Synthetic Aperture Radar surveillance of maritime traffic, leveraging developments in MIMO distributed SAR systems to achieve system performance and a high revisit rate. Additionally, multiple images can be generated of the same scene in slightly different times, enabling the identification and measures of moving targets (be them vehicles or sea currents), by along-track-interferometric approaches. These advantages are to be considered on top of the flexibility, robustness, and scalability common to distributed sensors formation. The design entails some challenges, such as the precise keeping of the inter-sensor distance of the formation along and across-track, and the design of the orbits for the constellations of formations to meet the observational requirements.

The design is conducted using a set performance baseline for individual satellites and a hypothetical set of requirements for minimum system performance, including an operational area of interest set as the Mediterranean Sea. The optimal formation size is investigated at a high level and specified required performance is determined. Following this, the optimal constellation required to achieve the specified minimum performance is conceived using a multi-objective genetic algorithm considering Walker pattern constellations.

The genetic algorithm focuses on system performance while also considering system cost; both monetarily and from a mission analysis point of view. Two separate configurations are considered in the formulation of the optimal solution; small swath and large swath strip map modes. Each configuration consists of a number of satellites in close formation flight in order to achieve the specified minimum performance. This investigation is performed under the assumption of a fixed pointing scan mode and a search mode, where the instrument can slew to the target. Once identified, the performance of solutions output by the genetic algorithm is examined across the target area. Finally, the lifetime of the constellation is investigated under several perturbations to assess constellation maintenance requirements.

Keywords: SAR, MIMO, Formation Flights, CubeSat, Constellation, Genetic Algorithm

This page is left intentionally blank.

Abstract

Questo documento presenta la progettazione di una costellazione di CubeSat che volano in formazione per la sorveglianza SAR del traffico marittimo, sfruttando gli sviluppi in sistemi distribuiti SAR MIMO per ottenere prestazioni di sistema e un alto rateo di rivisita. Inoltre, molteplici immagini della stessa scena possono essere generate in tempi leggermente diversi, permettendo l'identificazione e la misura di obiettivi in movimento (siano essi imbarcazioni o correnti marine), tramite approcci interferometrici along-track. Questi vantaggi devono essere considerati in aggiunta alla flessibilità, robustezza e scalabilità caratteristici di una formazione di sensori distribuiti. La progettazione comporta alcune sfide, come il mantenimento preciso della distanza tra sensori della la formazione along track e across track e la progettazione delle orbite per le costellazioni in formazione per soddisfare i requisiti di osservazione. La progettazione è condotta utilizzando una baseline di prestazioni impostata per i singoli satelliti e un ipotetico set di requisiti per le prestazioni minime del sistema, inclusa un'area operativa di interesse fissata come il Mar Mediterraneo. La dimensione ottimale della formazione è studiata ad alto livello e vengono determinate le prestazioni richieste. In seguito, la costellazione ottimale necessaria per raggiungere le prestazioni minime specificate è concepita utilizzando un algoritmo genetico multi-obiettivo che considera le costellazioni con uno schema Walker.

L'algoritmo genetico si concentra sulle prestazioni del sistema considerando anche il costo del sistema; sia finanziariamente che dal punto di vista dell'analisi della missione. Due configurazioni separate sono considerate nella formulazione della soluzione ottimale: a fascia stretta e larga e modalità di mappatura a strisce. Ogni configurazione consiste in un numero di satelliti in formazione stretta al fine di raggiungere le prestazioni minime specificate. Questa indagine è performata sotto l'ipotesi di una modalità di scansione a puntamento fisso e una modalità di ricerca, dove lo strumento può ruotare verso il bersaglio. Una volta identificate, le prestazioni delle soluzioni prodotte dall'algoritmo genetico vengono esaminate attraverso l'area obiettivo. Infine, la vita utile della costellazione è studiata con diverse perturbazioni per valutare i requisiti di mantenimento dell'orbita della costellazione.

Parole Chiave: SAR, MIMO, Voli di Formazione, CubeSat, Constellazioni, Algoritmo Genetico

Contents

Symbols & Acronyms

List of Symbols

P_R	Power received (W)
σ	Radar cross section (m^2)
A_e	Antenna effective area (m^2)
P_{Tpeak}	Peak transmitted power (W)
$P_{Tpeak,SIMO}$	Peak transmitted power in SIMO operating mode (W)
$P_{Tpeak,MIMO}$	Peak transmitted power in MIMO operating mode (W)
$P_N MIMO$	Noise power in MIMO operating mode (W)
$A_e SIMO$	Antenna effective area in SIMO operating mode (m^2)
$A_e MIMO$	Antenna effective area in MIMO operating mode (m^2)
N	Number of satellites in formation
η	Antenna efficiency
L_z	Antenna height (m)
L_x	Antenna length (m)
G	Antenna gain
λ	Wavelength (m)
P_T	Transmitted power (W)
SNR_{min}	Minimum acceptable signal-to-noise ratio
P_{Noise}	System noise power (W)
R	Range to target (m)
L	Total system losses
L_{ins}	Instrument losses (dB)
L_{misc}	Miscellaneous losses due to antenna alignment, radiation patterns etc.
ω_{ES}	Angular velocity of the Earth around the Sun
a	Semi-major axis (km)
e	Orbit eccentricity
i	Orbit inclination (deg)
Ω	Orbit right ascension (deg)
$\Delta\Omega$	Change in orbit right ascension over set time (deg)
Φ_{max}	Maximum latitude reached by antenna beam (deg)
	Beam central angle (rad)

γ	Central angle of antenna beamwidth (rad)
δ	Central angle of antenna nearside beam edge (rad)
ω	Orbit argument of perigee (deg)
θ	True anomaly (deg)
σ_q	Scene height dispersion (m)
$\sigma_x t$	Across track accuracy (m)
$\sigma_a t$	Along-track accuracy (m)
δ_x	Along-track sampling interval (m)
$L_{clutter}$	Losses due to ocean clutter (dB)
T	Number of satellites in Walker constellation
P	Number of planes in Walker constellation
F	Phasing constant of Walker constellation
θ_z	Elevation beamwidth (rad)
ΔV	Spacecraft delta-v available (m/s)
ρ	Atmospheric density (kg/m^3)
α_{J2}	Acceleration due to J2 (km/s^2)
α_D	Acceleration due to drag (km/s^2)
z	Orbital z position in ECI frame (km)
y	Orbital y position in ECI frame (km)
x	Orbital z position in ECI frame (km)
r	Orbital radius in ECI frame (km)
v_{rel}	Relative velocity (km/s)
C_D	Drag coefficient
A	Satellite cross-sectional area for drag computation (m^2)
m_{sat}	Satellite mass (kg)
v_{vessel}	Vessel surface velocity (m/s)
t	Simulation time (s)
L_a	Antenna length (m)
N_r	Number of ambiguities
A_{cov}	Area covered (%)
α	Local terrain elevation (deg)

List of Acryonyms

SIMO	Single-Input Multi-Output
MIMO	Multi-Input Mulit-Output
PSD	Power Spectral Density
PRF	Pulse Repetition Frequency
PRI	Pulse Repetition Interval
SISO	Single-Input Single-Output
AO	Area of Operations
U	Units (CubeSat standard unit of measurement
RX	Receiver
TX	Transmitter
SAR	Synthetic Aperture Radar
RCS	Radar Cross Section
PID	Positive Identification
CHIRP	Concentrated High Intensity Radiation Pulse
MOGA	Multi-Objective Genetic Algorithm
SNR	Signal-to-Noise Ratio
CMWS	CubeSat MIMO Wide Swath
PU	Pattern Units
TLE	Two-Line Elements
Std	Standard deviation
GMAT	General Mission Analysis Tool
AIS	Automatic Identification System
COTS	Commercial Off-The-Shelf

List of Constants

c	Speed of light in vacuum	$299792458\ m/s$
R_E	Average radius of the Earth	$6371\ km$
K	Boltzmann Constant	$1.3807\text{e-}23\ m^2kgs^{-2}K^{-1}$
T_0	Noise Reference Temperature	290 K
J_2	J_2 Constant	0.0010826
μ_E	Gravitational parameter of the Earth	$3.98600\text{e}14\ \text{m}^3s^-2$
J_2	Earth J2 parameter	1.018e-3

List of Tables

List of Figures

1   Introduction

Compact SIMO and MIMO SAR formations have become more topical in literature as of late[1] [2] [3]. Benefits of these formations over single-platform SAR systems include a potential gain in swath size proportional to the number of satellites due to N-1 ambiguities being suppressed, and a signal-to-noise ratio gain up to N^2 [2]. The distributed nature of the systems of formation flights also offer benefits in redundancy and scalability, alongside potential reductions in costs. All of these benefits are useful in maritime tracking applications, where wide swaths of ocean can be scanned quickly and individual vessels identified from high-resolution imagery[4].

While constellation design for regional fisheries surveillance or global radar coverage is a documented [5] [6], design of a constellation leveraging MIMO CubeSat formations is a sparsely covered topic. Generally, constellation design is a topic approached using a genetic algorithm of some sort [7] [8] [6] as the search space considered is quite large. Genetic algorithms are a class of optimisation methods which are based on Darwin's natural genetic selection. Optimisations from weighted sum approaches using single genetic algorithms to multi-objective genetic algorithms have been used for this application of constellation design. Usually, a simplification in the constellation structure is required to reduce the search space. Constellation patterns such as the Walker Delta and Star [9] and streets-of-coverage patterns are usually used for exploring global and regional coverage respectively. In preliminary designs, often less accurate methods of performance analysis are accepted in exchange for simplification of the design problem. These simplifications may include the use of semi-analytical methods [10] for example, to increase computational efficiency when simulating performance. In this work some simplifications were be made based on the nature of the design problem posed, but an effort to maintain a more accurate visualisation of constellation performance was made at the expense of some computational performance.

After surveying similar products and hardware currently available on the market, a set of performance requirements were generated for both the constellation performance and the spacecraft populating the constellations used in this design. These requirements were used as constraints in the genetic algorithm and for the individual formation design, as well as to assess the best individuals generated by the genetic algorithm. Finally, the lifetime of the satellites in each formation was also investigated to assess requirements for constellation maintenance due to orbit degradation. Spacecraft were assumed to have a propulsion system on board with a limited amount of delta-v to perform manoeuvres. Using NASA's GMAT, the operational lifetime of the formations of different constellation solutions could be assessed. This was done to give a full picture as to the implications of operating any of the constellations proposed in the solutions to the design problem.

2 Background Information

2.1 Resolution vs Swath Size: The SAR Paradox

Synthetic aperture radar is a powerful remote sensing tool, but like all tools it has innate limitations. The specific limitation of interest for this work is that it is impossible to achieve an arbitrarily wide swath, with an arbitrarily fine azimuth resolution [11]. This is because in order to avoid aliasing (and thus azimuth ambiguities) the pulse repetition frequency must exceed the doppler bandwidth (the frequencies produced as a result of the scatters falling in the beamwidth of the instrument). This limitation arises from the sampling theorem of Nyquist-Shannon[12]. In essence, the time between emitted radar pulses must exceed the time required to recover the echoes from the imaged swath otherwise the image will contain azimuth ambiguities [13].

2.2 Tackling the SAR Paradox with CubeSats

There have been many proposed solutions to tackle the issue of wide-swath SAR imaging at high resolution, such as that posed by Bordoni et. al [14] or Krieger et. al [15]. Many of these solutions focus on monostatic configurations [16] [17]. Given the typical power, space and cost constraints associated with traditional SAR missions this was no surprise. However, recent developments in hardware miniaturisation and efficiency have resulted in the ability to mount SAR payloads on small satellites or more specifically CubeSats. Relaxing the financial constraints on mission hardware facilitates a new approach to wide-swath high-resolution imaging through SIMO or MIMO CubeSat constellations.

At a fixed resolution, a formation flight of CubeSats can image a number of areas along a set look angle interval. Stitching these images together would achieve the wide-swath required while maintaining the desired resolution in azimuth and suppressing ambiguities. There are a number of challenges with this approach, the least of which is the close formation flight of the spacecraft themselves and the collision risk they pose to each other and other spacecraft. However, the benefits of overcoming the SAR paradox would certainly justify the added effort in overcoming these challenges.

2.3 SIMO vs MIMO operating modes

Given the distributed nature of the instrument used in the proposed formation flight, two primary operating modes must be explored to identify the best performing configuration: SIMO and MIMO.

For this preliminary design and sizing of the system, the focus was only on the energy balance and the benefits and drawbacks of each operating mode were solely evaluated on the results of that analysis.

Starting from the radar equation for a SISO system, the power received at the monostatic radar can be expressed as seen in equation 1.

$$P_R = \frac{P_T \sigma G A_e L^2}{(4\pi R^2)^2} \tag{1}$$

The effective area of the radar antenna can be expressed as in equation 2.

$$Ae = \frac{G\lambda^2}{4\pi} \tag{2}$$

Similarly, the SNR at the receiver can be expressed as in equation 3.

$$SNR = \frac{P_R}{P_{Noise}} \tag{3}$$

For an imposed minimum SNR_{min} the peak transmitted power can be calculated combining 3, 2 and 1.

$$P_{T_{peak}} = \frac{SNR_{min}P_{Noise}4\pi^3R^4}{G^2\sigma\lambda^2L^2} \tag{4}$$

At this point, the assumption that the satellites in formation operate as a single monolithic satellite was made for the purpose of evaluating the energy balance. For the SIMO case, this resulted in the following parameters being modified:

- $A_{eSIMO} = A_e * N$

Modifying 4 with the corresponding SIMO parameters the peak power for the SIMO system becomes that of equation 5.

$$P_{T_{peak,SIMO}} = \frac{SNR_{min}P_{Noise}4\pi^3R^4}{G^2\sigma\lambda^2L^2} \tag{5}$$

Similarly for the MIMO case where all satellites are broadcasting and receiving simultaneously, the following parameters must be modified:

- $P_{NMIMO} = P_N * N$ (all satellites are active)

- $A_{eMIMO} = A_e * N$ (all satellites are receiving)

Again, inserting the modified terms into 4 it can be seen that for the same output power, the SNR improves by a factor N. Alternatively, seen from the transmitted power point of view, for a set minimum required SNR the required peak power transmitted is reduced by a factor of N.

$$P_{T_{peak,MIMO}} = \frac{SNR_{min}P_{Noise}4\pi^3R^4}{G^2\sigma\lambda^2L^2N} \tag{6}$$

2.4   Additional MIMO Operation Benefits

2.4.1   Reduced PRF and Ambiguity Suppression

As per Giudici et. al [2] formation flight under MIMO operation mode allows for N-1 ambiguities to be suppressed due to multi-sampling. This subsequently enables a lower PRF than would otherwise be necessary for a single monostatic SAR solution. The PRF required for unambiguous reception for a monostatic solution is that shown in equation 7.

$$PRF = \frac{2v}{N\Delta x} \tag{7}$$

Subsequently, the optimal sampling in the along-track direction for the MIMO configuration is shown in equation 8 [**Aguttes.J-P.**], [18].

$$x_m(r) = m * \delta_x + r * 2\frac{\delta_x}{N_r}$$
$$r = 0, ..., N_r - 1 \tag{8}$$

Here, m is an integer number. The sensor positions themselves can be at any multiple of La/2 displaced from each other in the along-track direction. Displacement must be of an integer number of La/2 to avoid aliasing [11] and must be tightly controlled. The tight control is required to maintain azimuth ambiguity suppression [2] in the MIMO case.

2.4.2   Redundancy

A higher level system benefit of MIMO operation is that of redundancy. If a spacecraft in the formation were to experience a malfunction or be destroyed, the remaining spacecraft in the formation could continue to operate albeit at a reduced performance with respect to the nominal imaging product. The malfunctioning spacecraft would also be cheaper and easier to replace as it makes up only part of the formation. While this possibility of continued imaging operation would be possible in larger formations, it would be less possible within smaller MIMO formations. This is due to the likelihood of destructive interference between formation instruments for formations of N=2 [2]. As a result, any malfunction in a formation of 3 spacecraft would mean that imaging operations would have to cease.

In the case where multiple formations of 3 make up part of a wide-swath imaging train, cessation of imaging operations for one formation would obviously imply a reduced swath which could be imaged. However, with this reduced swath the imaging resolution would not have to be reduced to compensate for the loss of the formation from the imaging train. This represents an additional layer of redundancy within larger imaging trains, beyond the simple MIMO formation redundancy previously discussed.

Regardless of formation size the distributed system nature of the formation implies a significantly lower replacement cost for a system failure. The cost of manufacture and launch of a single CubeSat for a MIMO formation is far exceeded by the cost of a monolithic system with equivalent formation performance. This is obvious due to the enormous mass and size differences, along with a reduced ability to leverage COTS components in the proposed solution.

3 Spacecraft Concept of Operations

3.1 Target Information

As the purpose of this constellation is maritime surveillance, the constellation should be capable of monitoring vessels which are of interest to this objective. For the purposes of fisheries protection, humanitarian purposes, search and rescue and defense, the vessel category of interest is generally coasters. Coasters generally operate close to the shore in domestic waters. As per Menon [19], coasters consist of fishing trawlers, trading vessels and pleasure craft. Miller et. al [20] suggests that significant illegal fishing and human or drugs trafficking is conducted by vessels of these types. From a defense standpoint, modern navies of countries such as the US [21], India [22] and Russia [23] are all moving to smaller multi-role corvette-class vessels for their next generation of vessels. The smallest of modern corvettes falls into the coaster classification, and anything larger should be easily identified by a system that was designed to identify corvettes. For this design, the radar cross-section (RCS) of vessels was obtained from Williams et. al [24]. This information can be seen in table 1. RCS values for coasters range from 40 - 16,000 m^2 for this class. This RCS range was therefore used for sizing the individual CubeSat formations and assessing their feasibility for acquisition and tracking of vessels.

Target Ship			RCS	
Type	**Overall length (m)**	**Gross Tonnage (Tons)**	**Approx. Min. RCS (m^2)**	**Approx. Max. RCS (m^2)**
Inshore fishing vessel	9	5	3	10
Small coaster	40-46	200-250	20	800
Coaster	55	500	40	2000
Coaster	55	500	300	4000
Coaster	57	500	1000	16000
Large coaster	67	836-1000	1000	5000
Collier	73	1570	300	2000
Warship (frigate)	103	2000	5000	100000
Cargo liner	114	5000	10000	16000
Cargo liner	137	8000	4000	16000
Bulk carrier	167	8200	400	10000
Cargo	153	9400	1600	12500
Cargo	166	10430	400	16000
Bulk carrier	198	15000-20000	1000	32000
Ore carrier	206	25400	2000	25000
Container carrier	212	26436	10000	80000
Medium tanker	213-229	30000-35000	5000	80000
Medium tanker	251	44700	16000	1600000

Table 1: Radar cross sections by vessel class

3.1.1   Target Area

The target area for testing was set as the Mediterranean Sea. The Mediterranean has been a hotspot for humanitarian [25] [26], fisheries monitoring [27] [28] and defense [29] [30] activity in particular in recent years. This would make it a particularly useful area to monitor for maritime surveillance reasons. This target area was set up by retrieving the latitude and longitude coordinates of 42 cities on the coast of the Mediterranean and creating a 2D convex hull using the stereographic projection of the coordinates, as shown in figure 1. The target area considered was calculated to span 2.4522e6 km^2 in total.
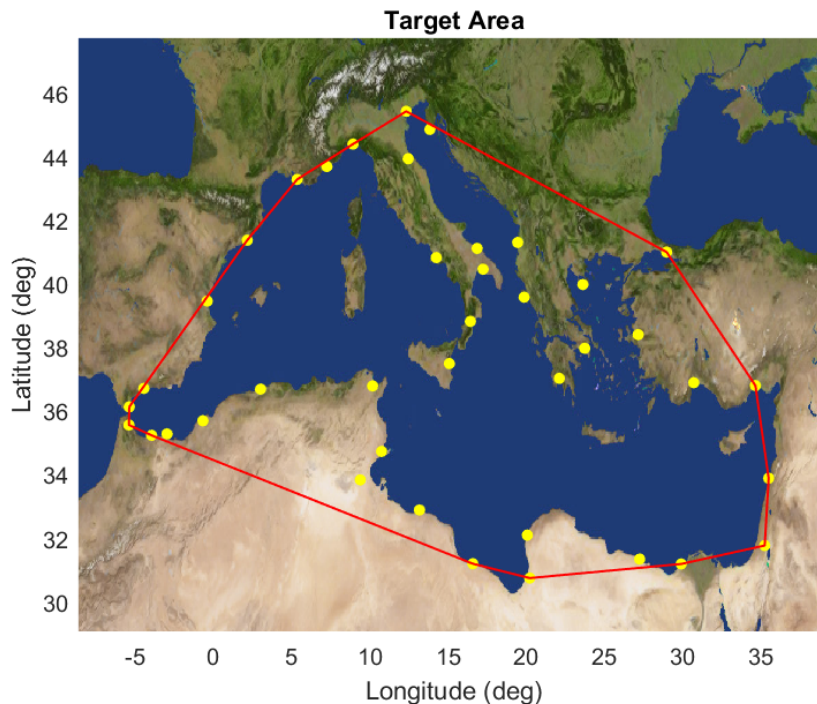
Figure 1: Plot of the target area, the Mediterranean Sea with major cities used to make the convex hull

3.2   Operating Modes

Generally speaking, spacecraft hosting SAR instruments consider their imaging revisit rate differently to their point revisit rate (ground track repeat cycle) due to the ability of the instrument to slew between elevation angles. It was assumed for the sake of this design that the CubeSat hosting the instrument was capable of full 3-axis stabilisation and control and so would be capable of manoeuvring to point its antenna throughout the selected elevation range. However, assuming that the antenna will be larger in area than the CubeSat bus itself when it is deployed it would increase the moment of inertia of the spacecraft considerably. This would make the spacecraft harder to point, especially under the effects of orbital perturbations. Pointing would be required for imaging because as a simplifying assumption, the spacecraft antenna in this design was not assumed to be a phased-array antenna. Whole-spacecraft manoeuvring to perform re-pointing was deemed to be necessary but was sought to be minimised if possible. For this reason, two operating modes were envisaged:

1. A single fixed look angle (referred to as fixed scanning or scan mode from this point on)

2. A variable pointing mode (referred to as search mode from this point on).

The scan mode assumes that a target is not assigned, and the instrument is passively scanning the surface of the Earth at a fixed nominal look angle. This was foreseen to be the nominal operating mode for a maritime surveillance constellation.

The search mode assumes that a specific known location must be imaged, and any pointing in the range of look angles can be achieved, such that the spacecraft can slew to ensure that location is in view of the instrument. In both operating modes, stripmap imaging is performed, with the sensor recording the image pushbroom-style.

3.3   Formation Configurations

To illustrate the benefits of the wide-swath high-resolution imaging for this application, 2 formation types were considered. Firstly, a single formation configuration was explored. This consisted of a constellation made up of formations using the minimum number of spacecraft required to achieve the baseline performance specified. Following this, a configuration was investigated where a number of formations from the first configuration were assumed to fly in formation imaging different areas on the ground to achieve the required performance. This was designated as CubeSat MIMO wide-swath (CMWS) configuration. In all cases, the spacecraft were assumed to fly in a single-file SAR train as per Agguttes [31] following one another so as to be on approximately the same orbit and experience more or less the same orbit degradation by orbital perturbations. This is similar to the multi-beam squinted SAR concept discussed by Krieger et. al [32]. These configurations are summarised in figures 2 and 3 respectively. Despite the misalignment of the spacecraft in the orbit velocity direction, for the CMWS mode it was assumed that the formations imaged the same area such that the difference in acquisition time associated with figure 3 could be neglected.
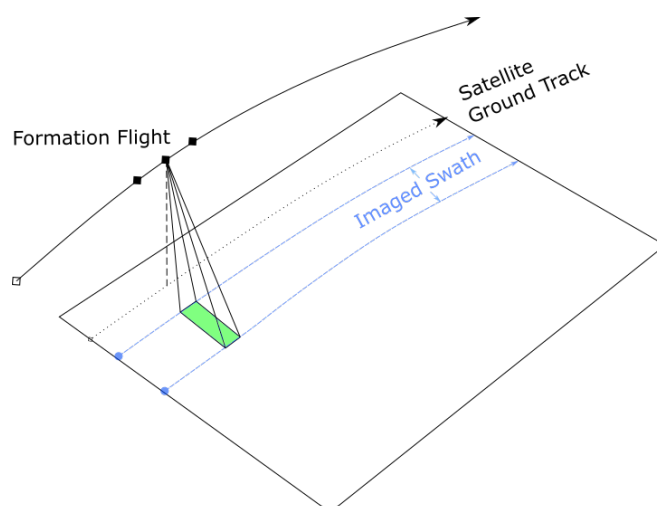
Figure 2: Single train formation flight
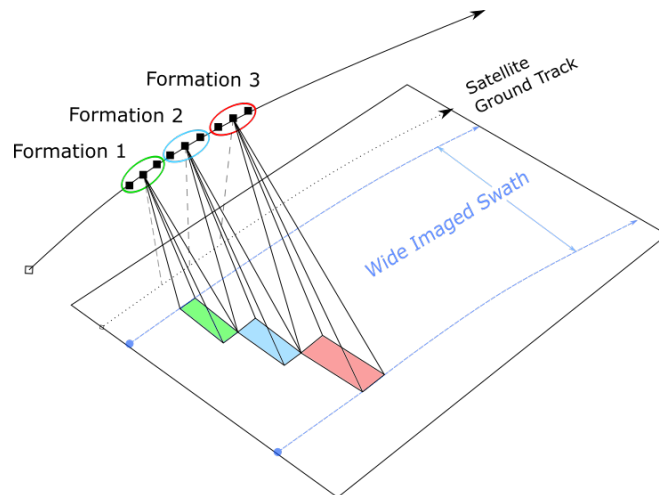
Figure 3: CMWS formation flight

4 Baseline Requirements

4.1 Performance Survey

Several government institutions and private companies offer solutions to high-resolution SAR and/or maritime surveillance via specific SAR products. The Sentinel missions, in addition to Capella X-SAR and ICEYE are among the most high profile of these offerings. To specify the minimum performances of the system, this state of the art was examined and multiple products compared keeping in mind the possible restrictions of the CubeSat form factor on system performance. This was done by accounting for performance differences from newer existing products by means of a set system margin of 20-30% as per ECSS and NASA Ames standards [33] [34]. This said, a SAR CubeSat system has yet to fly and so some parameters were chosen on the basis of educated best-guess and missions that are in development like SRI-CIRES [35]. This philosophy was deemed sufficient for this design process as the exact preliminary design of a SAR CubeSat is beyond the scope of this work.

Figure 4: CIRES spacecraft [36]

Lastly, the simplifying assumption that the antenna used was not a phased-array but a planar one was also taken to simplify the design process.
Some of the most prominent SAR missions in the Copernicus portfolio's performances are compared in tables 5, 3, 4 and 2 from which the base performance requirements for the instrument were derived.
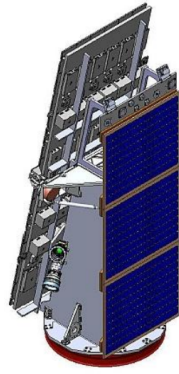
Figure 5: NOVASAR-S spacecraft [37]

Mode	Ground Resolution(m)	Elevation Angles^o	Swath Width(km)	N_{Looks}
ScanSAR	20 X 13.7	25-30	55	4
Maritime Surveillance	30 X 4	48-73	750	4
StripMap	6 X 13.7	16-31	15-20	1
ScanSAR Wide	30 X 13.7	15-29	150	3

Table 2: NOVASAR-S performance by mode [**NOVASAR**], [38]
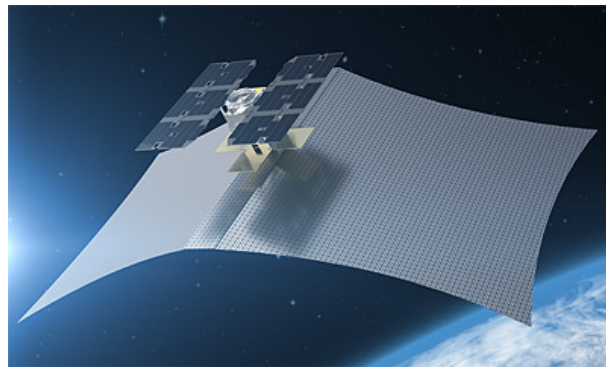
Figure 6: Capella Denali Spacecraft [39]

Mode	Ground Resolution(m)	Elevation Angles^o	Swath Width(km)	N_{Looks}
Spotlight	0.7-0.5 X 0.5	25-40	5	9
Sliding Spotlight	1.2-0.8 X 1	25-40°	5	5
StripMap	2.4-1.6 X 1.7	25-40°	5	1

Table 3: Capella X-SAR performance by mode [40]

Figure 7: ICEYE-X1 spacecraft [41]

Mode	Ground Resolution(m)	Elevation Angles(^{o})	Swath Width(km)	N_{Looks}
Spot	1 X 1	20-35	5	1-4
Spot Extended Area	1 X 1	20-35	15	1-4
Strip	3 X 3	15-30	30	1-2
Scan	15 X 15	21-29	100	1
Scan High	6 X 6	21-29	60	1
Spot Extended Dwell	1 X 1	20-35	5	1

Table 4: ICEYE performance by mode [42], [41]

Figure 8: Sentinel-1 spacecraft [43]

Mode	Ground Resolution(m)	Elevation Angles^o	Swath Width (km)	N_{Looks}
StripMap	5 X 5	20-45	80	1
EWS Mode	40 X 25 X 5	>20	400	1
IWS	20 X 5	>25	250	3
Wave Mode	20 X 5	23-36.5	20	1

Table 5: Sentinel performance by mode [44]

4.2   System Requirements

Parameter	NovaSAR-S	Sentinel-1	Capella X-SAR	ICEYE-X1
S/C mass (kg)	400	2300	40	85
Frequency (GHz)	3.1-3.3	5.405	9.4-9.9	9.65
Peak power (W)	1800	4800	600	3200
Polarisation	quad	quad	HH	VV
Antenna dimensions (m X m)	3 x 1	12.3 x 1.02	3.5 (circular, $\varnothing$)	3.2 X 0.4
Max bandwidth (MHz)	200	100	500	299
Duty Cycle (%)	2	12	10.4	4.6e-3
Orbit altitude (km)	580	693	485-525	560-580
Mean Power (W)	36	576	62.4	14.72

Table 6: SAR mission parameters compared [40], [45], [42].

As is clear from this table, the smaller the spacecraft the smaller the antenna size which must be compensated for with higher frequency carriers (higher bandwidth) to maintain a high resolution [46]. It is also clear that smaller spacecraft restrict flexibility in terms of peak power and sophistication, with only single polarisation modes available for imaging [47].

4.2.1   Form Factor

The spacecraft form factor was chosen to be a 16U CubeSat, similar to that of CIRES. It was assumed that anything smaller than this would be incapable of producing a similar antenna area to even ICEYE-X1, which was the smallest antenna area surveyed in table 6. Additionally, it was assumed that something smaller than this would be incapable of generating enough power to sustain a SAR payload consuming hundreds of watts. As with the ICEYE-X1 and ICEYE-X2 spacecraft, unfolding panels with areas equal to some multiple of those of the bus faces themselves could be employed.
This would give a 16U CubeSat the ability to match the antenna area of the ICEYE spacecraft, which is most near to it in terms of dimensions. This would also make it smaller in mass than the Capella Denali spacecraft, (next nearest to it in terms of size) as CubeSat standards dictate 1.3kg of mass per unit allowable [48]. Taking this standard and assuming the previously specified margin for propulsion systems and the deployable antenna, the wet mass for the spacecraft was calculated to be approximately 25 kg.

4.2.2   Power, Antenna Dimensions, Polarisation and Minimum SNR

A significantly lower peak power than ICEYE or Capella would likely be needed considering the form factor of the spacecraft and therefore its ability to generate and store power. This ability was assumed to be proportional to the physical dimensions of the bus, under the folding panels assumption mentioned above. Assuming that the back side of
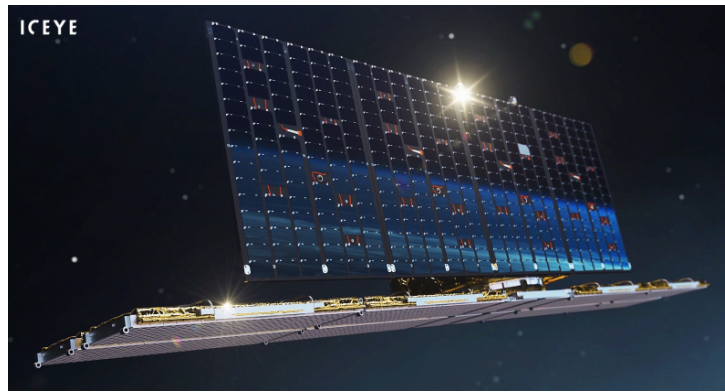
Figure 9: ICEYE-X2 spaceraft, with deployed folding solar arrays and SAR antenna [41]

any planar antenna could be used for power generation and considering current terrestrial commercial solar cell technology [49] an array of dimensions 2.2 x 0.5 m should be capable or producing approximately 300 W of power. Following standard practices [50] this panel would provide 180W orbit average power. Despite the exploration of orbits which could include a significant time spent in eclipse, these panels were assumed to provide a constant power output for simplicity. The dimensions of this array would also be compatible with the form factor selected above, considering a twice folding set of panels on either side of the spacecraft along its largest dimension.

Applying a significant margin to the required peak power for the lowest value of the surveyed missions (Capella) to compensate for the constrained form factor and more complicated thermal design problem resulting from said form factor, a peak power of 400W was estimated the system.

The smaller platforms surveyed had only a single polarisation in use (HH or VV). In this case as simplicity is preferred to accommodate possible issues with reduced size form factor and the fact that radar polarimetry is not required to detect vessels at sea, a single VV polarisation was chosen.

Generally speaking, 10dB is considered to be the minimum acceptable signal to noise ratio [51]. However, given the circumstances that maritime SAR image scenes are usually high contrast, a slightly lower value of SNR was deemed acceptable. This would in turn allow to compensate for some of the performance difficulties likely to be encountered due to the form factor chosen for the platform.

4.2.3   Orbit Height and Shape

Orbits for SAR systems tend to be circular in nature and ranging from 400-800 km to be close enough to Earth to mitigate the large power requirements and also to avoid the Van-Allen belts, as confirmed in table 6. The majority of the orbits of the platforms surveyed were approximately 500km in altitude, and as such this was chosen as the nominal spacecraft altitude.

Normally, Earth observation remote sensing platforms are placed in a Sun-synchronous orbit (SSO), such that the angle of the normal of their orbital plane with respect to the Sun is constant. This is done so as to ensure similar lighting conditions over imaged areas at each pass, giving the benefit of a near constant thermal noise in each image. This can be seen in the orbits of all of the surveyed satellites, orbiting in SSOs of approximately 97-98°.

However, the objective of this constellation is to survey ships at sea. The near total reflection of radio waves by the ocean and the near total reflection of metal ships will almost always yield a high contrast image. The angle of the ocean surface with respect to the incident waves results in almost all of them being scattered, leaving no return and an almost black area in the image (depending of course on ocean conditions). Consequently, the near perpendicular position of the metal superstructure of the vessels at sea yields a strong radar return and so generally a high SNR for an image of just sea and ships. As such, the effect of thermal noise is less significant than it tends to be in land base imaging applications. Thus, the benefits of an SSO from this standpoint are nullified.

Figure 10: ICEYE SAR acquisition of a ship [52]

There is then the case that an SSO allows the impacts of J2 on certain orbital elements to be frozen. However, assuming that the spacecraft (like ICEYE) has a propulsion system, the relatively inexpensive cost of the platform (being a CubeSat) and its replacement may not warrant the additional manoeuvring cost of placing it in a higher inclination orbit. In any case the longest pass possible through the target area was sought to maximise area coverage and minimise revisit time. This restricts constellation combinations to Walker Delta and Star shapes and inclinations to less than 90 degrees.

4.2.4 Strip Size and Imaging Duty Cycle

The maximum strip length was determined by considering the length of the approximate largest dimension of the target area. Drawing a line diagonally from South-East to North-West (35ºN, 32ºE to 38ºN, 0ºE as seem in figure 1) across the target area gave an approximate maximum path length through the zone of 2866 km. This corresponds to an angular distance of 0.44985 radians assuming a spherical Earth and an average planetary radius of 6371 km.

Considering the 500 km circular orbit already chosen and an equivalent average Earth radius of 6371 km, the angular velocity of the spacecraft could be found as shown in equation 9.

$$\omega = \frac{\sqrt{\frac{\mu_{Earth}}{h+R_{Earth}}}}{h+R_{Earth}} = 1.1085 x 10^{-3} rad/s$$

(9)

Assuming that the Earth is spherical as a simplifying assumption, this would take the sub-satellite point of the spacecraft approximately 405 seconds to transit the longest path across the target area. This defines the maximum operating time of the instrument, and thus the duty cyle. With an orbital period of 5668.14 seconds, the maximum imaging duty cycle becomes 7.16% of the orbital period. The radar duty cycle was set at a maximum of 15% in transmit and 5% in receive, considering the Sentinel-1 and Capella values with the relevant margins applied. This would result in a maximum average power of approximately 60 W. similar to that of Capella.

4.2.5   Propulsion System

In order to maintain precise distances from the other spacecraft within an orbital formation, while also combating the effects of orbital perturbations the spacecraft required a propulsion system. While ICEYE uses an ion thruster and chemical propulsion systems are generally reserved for larger spacecraft, a chemical thruster was chosen for this design. An ion thruster would use more power than a cold gas thruster, which would mean a lower rate of continuous operation of the payload which was deemed to have priority. Given the recent advances in cold gas thruster miniaturisation this, several COTS options exists. For the purposes of this design something similar to the VACCO CPOD was chosen [53]. The unit is capable of providing approximately 25 m/s of delta-v to a spacecraft of 25kg[54].

4.2.6   Noise Figure and Losses

The system noise figure and losses are difficult to quantify a-priori. Advances in technology would likely produce a lower noise figure overall for a system of similar specifications today, however it was assumed that the process of miniaturising such a system would incur penalties resulting in slightly worse performance than even the original Sentinel system. As such, the values of Sentinel-1 [55] were taken with the applied relevant margins to account for this, resulting in a Noise Figure of 3.5 dB being used.
Additionally, similar X-band link budgets [56], [57] account for system losses for the instrument were set at 2 dB. A number of loss sources still needed to be accounted for however. These included imperfect antenna radiation pattern, possible pointing errors and sea clutter. At X-band frequencies, sea clutter mainly due to high winds can account for a change in the backscatter coefficient of up to 6 dB in high winds [58]. This is especially the case for high grazing angles and VV polarisation. An additional set of losses of 2 dB were considered for the radiation pattern losses, in addition to other unforeseen possible sources of loss. (referred to as L_{misc}) each way were considered in the system losses term. This was such that the total 2-way system losses could be considered as shown in equation 10.

$$L = L_{ins} + L_{clutter} + 2 * L_{misc} \tag{10}$$

4.2.7   Multi-Launch Capacity

For the sake of the constellation sizing, the number of satellites that can be delivered to orbit with each launch must be considered as this defines the number of launchers

required to complete the constellation and so heavily influences its cost. Given the low delta-v available from the chosen thruster, for the purposes of orbital insertion and phasing the spacecraft were assumed to be inserted by the upper stage of the launch vehicle or via a dedicated upper stage insertion vehicle such as the Momentus Space "Ardoride" [59]. At this moment in time, the only proven launcher with an upper stage capable of putting several satellites on separate orbits during the same launch is the Falcon 9 from Space X [60].
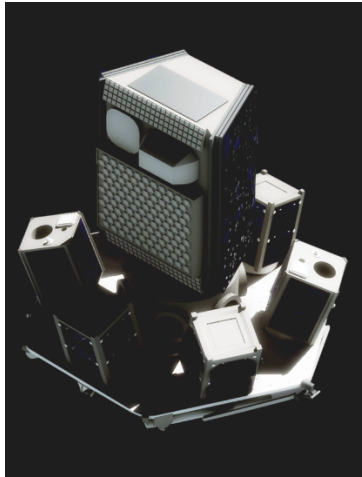
Figure 11: Momentus Ardoride last-mile delivery spacecraft [59]

Given the CubeSat form factor of the spacecraft, it is likely that whatever number of them being launched, they would fly as a secondary or ride-share payload. This would mean that only a fraction of the mass limit would be available for use for constellation spacecraft. In the case of the Falcon 9 standard payload of approximately 1800kg, it was assumed that less than half of the payload capacity would be available for ride-sharing purposes. This put the maximum launch mass per batch at 900 kg. In the case of the 16U bus selected, this equated to 36 satellites which could be launched at the same time.

4.2.8   Elevation Angle Range and Nominal Pointing

In the case of the single-train formation, an elevation range of 15-45° was chosen for the hypothetical instrument. This look angle range was assumed to apply to the individual formations, such that the minimum elevation of the instrument looking closest to the nadir vector in a 150km swath formation would be that of the minimum value in the range and vice-versa.

The instrument was assumed to be pointed at 0-Doppler and at a nominal passive look angle of 30° on a fixed side of the spacecraft to simplify its operation in addition to the design process. Considering the inclination restrictions imposed by the Walker patterns to be explored in this work, a port-side instrument pointing was chosen.

The port-side pointing was chosen to minimise the inclination difference required from the minimum launch inclination. Assuming the worst case scenario, where the launch inclination is that of the minimum possible from the proposed launch site. As shown in figures 12 and 13 respectively, this would allow the minimum amount of inclination change possible to reach an orbit which could still access the highest latitude point in the target area.
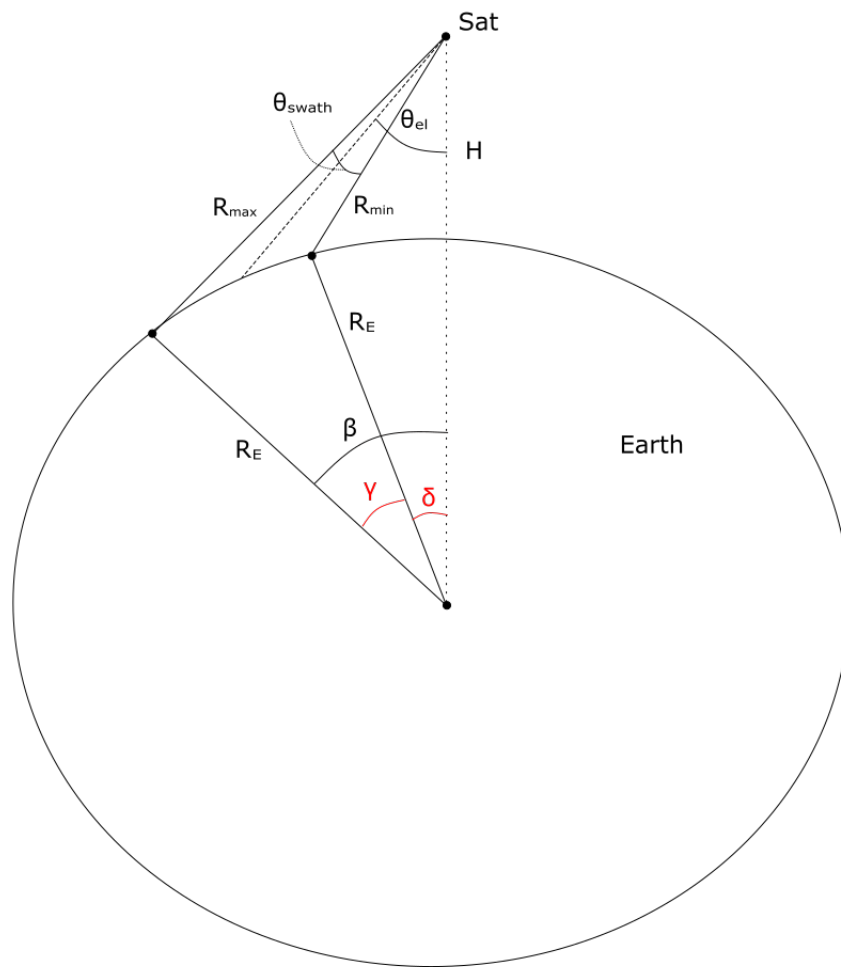
Figure 12: Coverage angles for off-nadir pointing instrument

With these angles calculated, the latitude and longitude ranges for the swath on an inclined orbit could be calculated considering the geometry depicted in figure 13 and applying quaternion rotations. This subsequently allowed for the computation of the minimum allowable inclination for the constellation. This minimum allowable inclination could then be used to constrain the genetic algorithm and reduce the size of the search space.
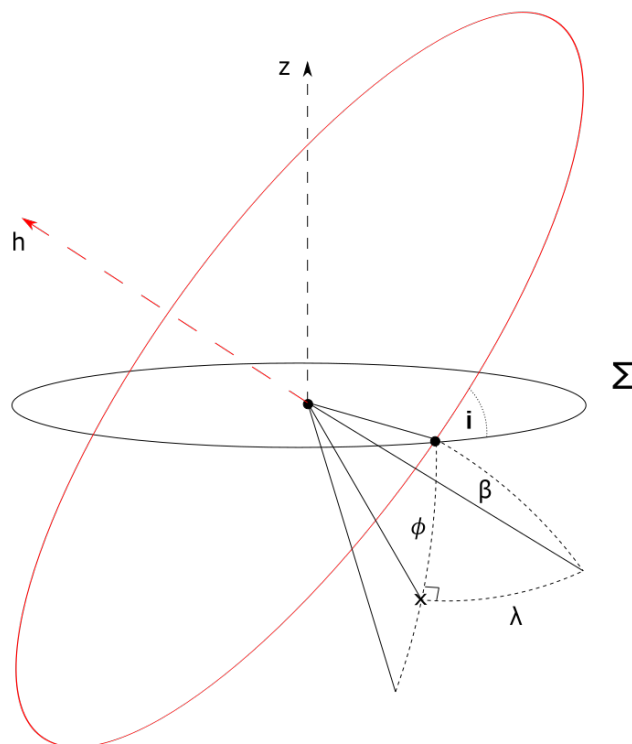
Figure 13: Latitude/longitude reach of spacecraft swath on an inclined orbit, considering a starboard-side pointing

4.2.9   Minimum Orbit Inclination

In order to ensure access to every point in the target area, the highest point in the target area must fall within the beamwidth of the antenna at least at the highest spacecraft latitude as it transits its orbit. For a port-side pointing, this means that the latitude of the far side beam edge must be at least that of the most northerly point in the target area. As such, from the latitude of the most northerly point in the target area and a fixed instrument pointing and swath size, applying the geometry of figure 12 and 13 the minimum inclination could be calculated as per equation 11.

$$i_{min} = \phi_{max} - \beta \tag{11}$$

This logic is shown clearly in figure 14 below, where ϕ_{max} represents the latitude of the most northerly point in the target area.

As seen in figure 13, the required rotation matrix was that calculated as seen in equation 12. In this case $\Delta\Omega$ was the difference in original orbit right ascension due to orbit perturbations.
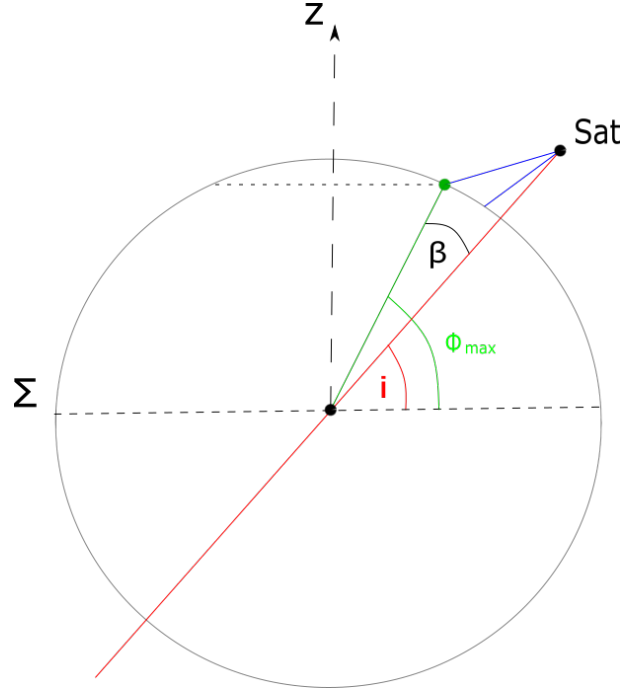
Figure 14: Minimum inclination definition incorporating geometry from figures 12 and 13

$$R_{\theta i \Delta \Omega} = \begin{bmatrix} cos(\theta + \omega) & -sin(\theta + \omega) & 0 \\ sin(\theta + \omega) & cos(\theta + \omega) & 0 \\ 0 & 0 & 1 \end{bmatrix} \begin{bmatrix} 1 & 0 & 0 \\ 0 & cos(i) & -sin(i) \\ 0 & sin(i) & cos(i) \end{bmatrix} \begin{bmatrix} cos(\Delta \Omega) & -sin(\Delta \Omega) & 0 \\ sin(\Delta \Omega) & cos(\Delta \Omega) & 0 \\ 0 & 0 & 1 \end{bmatrix}$$

$$(12)$$

The result was converted into quaternions and applied to the swath maximum and minimum vectors to create the ground track of the instrument swath in latitude and longitude.

4.2.10   Resolution and Swath Width

Considering the unknown capabilities of a CubeSat SAR instrument, for the purposes of this design the lower end of this resolution was chosen as the base on ground resolution requirement. This was decided to be the same in both ground image directions such that the on-ground resolution was 5 x 5 m.

Taking a middle value from the surveyed systems above, the swath width for a single formation was chosen to be 30km. Following the same logic a swath width of 150km was chosen for the CMWS mode envisaged. This would be achieved by 5 formations designed to image a 30km swath flying in formation with each other while imaging at separate elevation angles, as per section 3.3.

Considering the antenna dimensions chosen, the elevation beamwidth could be checked to ensure compatibility with the chosen swath dimensions at closest pointing so as to avoid a slewing requirement during imaging. The elevation beamwidth was calculated as in equation 13.

$$\theta_z = \frac{\lambda}{L_z} = 3.5325^o \tag{13}$$

Using the geometry from section 4.2.8 the required beamwidth angle to cover the 30km swath, $\theta_{swath@15^o}$ was found to be only 0.2439^o, and thus well within the antenna beamwidth.

4.2.11 Carrier Frequency and Bandwidth

Considering the resolution and antenna sizing limitations above (in addition to the frequencies used by the two closest spacecraft in dimension to the 16U bus) the carrier frequency was chosen to be in the X-band frequency range. This band spans from 8-12 GHz as per ITU-R V.431-8 designations [61] with a specific portion reserved for microwave remote sensing of 9.3-9.9 GHz [62]. A range of 9.45-9.75 GHz was chosen in this case to capture the lower intermediate range of the range of frequencies surveyed while staying within band designations. This achieves a middle value of the surveyed values while also compensating for the likely lower energy output capabilities of the platform.

The higher frequency allows for the usage of a large bandwidth, however given the general rule that bandwidth if proportional to signal power for wireless transmissions [63], a maximum bandwidth of 100 MHz was imposed to account for the foreseen lower power electronics required by the smaller bus system. This of course could be reduced for a coarser resolution if desired.

4.3 Individual Satellite Performance Summary

Considering all of the above design assumptions, the individual satellite performance and system performance are summarised in table 7 below.

Parameter	Value
Wet mass (kg)	25
Size (U)	16
Multi-launch capacity	36
Orbit altitude (km)	500
Look angle interval (deg)	15-45
Instrument pointing direction	Port-side (fixed)
$\Delta V available (m/s)$	25
Instrument scan modes	Stripmap
Instrument peak power (W)	400
Instrument TX duty cycle (% /orbit)	≤ 15
Instrument RX duty cycle (% /orbit)	<5
Instrument carrier frequency (GHz)	9.45-9.75
Maximum CHIRP bandwidth (MHz)	100
Antenna length (m)	2.2
Antenna height (m)	0.5
Polarization	VV
Swath size	30/150km
Ground Resolution	5x5m
Overall losses in TX/RX (dB)	12
RX noise figure (dB)	3.5
SNR required (dB)	8-9

Table 7: Summary of spacecraft and instrument performances

5   Formation Design

The minimum MIMO CubeSat formation required to achieve the performance set out in section 4.3 was investigated assuming that each spacecraft performed as in table 7. This investigation served as a working point for the constellation design but also as a validation that the chosen parameters were compatible with each other beyond the initial preliminary investigations performed.

As discussed, a number of CubeSats with the above specifications were assumed to be flown in a single train formation capable of imaging a swath of 30km in size at the specified resolutions. For the purposes of the high-resolution wide-swath mode of operation, 5 adjacent trains would be required to provide a total swath width of 150km.

5.1   Formation Sizing

For the sake of the formation sizing a single target was assumed to be at the far edge of the beamwidth. Considering the formation as a monolithic system such that the antenna length and transmit power could be considered as a linear combination of the individual transmitters in the formation and setting the minimum SNR required for a positive identification (PID), the transmitted power required by the individual satellite transmitters could be calculated as seen in equation 6 in section 2.3. As per Giudici et. al [**Giudici. D.**], trains with a number of satellites less than 3 would be infeasible for a MIMO formation due to the significant probability of destructive interference so a minimum formation size of 3 was considered feasible. Additionally, as per Giudici the SNR gain due to MIMO operation is specified as being between 60-92% of the maxiumum possible gain of N^2. For this design a midpoint was taken of 77%. The antenna length was also assumed to stack as per section 2.3.

5.1.1   Worst Case Sizing

To assess the feasibility of the system for the task, the worst-case target acquisition scenario was examined. This scenario was identified as that of the smallest RCS vessel (40 m^2) at the largest look angle (45°) and the highest centre frequency (9.75 GHz). Considering this case, the peak power required per satellite was plotted against the formation size to determine the ideal number of satellites in the formation. Of note is the horizontal line indicating the maximum peak power of the individual instruments. In doing so, the duty cycle was adjusted to ensure correct reception (no pulse overlap) as seen in figure 18. The maximum PRI was selected so as to reject azimuth ambiguities for this case. Finally, an antenna efficiency of 82.5 % was estimated as a midpoint of the range of values discovered in literature [64], [65], [66]. Finally, the local inclination of the surface impacted by the incident pulses was assumed to be 0. For clarity, the reference geometry is represented in figure 15. Considering this geometry it was assumed that the angle α was equal to the negative of the central angle for the side of the swath being considered as per figure 12. For the farside of the beam width for example, the angle alpha was taken to be $-(\gamma + \delta)$ and so on.
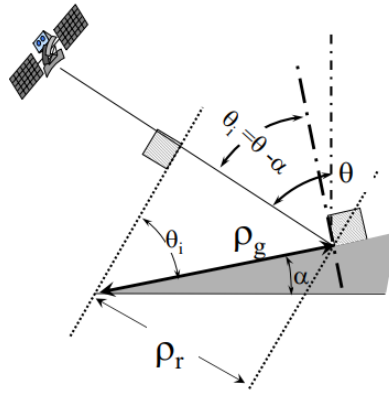
Figure 15: Radar geometry considered [11]

5.1.2   Formation Design Results
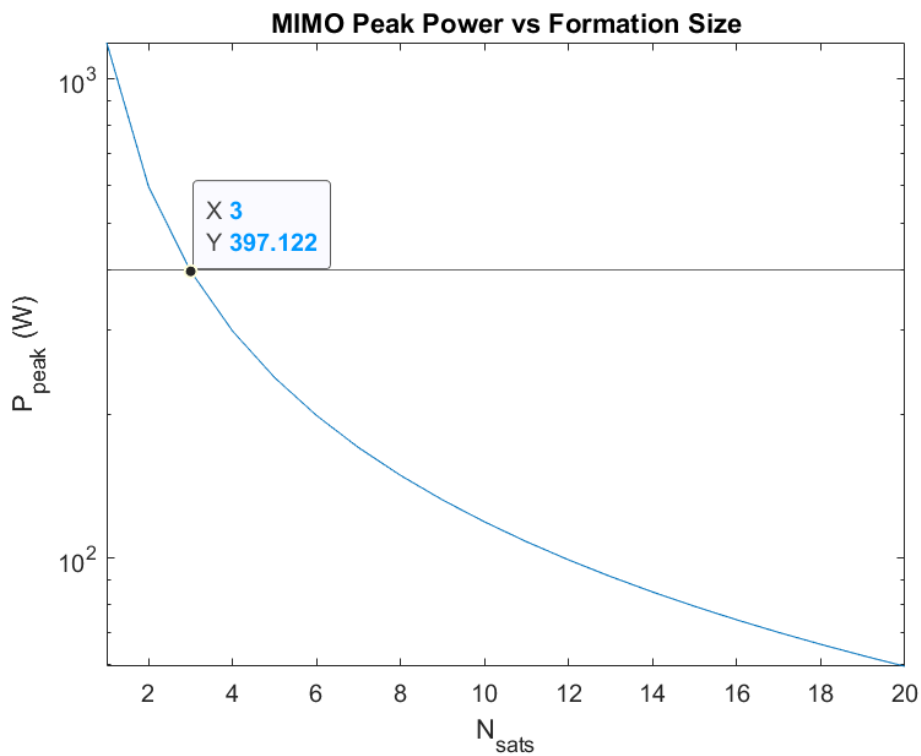
Figure 16: Plot of peak power vs formation
size for 30 km swath

As seen in figure 16, the optimal formation size for the required performance considering these conditions was found to be 3 satellites for a 30 km ground swath. The peak power required per satellite for a 3-satellite formation solution was approximately at the 400 W limit at 397.122 W with an average power of 42.8892 W. Similarly, a duty cycle of 10.8 % was found to be optimal for the 30 km swath to ensure correct reception.
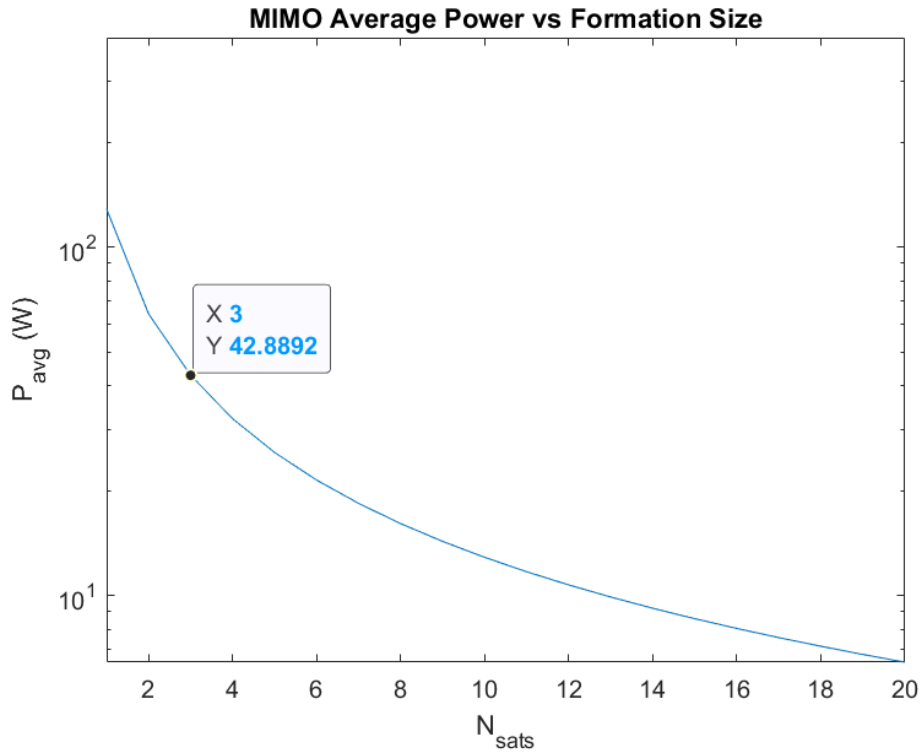
Figure 17: Plot of average power vs formation
size for 30 km swath
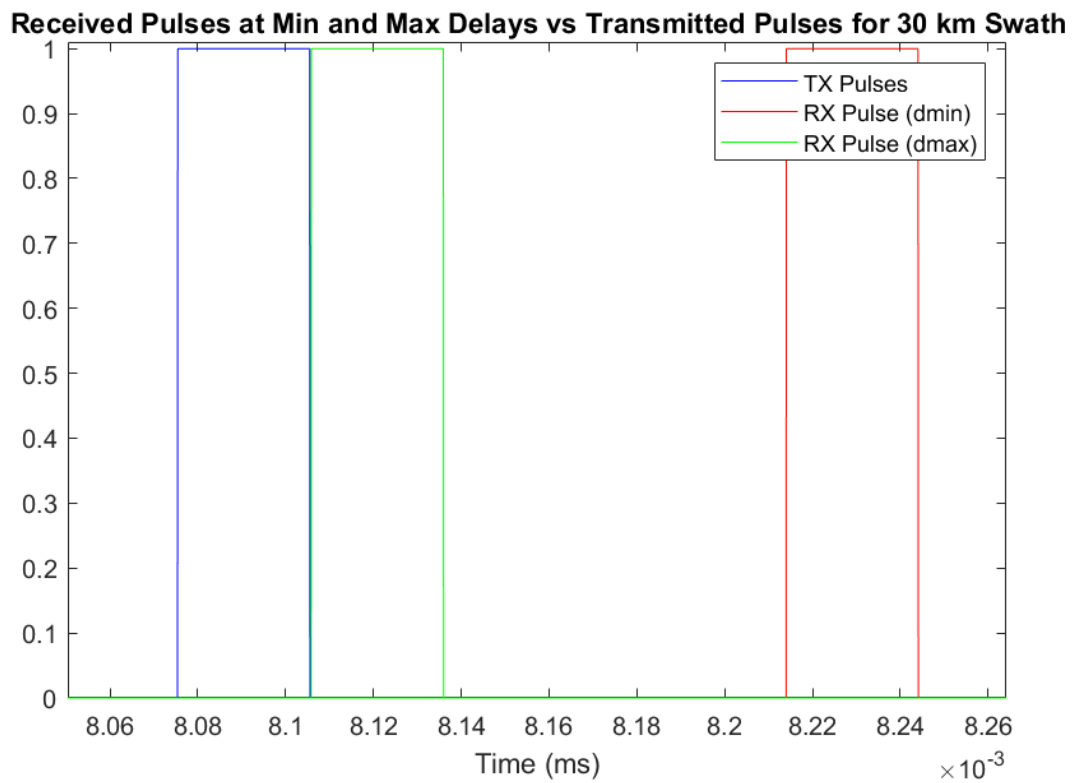
Figure 18: Plot of transmitted and received pulses for 30km swath and 10.8% duty cycle

Each spacecraft in the formation was assumed to be separated by a distance of less than 300m as per similar studies [67], requiring careful control using a nonlinear controller such as that developed by Montero-Miñán [68]. This distance (which amounts to the along track sampling interval) must be controlled with a strict accuracy shown in equation 14 in order to provide the necessary ambiguity suppression[2].

$$\sigma_{at} << \frac{\delta_x}{N} = 1.1m \tag{14}$$

Similarly, the across-track accuracy must be kept with an accuracy of that shown in equation 15. For the purposes of this calculation a scene height dispersion in the order of the size of one resolution cell was considered.

$$\sigma_{xt} << \frac{R\lambda sin\theta}{2\pi\sigma_q} = 345.496m \tag{15}$$

The design and implementation of such a control system to maintain these accuracies was considered to be beyond the scope of this work. As a result, inter-satellite distances were assumed to be guaranteed within the aforementioned specified limits for the sake of this project.

The required bandwidth to achieve the set ground resolution was calculated at the antenna beam's nearside, farside and boresight. As shown in figure 19, at the minimum elevation angle for the instrument the maximum allocated bandwidth is exceeded for all but the farside of the imaged swath. In this case, the maximum bandwidth would have to be increased to 120 MHz to maintain the desired ground resolution. Alternatively, a lower resolution could be accepted at the nearer side of the image for this elevation angle.
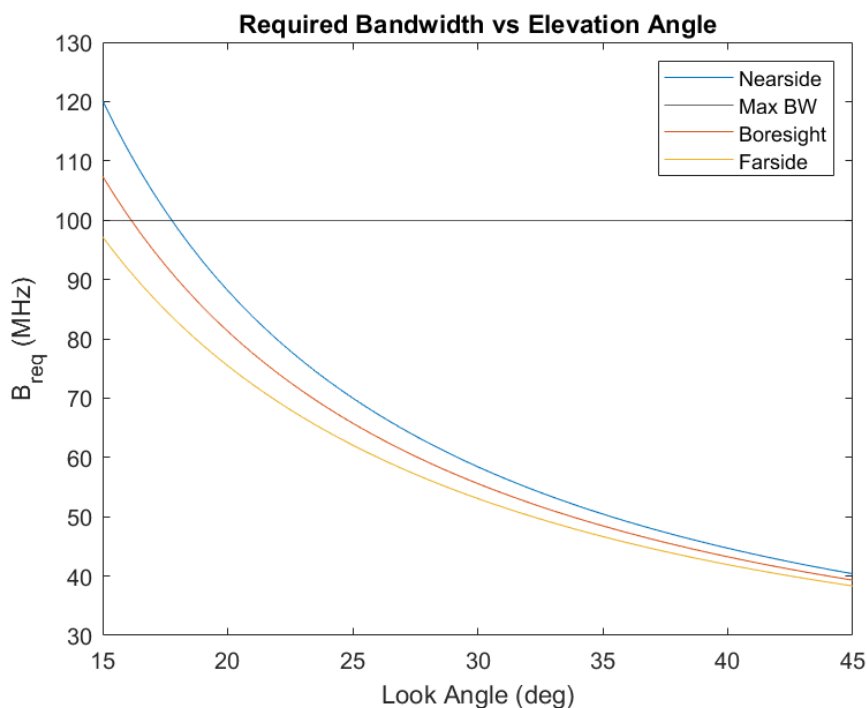
Figure 19: Required bandwidth for set resolution at the nearside, boresight and farside of the imaged swath for each of the elevation angles considered

The parameters for the formation worst-case sizing are summarised in table 8.

Parameter	Value
Formation Antenna Length (m)	6.6
Formation Antenna Height (m)	0.5
Instrument Elevation (deg)	45
Wavelength (m)	0.03084
Elevation Beamwidth (rad)	0.03074
Slant Range Resolution (m)	3.53
Required Bandwidth (MHz)	42.397056
Antenna Spacing (m)	3.3
Azimuth Resolution (m)	3.3
Azimuth Beamwidth (rad)	0.002329
Noise Factor	2.238
Noise Temperature (K)	649.2291
Noise Power (W)	2.04167 X 10^{-20}
Satellite Velocity (km/s)	7.616556
Boresight Ground Range (km)	500
Squint Angle (rad)	0.3
PRI (s)	0.000433267
Synthetic Aperture Length (km)	3.34403347
Synthetic Aperture Time (s)	0.43904
Synthetic Aperture Bandwidth (Hz)	2.2776
Number of Pulses	1013.3434
PRF (Hz)	2308.04745
Beam Sector (rad^2)	0.000286
Single Antenna Gain	11257.99626
Antenna Efficiency(%)	77
Antenna Effective Area (m^2)	1.541
Instrument Duty Cycle (%)	10.8
Pulse Length (s)	4.67928 X 10^{-5}
Noise PSD (dB)	-200.475
Noise Bandwidth (dB)	3.574881
Total Noise Power (dB)	-193.4
Peak Power (W)	397.122
1-Way Path Loss (dB)	-128.112
Total Losses (dB)	-193.816
Mean Received Power (dB)	-189.816
SISO SNR (dB)	-0.41587
MIMO Gain (dB)	8.407
MIMO SNR (dB)	7.9914

Table 8: Radar properties used

6   Constellation Design

6.1   Design Cases

For the purposes of this design, a number of scenarios were considered. Performance-based design using a multi-objective genetic algorithm for an unlimited number of launches was investigated so as to identify the minimum number of launches required for a set of prescribed performance requirements. This was examined both for the single-train and CMWS configurations so that the benefits of the latter with respect to the former could be analysed. This analysis was done for scan mode, after which the search mode was investigated.

6.2   Walker Constellations

Walker constellations are widely used as a preliminary design tool for constellation design [8], [6]. Generally speaking, Walker patterns like the Star and Delta are used for global coverage designs [69]. When considering a regional design problem such as this one, usually street-of-coverage patterns are used [70] [71]. However, the application of this type of pattern to regional designs in literature has largely been for smaller areas [72] [73]. Additionally, designs have appeared in literature for regional coverage of larger regions like the US [74], Iran [75] and Indonesia [5] utilising Walker constellation patterns despite their original global coverage intention.

Moreover, given the large number of variables which could conceivably be controlled by this algorithm a simplifying assumption was required to reduce the search space and make efficient use of the limited computational power that was available. Walker Star and Delta constellation patterns are the simplest to work with and some of the most well-known patterns for constellation design. Considering this and the large target area of interest, these patterns were chosen to be explored. It was anticipated that this may result in constellations using an excessive number of satellites and planes for regional performance, and too few satellites or planes for significant global performance. However the benefits in terms of accessibility in design and simplicity were decided to outweigh applicability issues for this case.

Walker pattern constellations consist of T Satellites distributed evenly among P orbital planes, all inclined by inclination i and with a relative phasing F. As a result, designs are described by T/P/F nomenclature for efficient reference [76].

Each plane is evenly separated in nodal right-ascension by an inter-plane phasing constant and each satellite in an orbital plane is separated from each other by an intra-plane phasing constant. The above can be summarised by figure 20 where a generic Walker constellation is visualised. Each spacecraft in a Walker constellation experiences similar perturbations to its orbit and thus they have similar operational lifetimes. This is one of the primary advantages of the Walker constellation design approach, while also simplifying the design problem significantly. There are multiple permutations of Walker constellation, however as discussed for the purposes of this work only the 2 main ones were investigated; the Walker Star and the Walker Delta. Walker Delta constellations have inclinations usually between 30° and 60° but in any case less than 90°. A Walker Star constellation is a polar constellation, with all orbits having a shared 90° inclination.
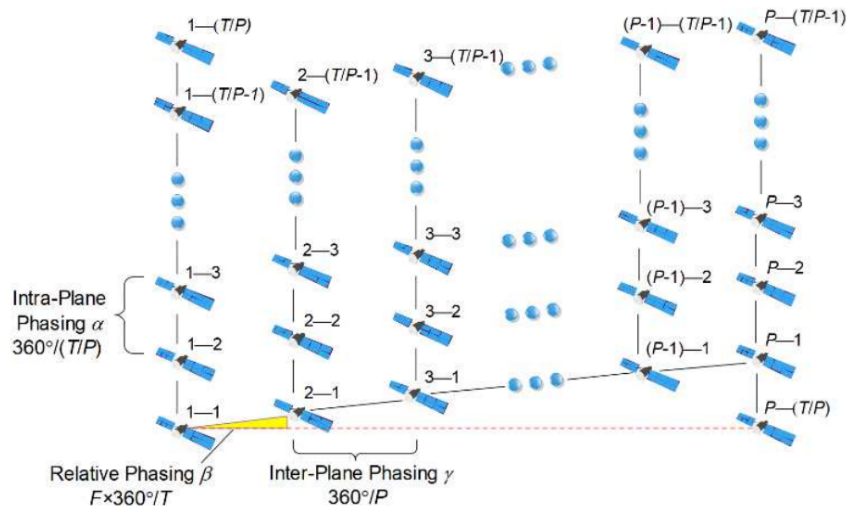
Figure 20: Generic Walker constellation and associated parameters [77]

As is clear from figure 20, the phasing constant must not have the same value as the number of satellites in the total constellation, otherwise there would be no relative phasing and a collision could occur. Additionally, the modulo of the number of satellites in the constellation and the number of planes must be 0, such that the total number of satellites is evenly divisible by the total number of planes with T,P and F all being integers.

6.3   Simulation Algorithm

The algorithm used to simulate each constellation functioned as follows:

- The simulation is initialised with launch date of 1st January 2024 at 00:00:00 UTC. A universal time vector spanning from the launch time to the launch time plus the desired simulation time in Julian datetime is then created.

- Each formation in the constellation was assigned an orbit with orbital elements based on the initial simulation parameters.

- Following this, each of the formations was inserted into the constellation in line with the Walker constellation design format.

- The pattern units and spacings were calculated and applied to each formation in each orbital plane.

- Instrument beam geometries and longitude/latitude coverage were calculated as per the logic and geometry presented in section 4.2.8, as shown in figures 21 and 22 respectively.

  From this, the maximum and minimum reach of the instrument swath in terms of latitude and longitude are ascertained.

```
16      curvature = 1/R_E;
17
18      RBS = quadSolve(1, -2*(h+R_E)*cos(look_angle), (h+R_E)^2 - R_E^2);
19      gamma = asin(RBS*sin(look_angle)/R_E);
20
21      Rmax = sqrt(R_E^2 + (h+R_E)^2 - 2*R_E*(h+R_E)*cos(gamma+(1/R_E)*(swath_size/2)));
22      el1 = abs(asin(sin(gamma+(15/R_E))*R_E/Rmax) - look_angle);
23
24      Rmin = sqrt(R_E^2 + (h+R_E)^2 - 2*R_E*(h+R_E)*cos(gamma-(1/R_E)*(swath_size/2)));
25      el2 = abs(look_angle - asin(sin(gamma-(15/R_E))*R_E/Rmin));
26
27
28
29      squint_angle = el1 + el2;
30
31      beam_max = look_angle + el2;
32
33      beam_min = look_angle - el1;
34
35      NS_central = gamma-(swath_size/2)*curvature;
36      FS_central = gamma+(swath_size/2)*curvature;
37      ymin = NS_central*R_E;
38      ymax = FS_central*R_E;
39
40      coverage = R_E*(FS_central - NS_central);
```

Figure 21: Beam geometry code snippet

```
89              R_theta = [cos(real(theta + w)) sin(real(theta+w))   0
90                         -sin(real(theta+w)) cos(real(theta+w))    0
91                                       0              0            1];
92
93          R_inc = [1          0          0
94                   0  cos(inc) -sin(inc)
95                   0  sin(inc)  cos(inc)];
96
97          R_raan = [cos(draan)  -sin(draan) 0
98                    sin(draan) cos(draan) 0
99                    0          0          1];
100
101         quat1 = quaternion(R_theta, 'rotmat', 'frame');
102         quat2 = quaternion(R_inc, 'rotmat', 'frame');
103         quat3 = quaternion(R_raan, 'rotmat', 'frame');
104
105         Rmax_int1 = quatrotate(compact(quat1), Rmax_orb);
106         Rmax_int2 = quatrotate(compact(quat2), Rmax_int1);
107
108         Rmax_ECI = quatrotate(compact(quat3), Rmax_int2);
109
110         Rmin_int1 = quatrotate(compact(quat1), Rmin_orb);
111         Rmin_int2 = quatrotate(compact(quat2), Rmin_int1);
112
113         Rmin_ECI = quatrotate(compact(quat3), Rmin_int2);
```

Figure 22: Coverage calculation code snippet

- Each orbit in the constellation was propagated under applied perturbations using ode113 as the numerical solver and as part of a constellation object with each of its positions and velocities stored.

```
8    options = odeset( 'RelTol', 1e-13, 'AbsTol', 1e-14);
9
10   [~,Y] = ode113(@(t, x) kep_ode_pert(t, x, mu, J2, cd, Am, planet_radius, w_Earth,m), times, x0, options);
11
12
13   x_pos = Y(:,1);
14   y_pos = Y(:,2);
15   z_pos = Y(:,3);
16
17   x_vel = Y(:,4);
18   y_vel = Y(:,5);
19   z_vel = Y(:,6);
20
21   pos_matrix = [x_pos y_pos z_pos];
22   vel_matrix = [x_vel y_vel z_vel];
```

Figure 23: Orbit propagation code snippet

- The target area of interest was set up, along with the target grid if constellation performance was being analysed.

```
9    [vertSpacing, horzSpacing] = SetGridRes(resKeyWord);
10
11   topHull = max(AO_Y);
12   botHull = min(AO_Y);
13
14   rightHull = max (AO_X);
15   leftHull = min(AO_X);
16
17   horzVector = botHull:horzSpacing:topHull;
18   vertVector = leftHull:vertSpacing:rightHull;
19
20   |
21   [X,Y] = meshgrid(horzVector', vertVector');
22
23   points = [X(:) Y(:)];
24
25   targets = zeros(length(points),2);
26
27   for ii=1:length(points)
28       if inpolygon(points(ii,2), points(ii,1), AO_X, AO_Y) == 1
29           targets(ii,:) = points(ii,:);
30       else
31           continue
32       end
33   end
34   NonZeroRows = find(~all(targets==0,2));
35
36   targets = targets(NonZeroRows,:);
```

Figure 24: Grid setup code snippet

- Following this, for each moment in time the ground track of the instrument swath is checked to see if it falls within the target area set up above. This is done by creating a linearly spaced vector between the maximum and minimum latitude and longitude points of the swath with 100 spaces. Following this, inPolygon is called for each point. If the result is true, the time of its occurrence is stored. This is done for every orbit in the constellation.

- A loop is run over each of the recorded times (each pass through the target area) with a Polygon created from the max and min points of the instrument swath at each time step. Subsequently, inPolygon is applied to check if the grid points are inside of the instrument swath at any point between time steps. If yes, these values are recorded. In the case of the grid, the times are assigned to each grid point. This is repeated for every orbit in the constellation.
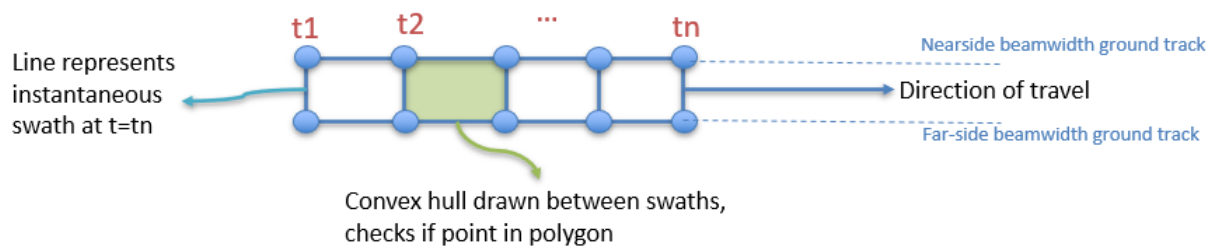
Figure 25: Grid point search algorithm visualised

```
21    for ll=1:length(tgt_X)
22        [PointInSwath,~] = inpolygon(tgt_X(ll), tgt_Y(ll), swath_X, swath_Y);
23        try
24        if PointInSwath==1 && flags(ll)==0 % check if point is in swath and has
25                                            % not been found in this same swath.
26                                            % If it has, skip. If not, record
27                                            % PID time and set a flag that it's
28                                            % been found.
29            % increment PID so that if the same point is found next time it
30            % does not overwrite the previous stored time
31            PID(ll) = PID(ll) + 1;
32
33            % store the time of the positive ID in a column of t_PID
34            % and a row which corresponds to the number of the point. (point 1
35            % in row 1)
36            t_PID(ll,PID(ll)) = t_AO(kk);
37
38            flags(ll) = 1;
39        else
40            continue
41        end
42        catch
43            disp('error: pausing');
44        end
45    end
```

Figure 26: Grid point search code snippet

- At this point the constellation performance is calculated by measuring the number of grid point identifications, maximum revisit time per point, leakage time per point across the total area etc.

- Following this, any plots required are created. In the case of the tracking algorithm the grid is replaced with a moving target but the same logic is applied.

6.3.1   Orbit Propagation and Orbital Elements

Orbit propagation for every case examined in the MOGA was conducted using a time step of 60 seconds. The propagator chosen for this task was ode113 as accuracy was deemed most important for this evaluation as covered in section 6.7. All formations in the constellation were assumed to have the same argument of perigee, semi-major axis and eccentricity to begin with.

The orbit propagator was validated using orbital elements from Sentinel-1B. The elements were taken from publicly available TLEs [78] at an interval of 24 hours. Ingesting these TLEs, the spacecraft orbit was propagated for 1 single orbital period. Using a live tracking source [79], 3 equally observations equally spaced in time were recorded of the satellite Cartesian position. Using the Gibbs method for preliminary orbit determination, the instantaneous orbital elements for the spacecraft were recovered. Analysing the difference in the orbital elements obtained by Gibbs method and those produced by the propagator, using the Sentinel-1B system requirements document as a guideline [80] the propagator was validated for use as a preliminary design tool.

6.3.2   Perturbations

Drag and J2 perturbations were considered for the purposes of this analysis. Acceleration due to J2 effect was calculated as in equation 16 obtained from Curtis [81].

$$\boldsymbol{\alpha_{J2}} = \frac{3}{2}\frac{J_2\mu R_e^2}{r^4}\left[\frac{x}{r}(5\frac{z^2}{r^2}-1)\widehat{\boldsymbol{i}} + \frac{y}{r}(5\frac{z^2}{r^2}-1)\widehat{\boldsymbol{j}} + \frac{z}{r}(5\frac{z^2}{r^2}-3)\widehat{\boldsymbol{k}}\right] \qquad (16)$$

The standard J2 constant of 1.018e-3 was applied, additionally for all computations in this work an average Earth radius of 6371 km was assumed.

Acceleration due to drag was calculated as per equation 17. The satellite mass from section 4.3 was used along with a drag coefficient of 2.2 as is standard for this type of investigation [82]. Each satellite was assumed to have a cross sectional area equal to that of the major dimensions of its SAR antenna, which was assumed to be perpendicular to the relative velocity of the satellite with the atmosphere. This simulates a worst case scenario which provides a lower bound for the satellite lifetime for the purposes of this early investigation. The relative velocity in this case is the difference between the satellite's velocity vector and the velocity vector of the atmosphere. The latter is calculated as the cross product between the earth's angular velocity and the satellite orbital radius.

$$\boldsymbol{\alpha_D} = -\frac{1}{2}\rho v_{rel}\frac{C_D A}{m_{sat}}\boldsymbol{v_{rel}} \qquad (17)$$

The atmospheric model used in this analysis was that of the 'US Standard Atmosphere 1976' (USSA76) model found in Curtis [81].

6.3.3   Formation and Number of Satellites

For the sake of this simulation, each formation was considered as a single monolithic satellite delivering the specified performance outlined in section 5. As such, the total number of formations was used as the instead of the total number of satellites. As a result, for each constellation combination the total number of satellites required equals the number of formations times 3 for the single-train case and times 15 for the CMWS case.

6.4   Performance Metrics and Analysis

Before selecting metrics for performance analysis, a spaced grid was generated inside of the target area to discretise it as seen in figure 27. A selection of performance metrics could then be analysed on a per-point basis over a given time vector for the set grid, to give a better indication of the target area-wide constellation performance. The grid spacing used for this preliminary level of design was set as 444 km in the longitude direction and 222km in the latitude direction respectively.
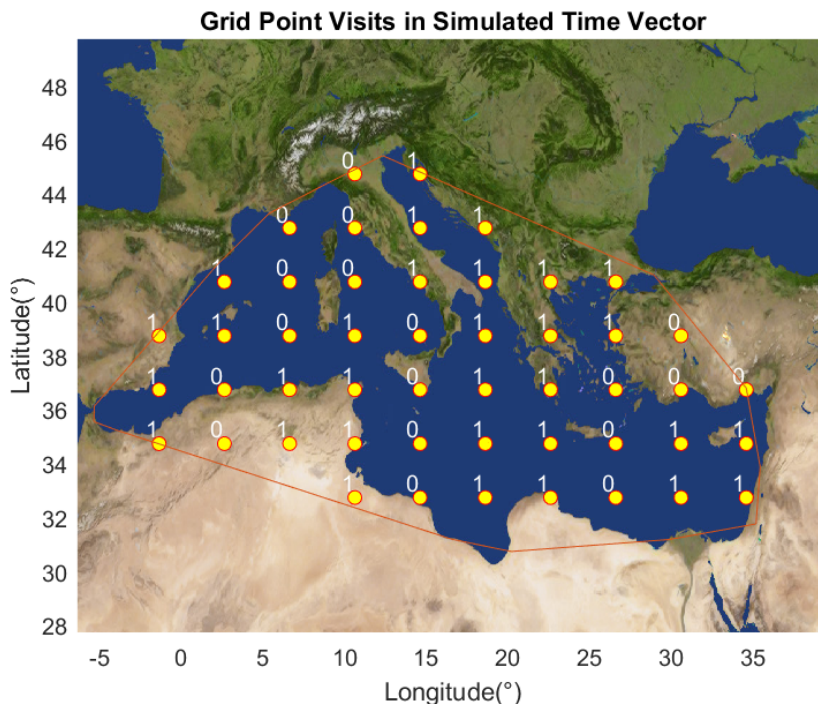
Figure 27: Sample evaluation grid showing number of point visits for a single-train formation over 15 orbits

The performance metrics were decided to be as follows:

1. Average Leakage time (s)

2. Area Coverage (%)

3. Leak Time Deviation (s)

4. Number of formations used (total number of satellites)

5. Number of orbital planes

6. Difference in inclination from the launch site (rad)

The average leakage time of each point is the most obvious basic metric given the a set desired revisit performance for the constellation and was defined as the amount of time between point visits by a spacecraft in the constellation. The reasoning behind this request is that the point revisit rate will most-significantly impact the tracking performance for the constellation. This being the intended product of the constellation itself means this metric has the highest priority for performance analysis. An average value of the point leakage time for the target area was used to determine if a constellation meets the minimum requested design requirements. Total percentage of the target area covered was deemed as a high priority for the tracking solution to ensure as much of the target area was covered as possible in the set time frame.

In order to assess uniformity and completeness of the coverage of the target area respectively, both the standard deviation of the average point leakage time across the area and the area coverage must be considered. Both of these considerations serve to ensure the best possible tracking performance inside of a given period of time and must be minimised and maximised respectively.

The number of satellites used for the solution directly effects its setup, operation and maintenance costs. As such, the fewer formations (and thus satellites) used the better.

Finally, the difference in inclination from the proposed launch site and number of planes was considered to account for the costs (both financially and in terms of delta-V) of inserting the constellation into the required orbits. At the time of completion of this work, the only launcher capable of placing several satellites on different orbits via upper stage manoeuvring is the Falcon 9. The launch site was thus set as Cape Canaveral, Florida as this is primarily where the company launches the vehicle from. It is possible that another launch vehicle using a last-mile delivery vehicle could achieve the same result, but without knowing the number of planes to be reached a-priori it is not possible to know if the upper stage vehicle along could reach all of them. To give the best possibility of deploying all required satellites on their respective planes without needing a second launch or manoeuvring by the spacecraft themselves, choosing the Falcon 9 was seen as the safest option.

Given that the primary payload being launched is unlikely to be this constellation and that the destination of the primary is unknown, the launch inclination was set to the minimum achievable from the launch location; the latitude of the launch site. The constellation will require higher inclination orbits to reach the highest latitude of the coverage area (approximately 45 degrees). This is far closer to the maximum achievable inclination of 55° using this launcher than the minimum of 28.5^o [60]. Setting the value to the lower bound of the inclinations achievable from the launch site therefore accounts for the maximum foreseeable inclination change required and thus constitutes the upper bound of the manoeuvring costs for launching from this site. It is of course possible that the upper stage could insert the primary payload on an orbit with a different inclination, but without knowledge of the launch manifest the above assumption was deemed satisfactory for this phase of the study.

6.5   Minimum Constellation Performance

To be viable as a solution for maritime surveillance within the selected target area, the solution should achieve a set of minimum performances.

6.5.1   Average Leakage Time

To set the revisit rate or leakage time performance, current industry service offerings were reviewed. Most services cite their search mode performance when quoting revisit times as it tends to be significantly lower than the scan mode performance. In the case of Capella, with 6 satellites a mean revisit time of 3-6 hours is claimed and a maximum of 6 hours [83]. With 18 satellites, 1-3 hours revisit time is claimed.
Examining the offerings of ICEYE, an equatorial mean revisit time of 20 hours is quoted with 14 satellites in their constellation [41], [84]. This is quoted alongside a mean time-to-access of 12 hours. NovaSAR-S lists revisit times of 14-34 hours with 3 satellites [38] while Sentinel-1 is obviously the lowest at 24-72 hours due to being only a double satellite constellation [43].
Considering all of the above services, the minimum average revisit time was chosen to be 6 hours with no limit on the maximum revisit rate. Given that the time for the constellation to acquire any one point in the grid for the first time does not constitute a revisit, leakage time was used to refer to the time elapsed between point identifications. This time was what was used to measure the constellation performance.

6.5.2   Area Coverage

To effectively search for or track ships in the target area, the majority of the area should be covered within a 24 hour period. Coaster-type vessels are not particularly fast, with design speeds in the 14-15 knot range and average speeds significantly less [85]. As such, their positional uncertainty per unit leakage time is rather low. This positional uncertainty was calculated assuming that the vessel maintained a constant speed from its last acquisition and could head in a straight line in any one direction. This creates a circular area of radius $v_{vessel} * t$ at each time step in which the vessel could be located anywhere. This positional uncertainty was assumed to be fixed such that instrument swaths passing through it without identifying the true location of the vessel would not decrease the positional uncertainty. This assumption was taken to simplify the simulation process.
For a coaster travelling at maximum speed, the approximate positional uncertainty in a 24 hour period was therefore +/- 600 km in any one direction. However, given the 6 hour average revisit time imposed by similar products, this puts an average positional uncertainty requirement of +/- 166km. This in turn gives a circular search area around the last known location of the vessel of 86569 km^2, just 3.53% of the 2.45 million square kilometer search area considered.
Given this ratio, a 100% area coverage rate in such a short period of time was not deemed as required, but obviously the closer to 100% coverage the better. This would be because a lost vessel of this class could not get very far compared to the major dimension of the search area itself in the set simulation time. If the vessel was located even once the search area could be narrowed to that area of a few hundred km, and if it was not located in the search period it must exist in the much smaller, un-searched area. Regardless, this creates a viable search and track approach without applying stringent performance restrictions.

To guarantee that most of the area was covered a target area coverage limit of 85% was imposed. This could be increased or decreased as the service itself is defined in more detail.

6.5.3 Maximum Number of Launches

The final Capella constellation consisting of 36 individual satellites was deemed as a reasonable analogue for the number of launches required to fully deploy the constellation. In the case of the MIMO Cubesat formations this value would obviously need to be multiplied by 3 as the performance of a single satellite in the Capella constellation is matched only by 3 CubeSats in close formation. This would require 3 launches at maximum capacity to deploy fully. In the meantime, as constellations are trending towards mega-constellations like Starlink, the benefit of additional satellites not only in terms of redundancy but also on performance was decided to be worthy of investigation. As such the maximum number of launches available was decided to be 5. This imposes an upper limit of 60 formation flights in the single-train configuration and 12 formation flights in the CMWS configuration, totalling 180 satellites at maximum.

6.5.4 Minimum Constellation Performance Summary

The minimum constellation performances are summarised as:

- Average leakage time (revisit rate) < 6 hours

- Area coverage > 85 %

- Maximum number of launches for deployment = 5

6.6 Working Point

Prior to running the optimisation procedure, a working constellation for both the single-train and high-resolution wide-swath cases was manually found via iteration such that the minimum required performances were met. The variables for each solution are reported in table 9 with performance listed in table 10 and visualised in figures 28, 29, 30 and 31 respectively. A time step of 5 seconds and a grid spacing of of 55.5km in longitude and 27.5km in latitude was used for this analysis.

6.6.1 Working Point Constellations

Case	Orbit Planes	Inclination (rads)	Formations	Phasing Constant	$\Omega_0(rads)$
Single-train 30km swath scan mode	55	0.7662	55	1	4.9334
CMWS 150km swath scan mode	11	0.7662	11	1	4.9334

Table 9: Working point constellation variables

6.6.2   Performance Over Target Area
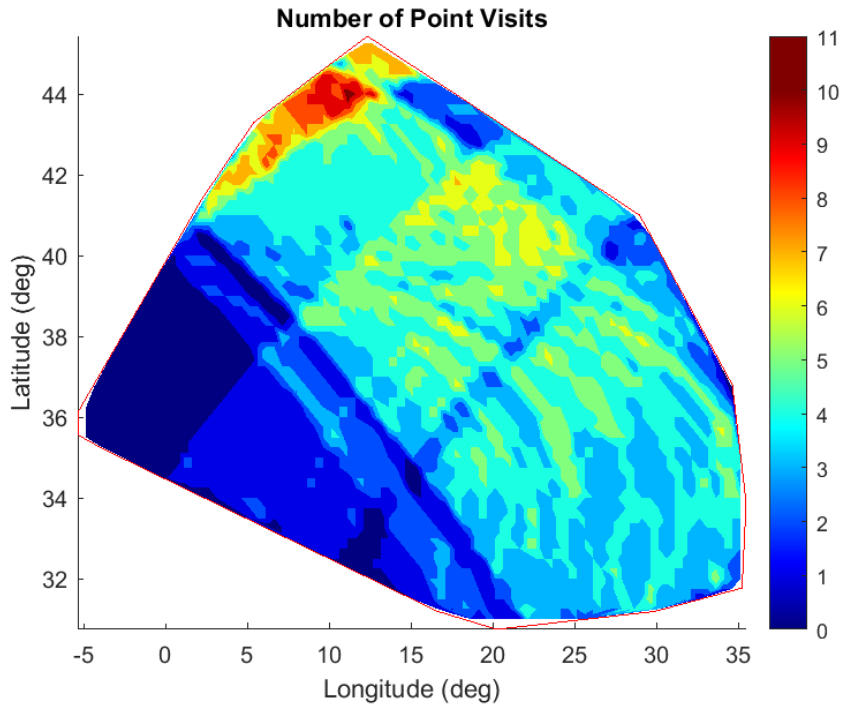
Figure 28: Single-train scan mode number of visits per grid point in 24 hours
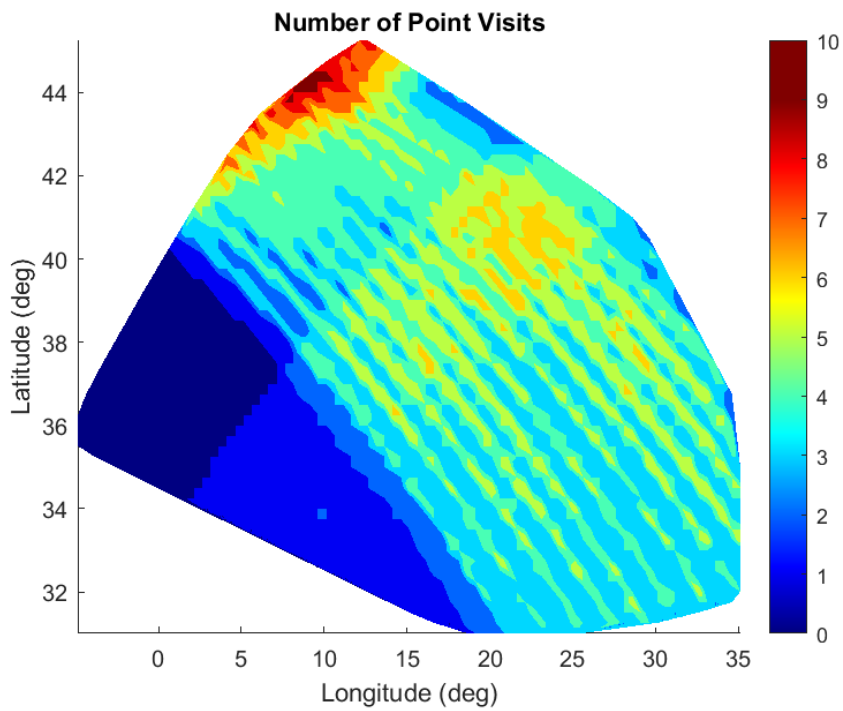
Figure 29: CMWS scan mode number of visits per grid point in 24 hours
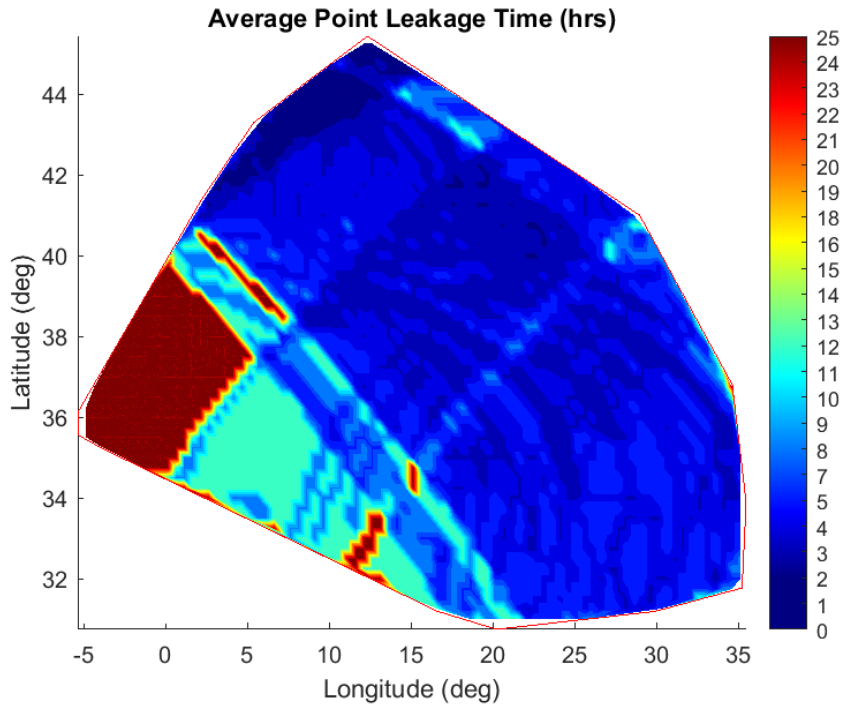
Figure 30: Single-train scan mode average leakage time per grid point in 24 hours
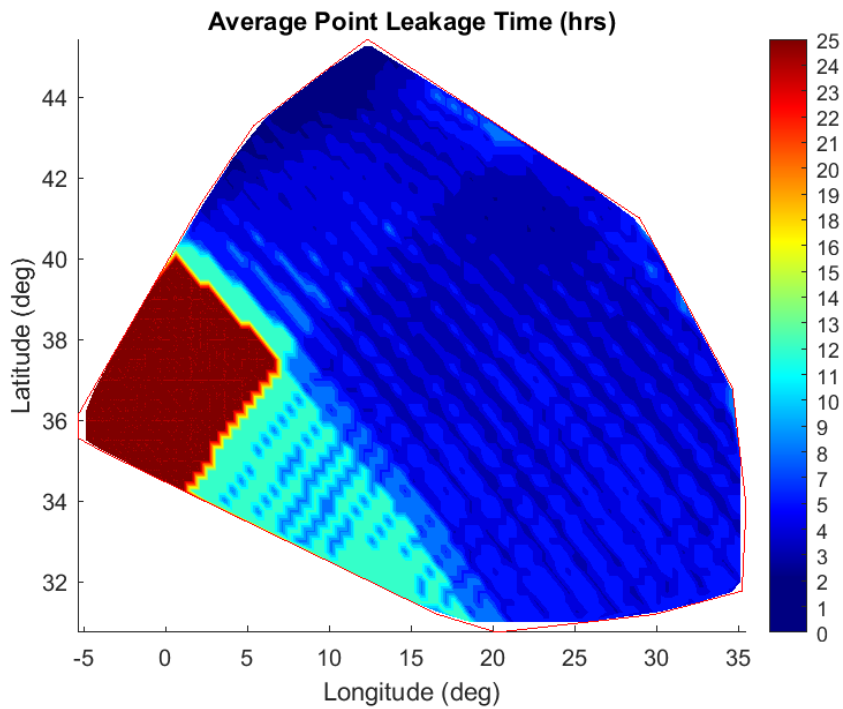
Figure 31: CMWS scan mode average leakage time per grid point in 24 hours

Case	Mean t_{leak} (hrs)	Deviation t_{leak} (hrs)	$A_{covered}$ (%)
Single-train scan mode	5.63	7.85	90.938
CMWS scan mode	5.614	7.82	89.704

Table 10: Working point constellation performances

36

6.7   The Multiple Objective Genetic Algorithm

To design the optimal constellation and attempt to improve upon the working point, a multi-objective genetic algorithm (MOGA) was used. The problem to be solved consists of a very large search space with a high degree of non-linearity. To avoid getting stuck in local minima or maxima, a large population was foreseen to be required. As per Vrajitoru [86], larger populations are preferred over a large number of generations. This would result in exceedingly long compute times due to the accuracy that the solution provides, so parallel computing was leveraged to reduce compute times. Regardless, for the fixed hardware available for simulations there therefore existed a set amount of compute power to be used in a time efficient manor to optimise the problem.

While analytical and semi-analytical methods such as those of [10], [87] would produce a faster convergence of the algorithm, the results achieved would be less accurate. While this is usually an acceptable trade-off for this phase of the design process, there exists less work done in literature on constellation designs with this level of accuracy for this specific objective. As such, the choice of accuracy over speed was deemed to be of more interest.

6.7.1   Pareto Optimality

The goal of the MOGA is to find the set of variables which achieve Pareto optimality for a set of fitness functions. Pareto optimality is reached when a set is optimised such that improving one of the outputs worsens the at least one of the others [88]. For a 2 objective optimisation this can be visualised by means of a Pareto front [89].

6.7.2   Variables

The MOGA was given control over the following variables:

- Number of orbital planes (P)

- Orbit inclination (i)

- Total number of formations (T)

- Phasing Constant (F)

- First orbit nodal right ascension (Ω_0)

6.7.3   Constraints

To avoid non-eligible solutions and subsequently accelerate the rate of convergence of the algorithm, the MOGA must be constrained. The constraints for this optimisation problem take three forms; linear and nonlinear equality constraints, integer constraints and upper and lower bindings.

Considering sections 6.2, 4.2.9 and 6.4 the design problem could be simplified as follows:

$$
\begin{cases}
\min(\text{P,T,(i-}i_0), t_{leak}, \, std(t_{leak}), \, \frac{1}{A_{cov}}) \\
P & \in [1, \text{ T}] \\
i & \in [\text{i}_{min}, 90^o] \\
F & \in [1, \text{ T-1}] \\
T & \in [1, \text{ 60}] \\
\Omega_0 & \in [1, \text{ 360}^o] \\
mod(T, P) & 0
\end{cases}
\tag{18}
$$

Given the above problem, this optimisation was defined as a nonlinear mixed-integer problem with a large search space even after considering the constraints applied to the algorithm. As such, a large computational time (in the order of hours) was expected.

6.7.4   Simulation Time Period

Given the preliminary nature of the design, performance was analysed over a 24 hour period for the target area. Each orbit combination was therefore propagated for 16 orbits from the set start date of January 1st 2024 at 0000 Zulu time. This was deemed to be sufficiently close to the ground track repeat rate of 15.24 orbits to assess the constellation performance with the appropriate level of accuracy for this level of investigation. The repeat rate under J2 was calculated as in equation 19.

$$
\frac{k}{m} = \frac{n + \dot{\omega} + \dot{M_0}}{w_E - \dot{\Omega}}
\tag{19}
$$

The MOGA optimisation was run with a time step of 60 seconds. Once favourable combinations were found, performance was analysed in more detail using a finer time step of 5 seconds over a 24 hour period. Additionally, a finer grid spacing was used to give a more detailed image of the data recorded per grid point and the coverage area.

6.7.5   MOGA Algorithm Summary

For each individual in the population, the algorithm outlined in 6.3 was run as part of the fitness function placed into gamultiobj in MATLAB. The chosen performance parameters were then input as fitness functions for the MOGA. The process is summarised in figure 32 diagram.
For the sake of this investigation a population of 200 with 100 generations and a propagation time step of 60 seconds was used for all MOGA analyses. Results generation took several hours, in some cases as long as 45 using sequential solving. This improved to 20 hours using parallel computing tools. All simulations were run on an i3-7100U processor clocked at 2.40 GHz with 4 GB of RAM.
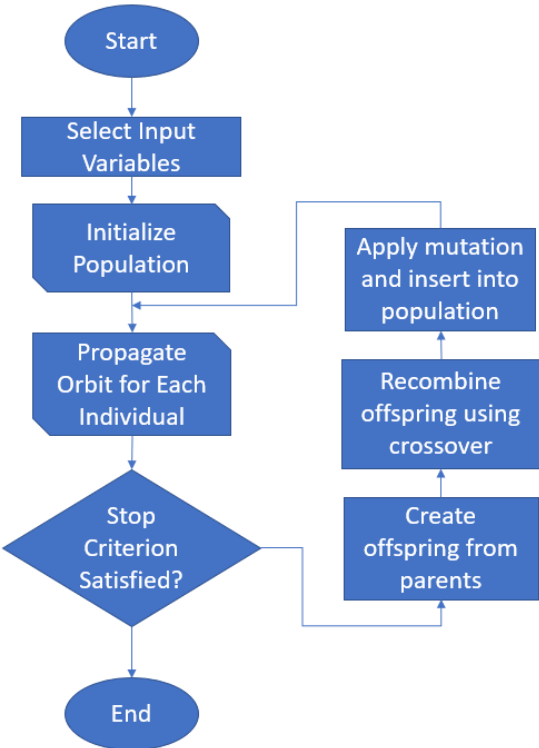
Figure 32: MOGA runtime diagram

7   Results

7.1   Single-Train Scan Mode

7.1.1   Best Designs

The best 20 constellation designs achieved from the MOGA for scan mode are shown in table 11, along with their performance based on the fitness functions used. The combinations in table 11 are the best 20 Pareto plot points from the final generation of the genetic algorithm sorted in terms of leakage time. The most important relationships between all 6 objectives are shown via the aforementioned Pareto point plots shown in figures 33, 34, 35 and 36 respectively. All other Pareto plots are visible in appendix 10
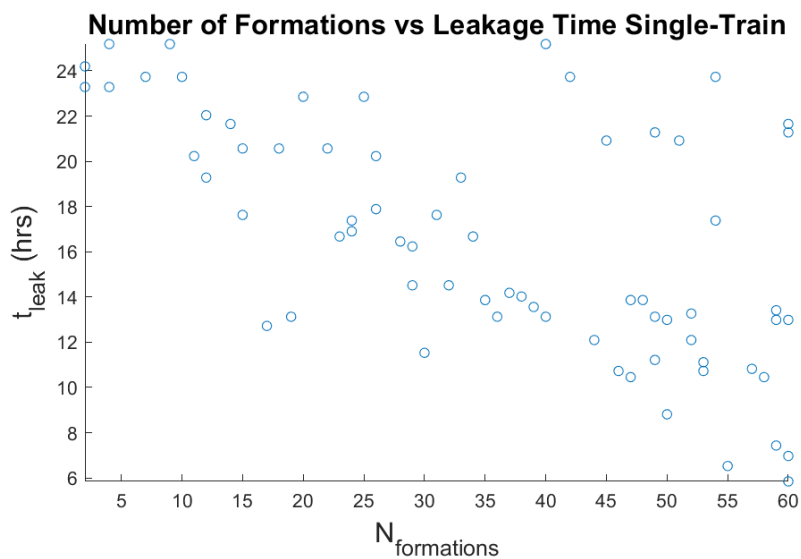
Figure 33: Plot of number of formations vs leakage time for single-train configuration 30km swath scan mode
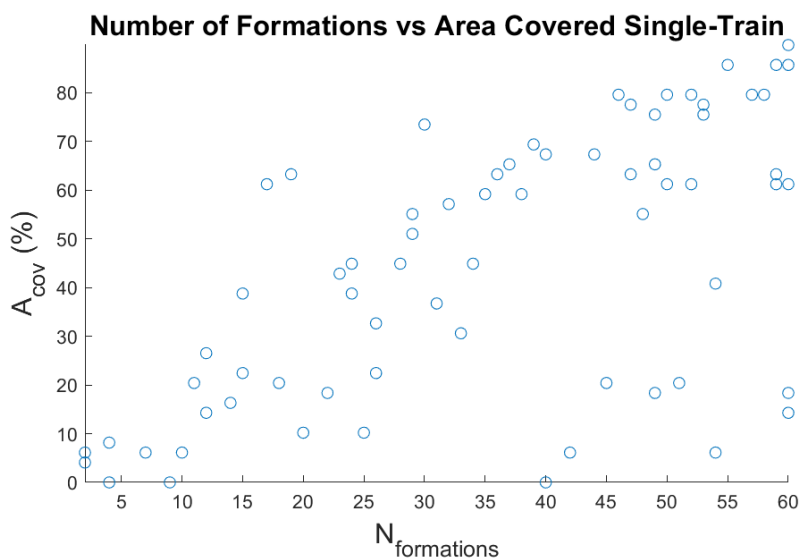
Figure 34: Plot of number of formations vs area covered for single-train configuration 30km swath scan mode

40
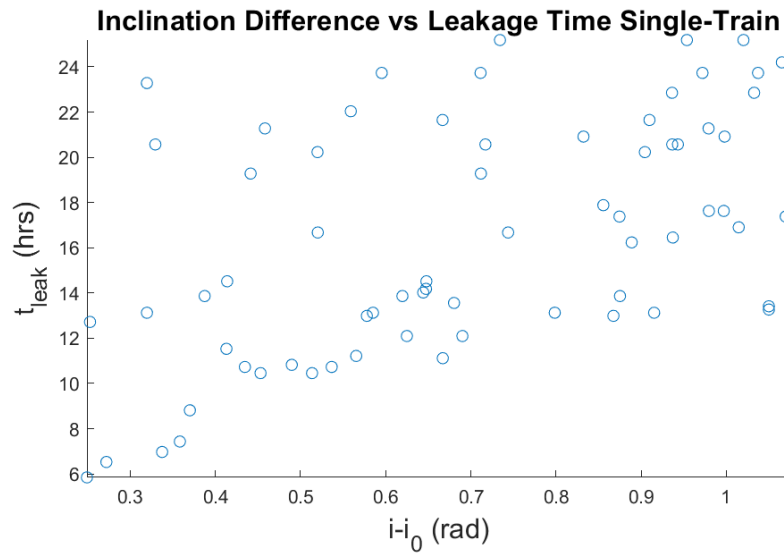
Figure 35: Plot of inclination difference vs leakage time for single-train configuration 30km swath scan mode
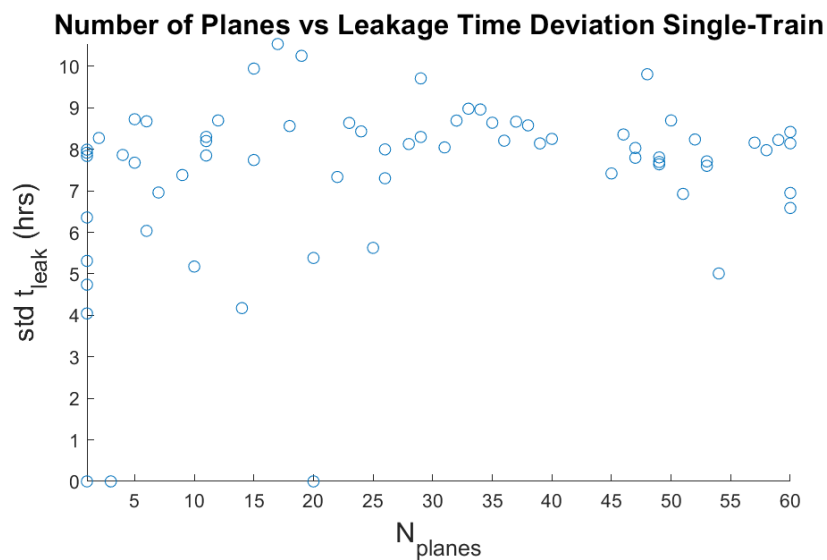
Figure 36: Plot of number of planes vs leakage time deviation for single-train configuration 30km swath scan mode

Planes	i (rad)	Formations	Phasing Constant	$\Omega_0(rads)$	Mean t_{leak} (hrs)	Std t_{leak} (hrs)	$A_{cov}(\%)$
60	0.74467	60	1	6.2832	5.8483	8.4191	85.7118
11	0.76749	55	26	0.19251	6.529	8.3004	85.7118
60	0.83296	60	23	6.2435	6.9717	8.1453	89.7988
59	0.8538	59	52	4.9102	7.4336	8.2263	85.7118
50	0.86552	50	11	3.1329	8.8142	8.6971	79.5924
47	0.94852	47	28	2.4207	10.457	8.033	77.5494
58	1.0091	58	53	1.8594	10.457	7.98	79.5924
46	0.93017	46	21	6.0276	10.73	8.3589	79.5924
53	1.0321	53	27	4.3785	10.73	7.7109	77.5494
57	0.98525	57	16	2.7639	10.824	8.1611	79.5924
53	1.1626	53	40	4.2482	11.117	7.6029	75.5115
49	1.0609	49	47	6.0377	11.218	7.6962	75.5115
15	0.90846	30	14	1.2783	11.533	9.9458	73.4699
11	1.1856	44	35	4.1574	12.098	7.8519	67.3491
52	1.1204	52	49	5.4739	12.098	8.2376	79.5924
17	0.74825	17	15	0.030397	12.721	10.538	61.2257
1	1.363	59	1	3.7956	12.989	7.9921	61.2257
1	1.5708	60	1	6.2831	12.989	7.92	61.2257
5	1.0734	50	43	3.8189	12.989	8.7258	61.2257
36	1.2941	36	19	0.90544	13.127	8.2084	63.2671

Table 11: Single-train configuration scan mode MOGA results

7.1.2   Best Individual: Performance Over Target Area

Given the lack of an imposed maximum allowable leakage time, the best individual was chosen based on mean leakage time and area coverage. Only one individual was capable of reaching the minimum prescribed performances outlined in section 6.5.4 as seen in table 11. Performance of this constellation across the target area for the simulated time period is presented in figures 38 and 39 respectively. For the sake of this detailed performance analysis, a higher density grid (spacing 55.5 km in longitude and 27.75 km in latitude respectively) and a smaller time step of 5 seconds were used. These grid and time step parameters were used for all of the detailed analyses performed in this investigation.

Single-Train MOGA Best Individual
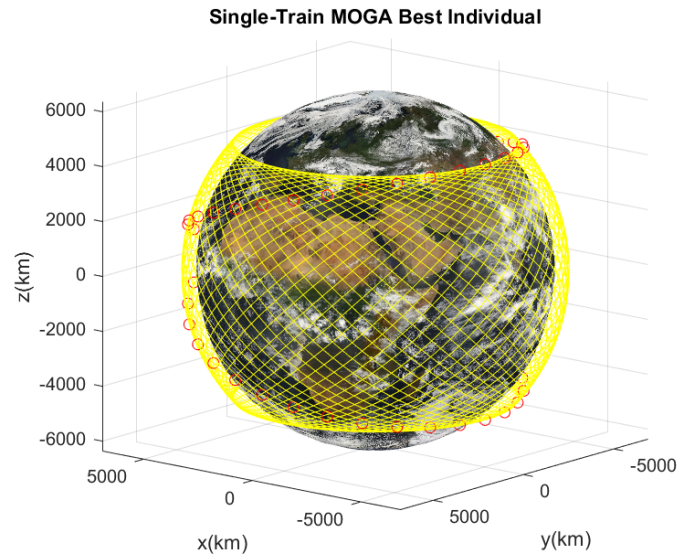
Figure 37: MOGA best individual 30km scan mode constellation orbit plot

Mean t_{leak} (hrs)	Std t_{leak} (hrs)	$A_{cov}(\%)$	Satellites
4.8733	7.633	91.119	180

Table 12: Detailed performance numbers for best single-train scan mode individual

Average Point Leakage Time (hrs)
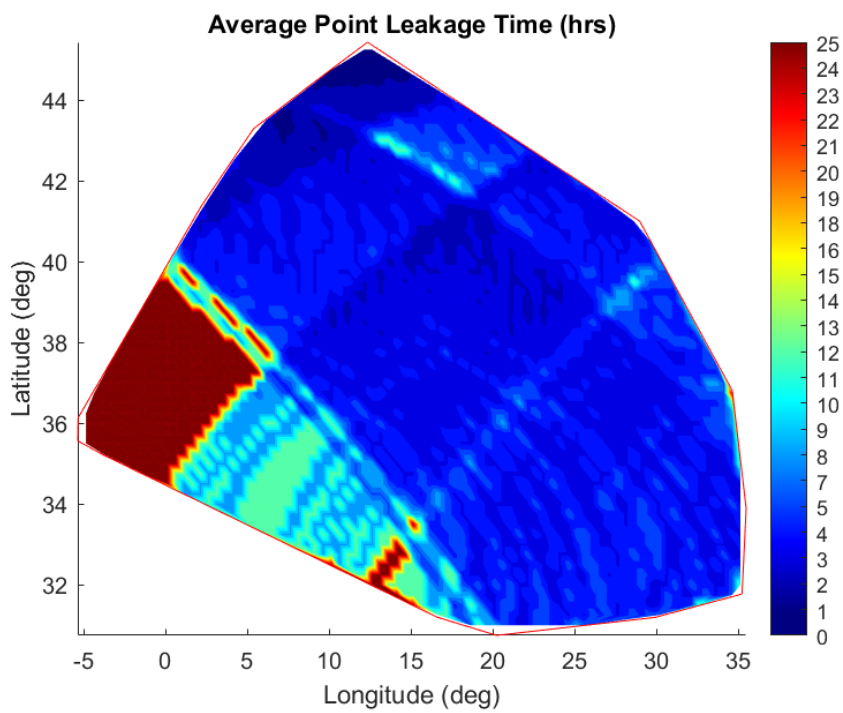
Figure 38: MOGA best individual 30km scan mode average leakage time per grid point in 24 hours
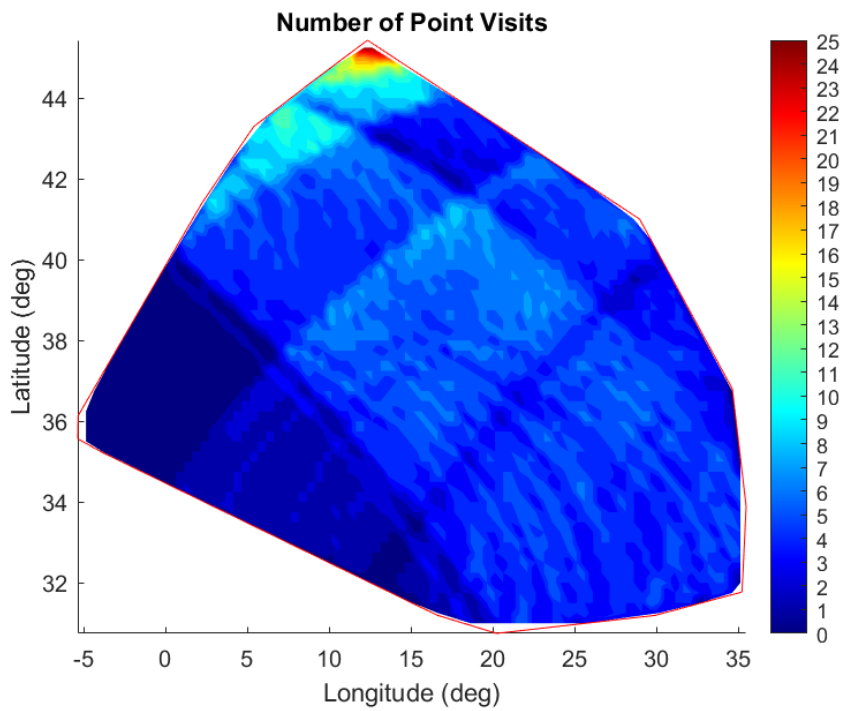
Figure 39: MOGA best individual 30km scan mode number of visits per grid point in 24 hours
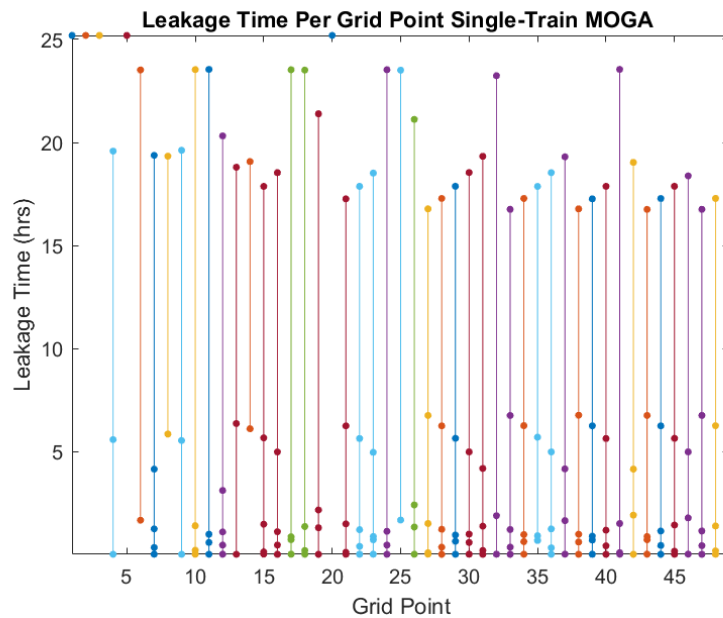
Figure 40: Single-train MOGA best individual leakage times per grid point. Each point represents an instance where the grid point was identified by the constellation. See 61 for numbering

7.2   CMWS Scan Mode

7.2.1   Best Designs

Of note is that the typical Pareto front shape is not clearly visible in all plots. This is likely due to a lower population than would be typically used for this search space size. Additionally, in the case of any plots showing area coverage results the shape of the Pareto front appears somewhat inverted. This is due to the usage of the term $\frac{1}{A_{cov}}$ in the minimisation instead of a negative value for area coverage. Whatsmore, as per section 5 each formation in this investigation case consisted of 15 satellites; 5 x 3-satellite formation flights flying in line.
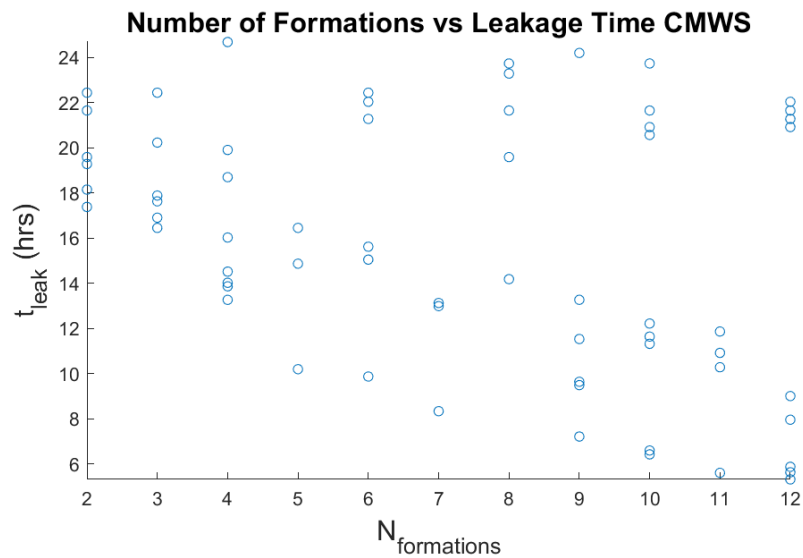
Figure 41: Plot of number of formations vs leakage time for CMWS configuration 150km swath scan mode
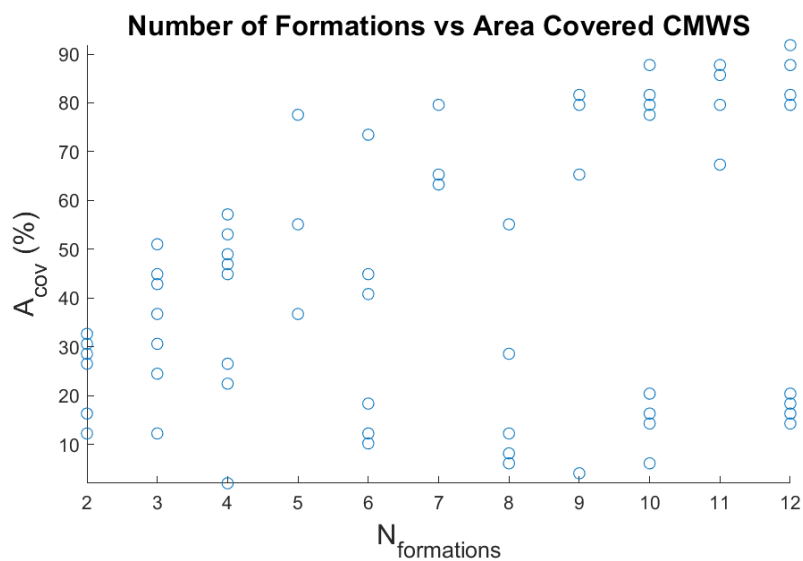
Figure 42: Plot of number of formations vs area covered for CMWS configuration 150km swath scan mode
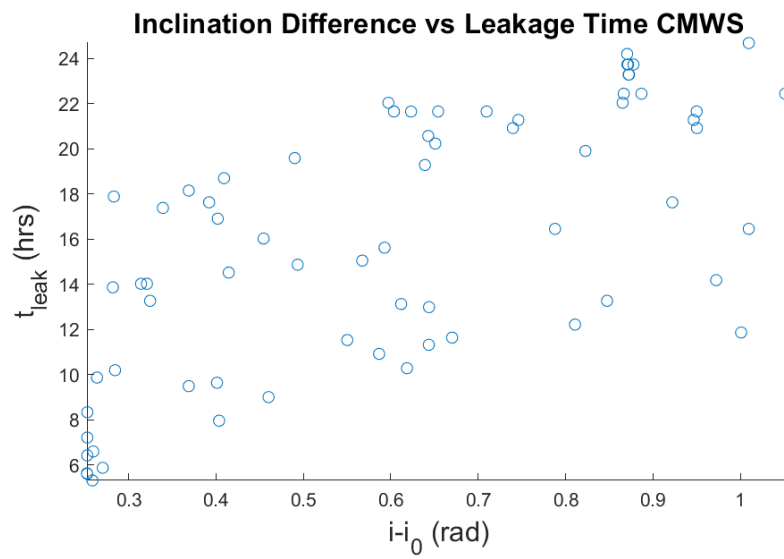
Figure 43: Plot of inclination difference vs leakage time for CMWS configuration 150km swath scan mode
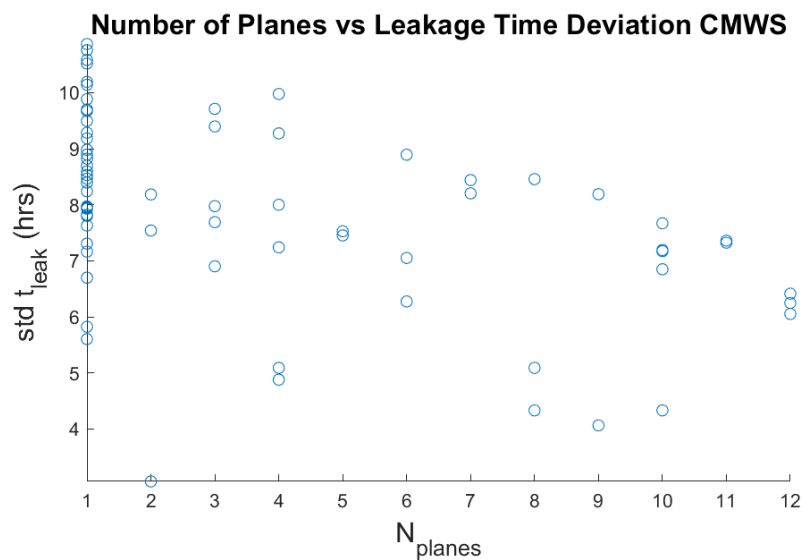
Figure 44: Plot of number of planes vs leakage time deviation for CMWS configuration 150km swath scan mode

Planes	i (rad)	Formations	Phasing Constant	$\Omega_0(rads)$	Mean t_{leak} (hrs)	Std t_{leak} (hrs)	$A_{cov}(\%)$
1	0.75403	12	1	5.7637	5.3189	7.9721	87.7577
1	0.74799	11	1	5.0145	5.609	7.9611	87.7577
1	0.74783	12	1	5.02E-07	5.6346	8.5314	81.6326
1	0.76585	12	1	0.43626	5.8761	7.9502	91.8357
1	0.74813	10	1	0.011444	6.427	8.5976	87.7577
1	0.75502	10	1	5.7679	6.5988	8.3971	87.7577
1	0.74816	9	1	0.062544	7.2163	8.9823	81.6326
1	0.89906	12	1	0.55988	7.9612	7.9306	79.5924
1	0.74821	7	1	6.2652	8.3377	9.498	79.5924
1	0.95566	12	1	0.7694	9.0072	7.8232	91.8357
1	0.86431	9	1	2.4148	9.4922	8.7	81.6326
9	0.89665	9	5	0.37874	9.6405	8.1892	81.6326
1	0.75934	6	1	5.7907	9.8719	10.193	73.4699
1	0.77996	5	1	4.9084	10.198	9.885	77.5494
11	1.1141	11	8	0.19475	10.283	7.361	85.7118
1	1.0822	11	10	1.3744	10.92	7.6289	79.5924
5	1.1391	10	2	0.69383	11.321	7.5288	79.5924
3	1.0457	9	2	0.94649	11.533	7.9759	79.5924
5	1.1657	10	9	0.53996	11.641	7.4537	81.6326
11	1.4965	11	4	5.221	11.865	7.3243	67.3491

Table 13: CMWS configuration scan mode MOGA results

7.2.2   Best Individual: Performance Over Target Area

As can be seen from table 13 the benefits of the CMWS mode are immediately apparent with better performance across the board for the same number of satellites used. Additionally, unlike in the single-train case several individuals were capable of meeting the individual performance requirements set. Performance of the best performing constellation across the target area for the simulated time period is presented in figures 46 and 47 respectively.
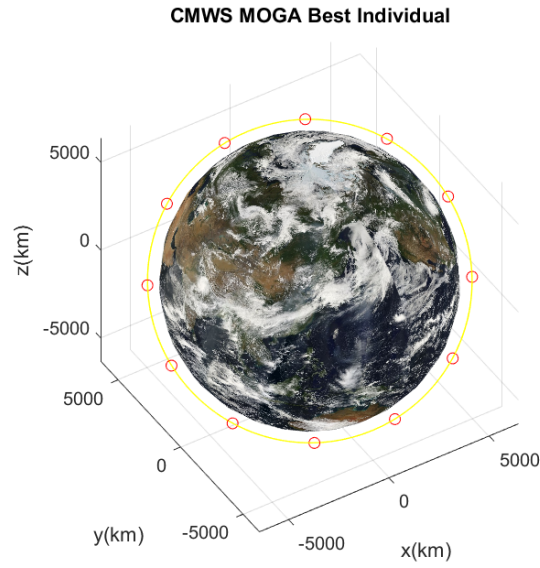
Figure 45: MOGA best individual CMWS scan mode constellation orbit plot

Mean t_{leak} (hrs)	Std t_{leak} (hrs)	$A_{cov}(\%)$	Satellites
5.35967	7.8503	88.3079	180

Table 14: Detailed performance numbers for best CMWS scan mode individual
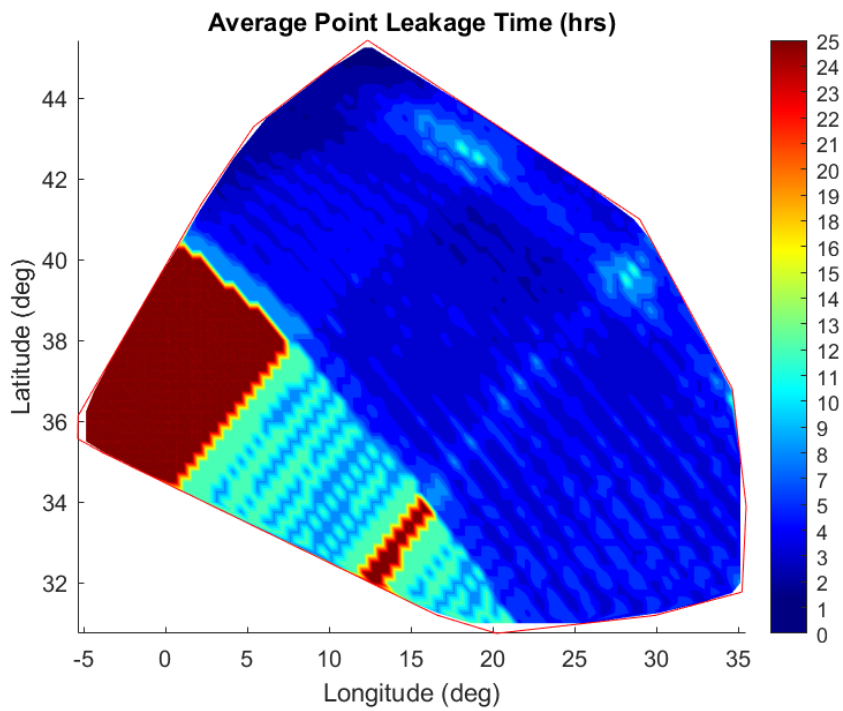
Figure 46: MOGA best individual CMWS scan mode average leakage time per grid point in 24 hours
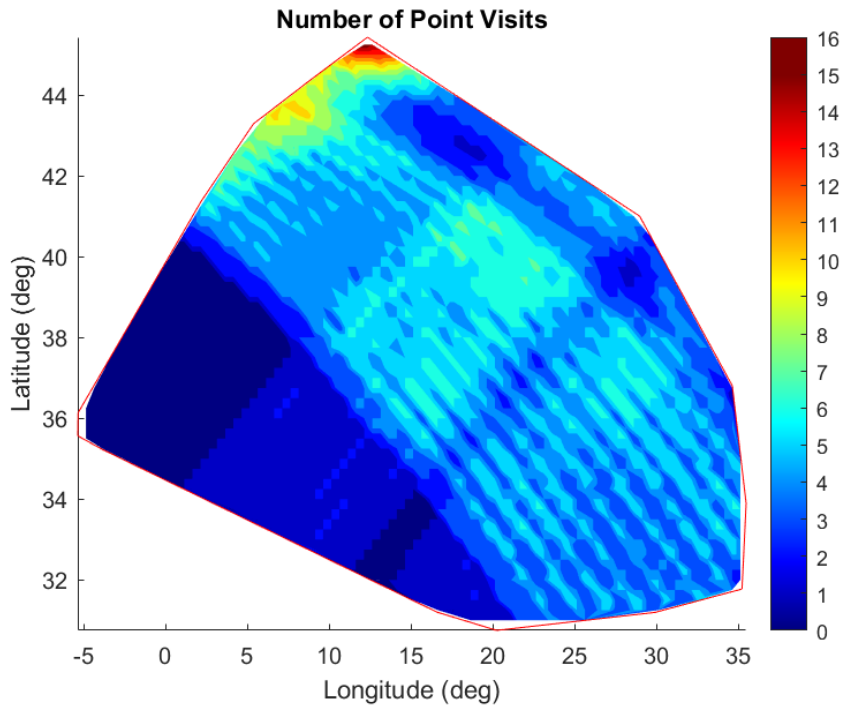
Figure 47: MOGA best individual CMWS scan mode number of visits per grid point in 24 hours
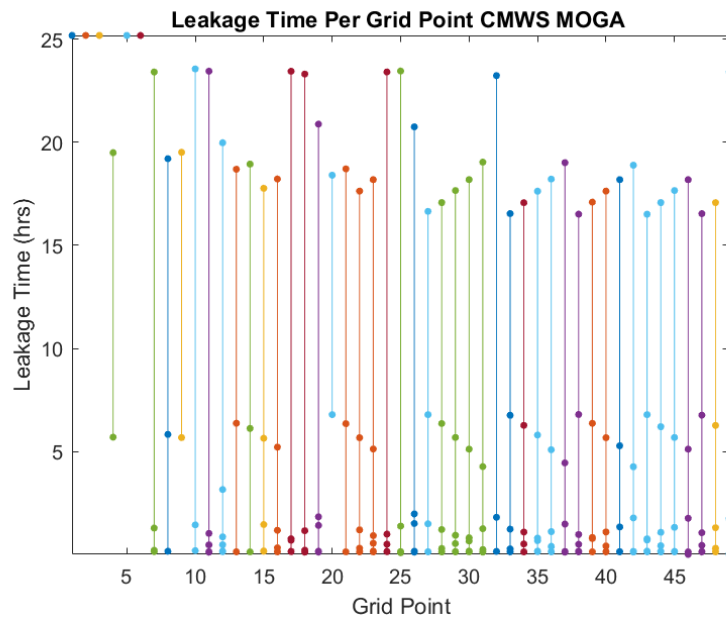
Figure 48: CMWS MOGA best individual leakage times per grid point. Each point represents an instance where the grid point was identified by the constellation. See 61 for numbering

7.3   Search Mode

Given the range of elevation angles reachable by the instrument, an equivalent instrument swath of 417.5614 km was calculated for the purposes of the MOGA constellation design. This was obtained by considering the ground range distance to the edge of the nearside edge of the beamwidth at the minimum elevation angle and the same distance to the farside of the beamwidth at maximum elevation angle. This equivalent swath was considered to be the same for both single-train and CMWS modes. This is because in the case of the CMWS mode, although the swath is wider it is composed of several instruments with the same elevation angle limitations as the single-train configuration. This means that the equivalent boresight of the CMWS swath has a restricted elevation angle range which, when combined with the increased swath width, produces the same equivalent swath as the single-train case.

7.3.1   MOGA Results

Planes	i (rad)	Formations	Phasing Constant	$\Omega_0(rads)$	Mean t_{leak} (hrs)	Std t_{leak} (hrs)	$A_{cov}(\%)$
1	0.76028	12	1	0.23904	2.3108	5.5222	93.8790
1	0.75742	12	1	0.14631	2.3549	5.5961	93.8790
1	0.7549	11	1	0.056014	2.503	5.7691	91.8357
1	0.75642	11	1	0.06337	2.5132	5.7475	91.8357
1	0.75289	11	1	0.00013204	2.5601	5.8852	91.8357
1	0.75594	10	1	0.084881	2.8564	6.1443	91.8357
1	0.7607	9	1	0.23105	3.2559	6.4863	89.7988
1	0.75449	8	1	0.024723	3.2732	6.4266	91.8357
1	0.7949	8	1	0.27916	3.5768	6.363	93.8790
1	0.78354	7	1	0.12636	3.9551	6.7963	89.7988
1	0.75658	7	1	0.20455	4.0996	7.266	87.7577
3	0.82754	6	1	0.47817	4.9163	7.2374	93.8790
5	0.77138	5	2	0.096587	4.9959	7.4803	91.8357
6	0.8242	6	1	0.1768	5.251	7.306	91.8357
1	0.75475	4	1	0.065361	5.6346	8.0103	91.8357
10	1.1627	10	1	4.0435	5.7395	6.0436	93.8790
5	1.1668	10	6	0.86665	5.9902	6.3039	93.8790
1	0.95408	7	1	0.67376	6.2322	7.0119	91.8357
1	1.5595	9	1	0.92867	7.0113	6.2156	89.7988
7	1.1385	7	1	3.8185	7.4336	6.4198	91.8357

Table 15: Search mode MOGA results

As is clear by table 15, the performance for similar products such as Capella X-SAR are quoted under the assumption of this kind of operational mode. With just 12 single-train formations operating in this manner a average target revisit rate of below 3 hours is possible. In some of the listed cases as few as 4 formations are required to achieve the minimum specified performance.
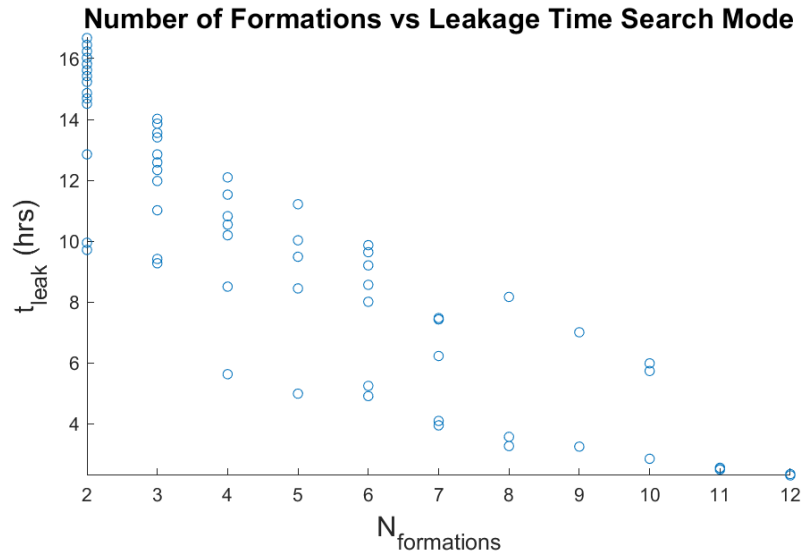
Figure 49: Plot of number of formations vs leakage time for search mode
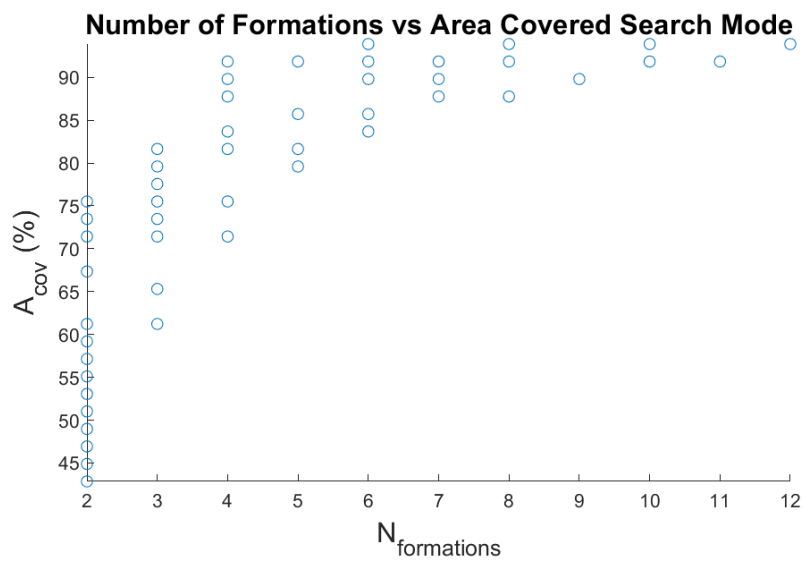
Figure 50: Plot of number of formations vs area covered for search mode
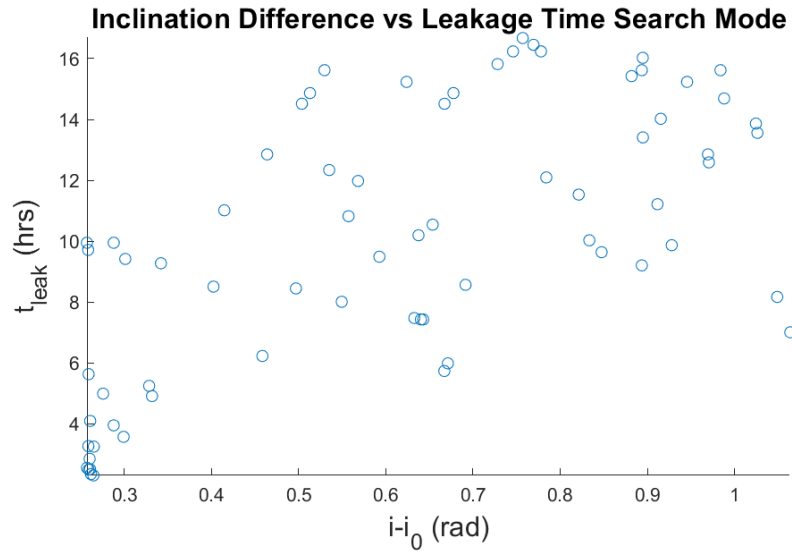
Figure 51: Plot of inclination difference vs leakage time for search mode
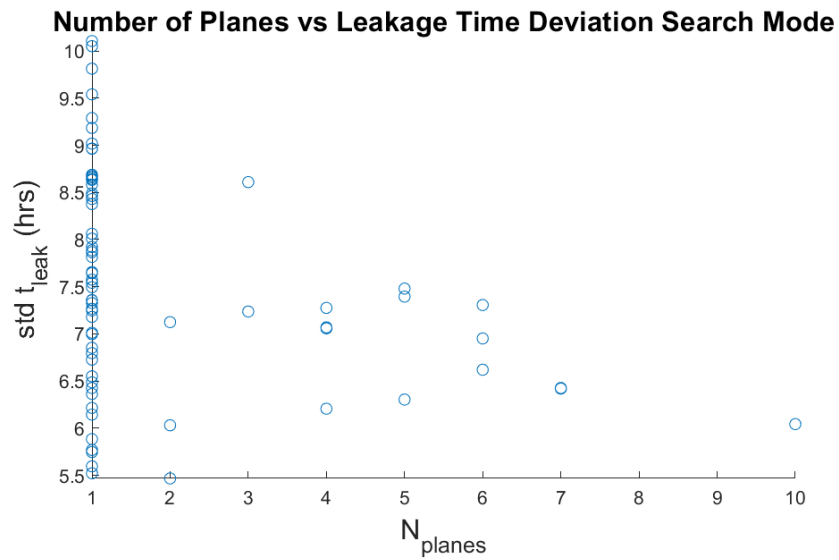
Figure 52: Plot of number of planes vs leakage time deviation for search mode

7.3.2   Best Individual: Performance Over Target Area

As is clear from figures 53 and 54 despite the increased performance across the target area there are still some points that the constellation does not reach in a 24 hour period. This would therefore lead the leakage time to be that of the simulation time at these grid points and thus result in the same max leakage time performance as all other combinations produced by the MOGA for this optimisation.

It is also worth noting that the area covered by this hypothetical 417km swath is not the same as that of CMWS and single-train configurations. This is obviously because the search mode constellation is made up of the same formation configurations as those explored in the scan-mode of operation. Rather, this area coverage represents the total area which could be covered by the swath of the formation instruments at the instantaneous point in time. The same logic is true for the leakage time standard deviation.

Mean t_{leak} (hrs)	Std t_{leak} (hrs)	$A_{cov}(\%)$	Satellites
2.3658	5.6147	91.68	180

Table 16: Detailed performance numbers for best search mode individual
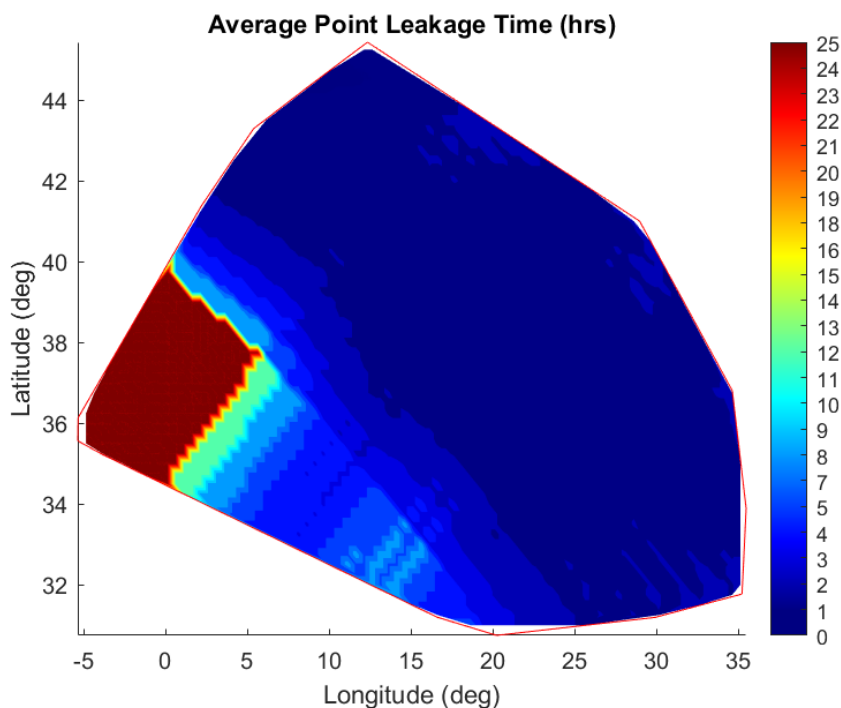
Figure 53: MOGA best individual search mode average leakage time per grid point in 24 hours
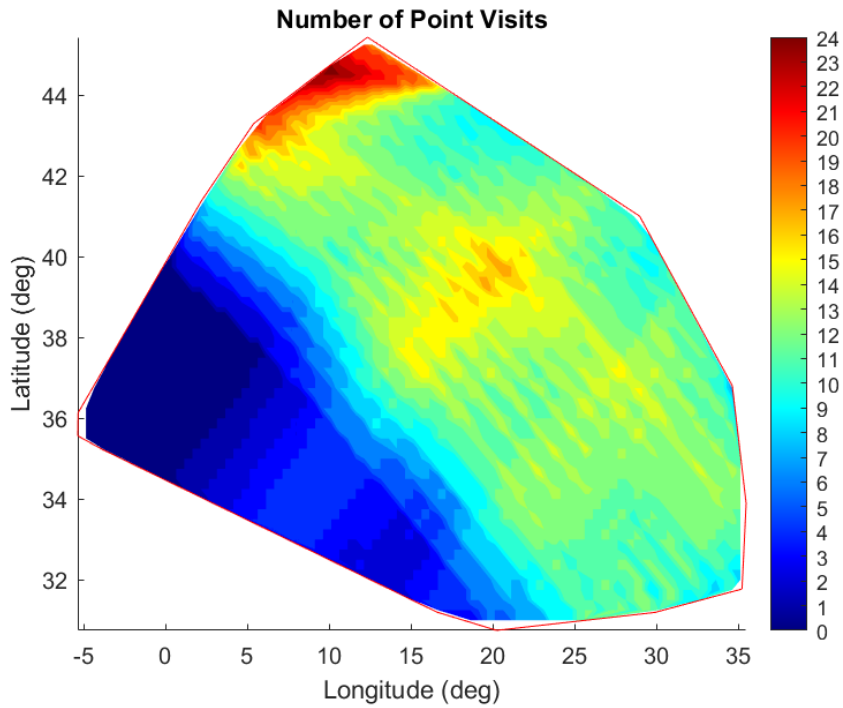
Figure 54: MOGA best individual search mode number of visits per grid point in 24 hours
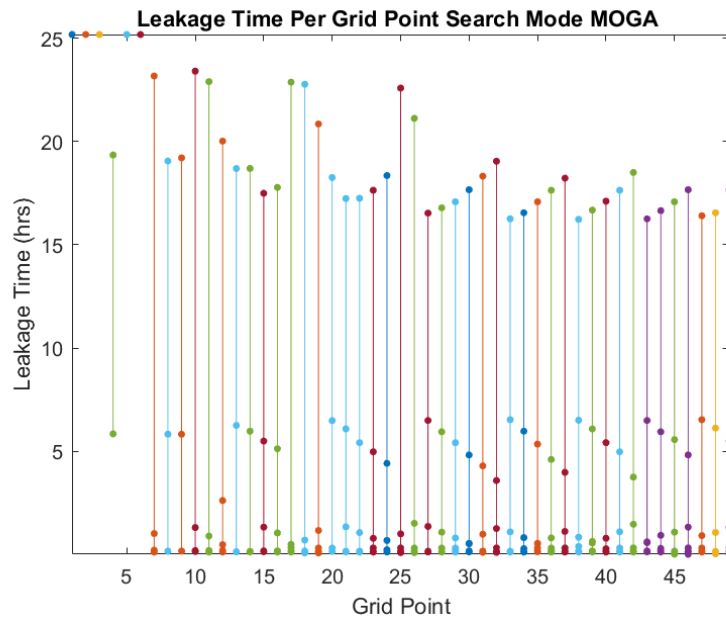
Figure 55: Search mode MOGA best individual leakage times per grid point. Each point represents an instance where the grid point was identified by the constellation. See 61 for numbering

7.4   Tracking Performance

7.4.1   Tracking Simulation

To contextualise the results obtained from the MOGA optimisation, the ability of each constellation to track a maritime vessel was investigated. A simple straight course was used for this application along with the parameters of a specific real-world vessel. The course plotted for tracking simulation was a simple East-West traverse of the target area in a straight line, starting from a randomly allocated point in the East of the target area. The vessel used for the case of the tracking was chosen to be the FRAMURA [90]; a 55 metre-long pleasure craft in the coaster class ported in Malta. The effects of currents and weather on vessel trajectory were not simulated due to the preliminary nature of this study. The vessel average speed was quoted as 12.5 knots. However, to account for the vessel maintaining heading under the effects of the currents and winds not simulated, as well as stops for pleasure purposes the vessel speed was taken to be half that at 6.25 knots.

As with the target area performance assessments, the simulation period was set as 24 hours and the properties of the target were set in accordance to table 1.
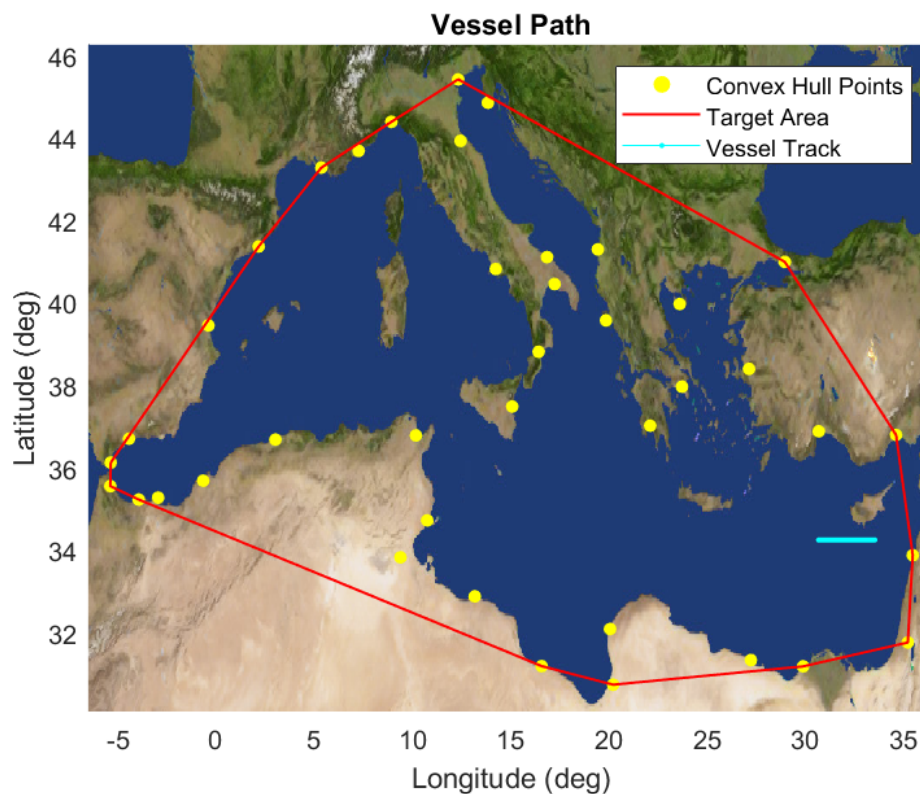
Figure 56: Simulated vessel path across the target area over 24 hours

7.4.2   Tracking Results

The tracking performance of each constellation is visible in table 17. Tracking performance was measured by average target revisit time, number of target visits and maximum positional uncertainty, with the latter calculated as per section 6.5.2.

Constellation	Target PIDs	Average Target Revisit Time (hrs)	Maximum Positional Uncertainty (km)
Single-train working point	6	4.7179	120.769
CMWS working point	6	4.7416	174.637
Single-train best MOGA individual	6	4.7172	215.916
CMWS best MOGA individual	6	4.7136	120.237
Search mode best individual	16	1.6064	89.546

Table 17: Tracking performance by constellation

8 Satellite Lifetime Calculation

8.1 Assumptions

To investigate the rate at which satellites in the constellation would need to be replaced, it was necessary to examine the lifetime of each satellite. For the purposes of this investigation the lifetime of the satellite was defined as the time after which the spacecraft could no longer maintain its own orbit using its on board propulsion system and successfully dispose of itself. As per the ESA recommendation on space debris [91], the spacecraft must re-enter the Earth within 25 years of mission completion. For this, it was also investigated if a set amount of delta-V was required in order to position the spacecraft to meet the ESA recommendations.

Satellite lifetime was examined for working point and scan mode solutions. Given that the search mode solutions were so close in orbital elements to the working point solutions it was assumed that they would decay at approximately the same rate.

As per table 7, the on board propulsion system for each satellite was specified to be capable of providing 25 m/s of delta-V total. It was assumed that the propulsion system could give impulsive manoeuvres and that neither the fuel nor the performance of the system degraded over time. Orbit maintenance manoeuvres were assumed to be given whenever the values of the semi-major axis, inclination or eccentricity exceeded 3-sigma from the original prescribed orbital elements. The standard deviation value was applied considering that of the Sentinel-1 values as a guideline [80]. Each satellite in each formation was assumed to perform orbit maintenance manoeuvres in the same way at the same time so as to avoid collisions and negate the requirement to design a controller to ensure orbital spacing was maintained (which was deemed to be outside of the scope of this work). In addition, it was assumed that each satellite in the constellation over the course of its lifetime would be effected by the perturbations in approximately the same way. Therefore only one simulation had to be run for a single satellite per constellation. Each simulation was run until the satellite altitude reached 100km, as crossing the Kármán was assumed to result in the re-entry of the spacecraft. Finally, as per the discussion in section 4.2.7, no budgeting for phasing or insertion was accounted for at this stage of the design for the propulsion system.

8.2   Perturbations

For the purposes of the analysis, GMAT was used [92]. The tool simulates all possible perturbations of interest, giving an accurate indication of the lifetime of a satellite in the constellation. Inputs to GMAT for perturbations were set exactly as in section 6.3. Additionally, all major bodies in the solar system bar the moon were chosen to be point masses without complex gravity fields.

8.3   Operational Lifetime and Orbit Decay

Calculations on lifetime were made by propagating the orbit of a satellite in the given constellation until such a time that any of the 3 orbital elements of interest exceeded the allotted threshold value. At this point, a manoeuvre was given and the delta-V required to restore the original values of inclination, semi-major axis and eccentricity was calculated. Inputting the values associated with the propulsion system chosen in section 4.2.5 and assuming satellites in formations were launched at the same time, the operational lifetime of each formation was obtained. As per the -04 designation model of the thruster chosen, 1.314 kg of fuel was assumed to be on board. To keep GMAT from stepping into negative fuel values a small reserve was assumed to be kept in the fuel tanks of 2-3% of the original fuel mass.

Each of the working point constellation formations have the same orbital elements except of course for the true anomaly and nodal right ascension. As such only one analysis was done for this case. Each of the operational lifetimes and decay times for formations in each constellation combination are displayed in table 18. Due to the solutions being similar in their orbital parameters, only one set of plots for fuel mass and altitude over time are displayed in this section. The altitude and fuel mass over time for the other two cases can be found in appendix A (10).

Case	Operational Lifetime (MM:DD:HH:MNMN:SS)	Orbit Decay Time (MM:DD:HH:MNMN:SS)
Working point	3:10:16:00:28.799	7:18:20:3:50.4
MOGA single-train	3:8:21:46:4.8	7:18:4:24:57.6
MOGA CMWS	3:8:18:48:57.6	7:13:18:59:2.4

Table 18: Operational lifetime and orbit decay time of each constellation with station keeping

As seen from figure 57 and table 18 respectively, the orbit of every satellite in the constellation should decay well within the 25 year limit even with the operational period included in that time span.
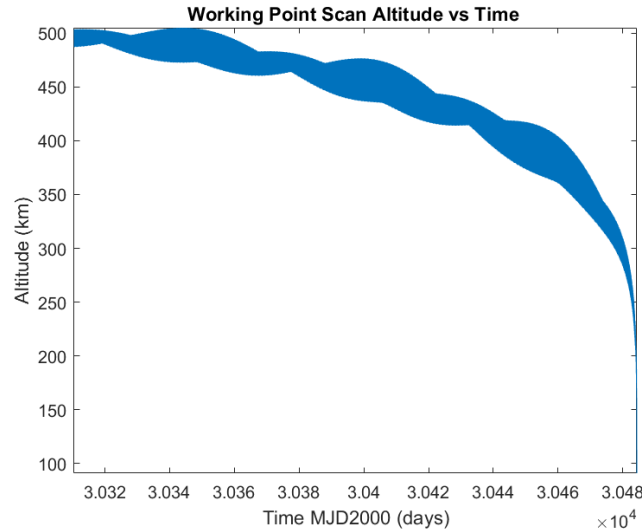
Figure 57: Working point orbit altitude with station keeping over time

The operational lifetimes in table 18 show that a cold gas thruster like the VACCO is unlikely to be the best choice for a constellation like this. Considering that similar spacecraft such as ICEYE-X1 or Planet Doves have a service lifetime of 1-3 years [93] [94], the 3 months achieved with this propulsion solution is inadequate.
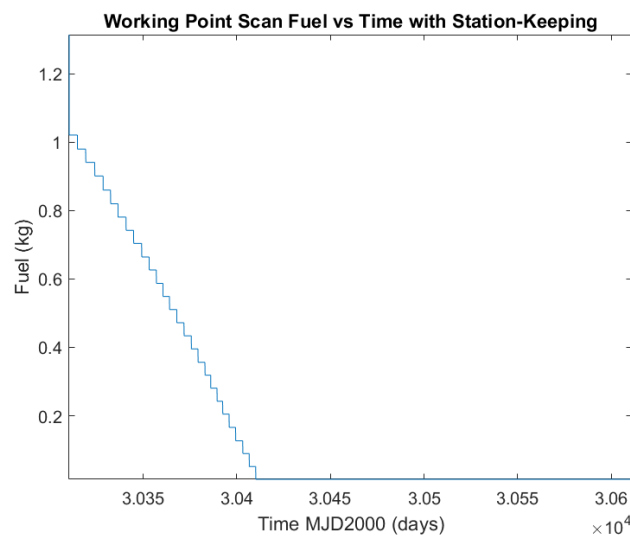
Figure 58: Working point constellations fuel mass with station keeping over time

The simplicity and low-power consumption of the cold-gas thruster has reliability benefits that more complex systems may not have, which is why it was chosen for this examination. However, in this case an electrical propulsion solution would be more suited from the service lifetime standpoint. A compact solution like that of the Enpulsion R^3 could deliver 10 times the delta-v in the same form-factor [95], leading to a comparable lifetime to that of ICEYE-X1 or Planet Doves.

9   Discussion

9.1   Comparison of Single-Train, CMWS and Search Mode

The Pareto plots of the three investigations for the two most important parameters (leakage time, area coverage) are summarised in figures 59 and 60 respectively.
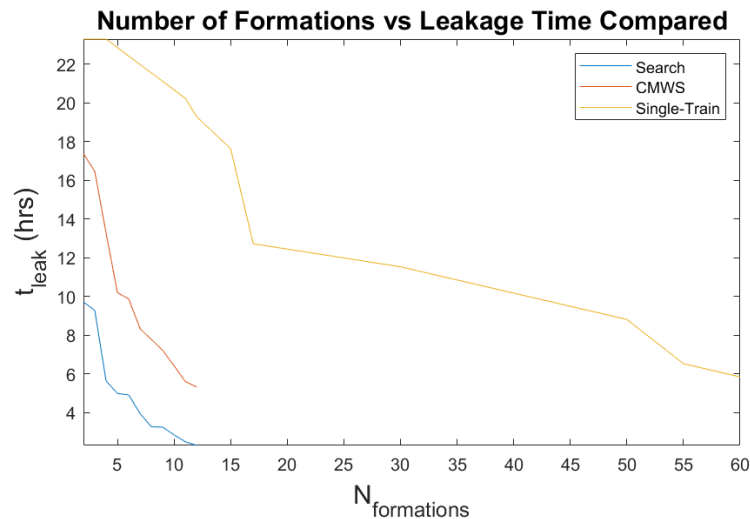
Figure 59: Combined Pareto plots of leakage time vs number of formations
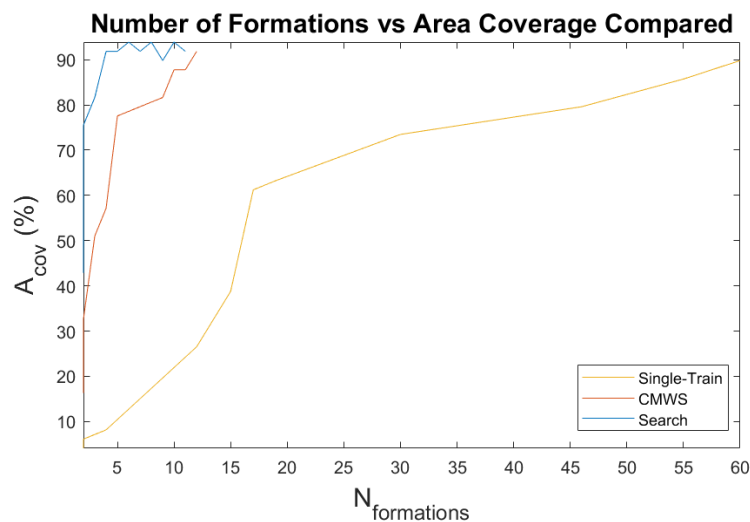
Figure 60: Combined Pareto plots of area coverage vs number of formations

9.1.1   Single-Train vs CMWS

The benefits of CMWS over single-train are immediately apparent from the summaries above. The CMWS configuration allows to achieve significantly better performance at the lower end of the number of formations used versus the single-train configuration. This means that with as few as 10 satellites (2 formations of 5 CubeSats) in CMWS configuration, the revisit performance of the ICEYE constellation at the equator (outlined

in section 6.5.1 could be matched. Using a single-train solution, this would require 45 satellites (15 formations of 3 CubeSats) for the same performance.

This benefit is even more pronounced in area coverage as seen in figure 60. This result was expected due to the wider swath imaged, where 25 satellites (5 formations of 5 CubeSats) in CMWS configuration cover an area which can only be matched by 126 satellites (42 formations of 3 CubeSats) in single-train configuration. This represents an almost 5-fold reduction in the number of satellites required for the same level of performance at lower coverage levels especially when using CMWS configuration formation flights.

9.1.2   Scan Mode vs Search Mode

As is also clear from both figures 60 and 6.5.1 that search mode produced the best performance of the two operating modes, as expected. Using this operating mode allows for significant performance gains, especially with respect to point leakage time. Leakage times less than half of scan mode solutions using an equivalent number of satellites were observed from the resulting investigation. Of course, operation in this mode would require supplementary information so that the spacecraft would know where to slew its instrument. As such, when considering an isolated system which does not communicate with competitors and looks to replace services like AIS for example, this mode of operation (and thus the solution) may be less feasible.

9.2   Best Individuals Performance

Considering the single-train case, the leakage time deviation was approximately 8 hours for the top 20 individuals. This significant deviation was expected for this configuration, because as seen in figure 39 not all points are visited by this constellation in set simulation time frame. It was anticipated that due to the fixed pointing and small swath size that this would be the case, even with as many as 60 formations leveraging 180 satellites.

This improved for the CMWS mode, with most deviations in the order of 7 hours as opposed to 8. However, this improvement was not as stark of a contrast compared to the single-train results. This was clearly due to the points which were not visited in the simulation time period significantly impacting the average leakage time across the target area. This can be seen for the single-train configuration best MOGA individual in figure 40 with figure 61 provided as a reference for the appropriate grid numbers.

9.3   Single-Launch Performance

9.3.1   Single-Train Scan Mode

Inferring from the Pareto fronts in section 7.1.1, a single launch constellation solution operating in single-train configuration could not meet the minimum requirements set out at the beginning of this work. It would instead have a leakage time in the order of 20 hours, similar to what is stated for ICEYE's equatorial revisit time in Strip Map mode which uses a similar number of satellites with a similar swath size [41]. This served to further validate the performance evaluation procedure used in this investigation.

Beyond this, the area coverage would be in the order of 20-30% and a minimum leakage time deviation of 5-6 hours. As expected, the single-train scan mode single-launch Walker
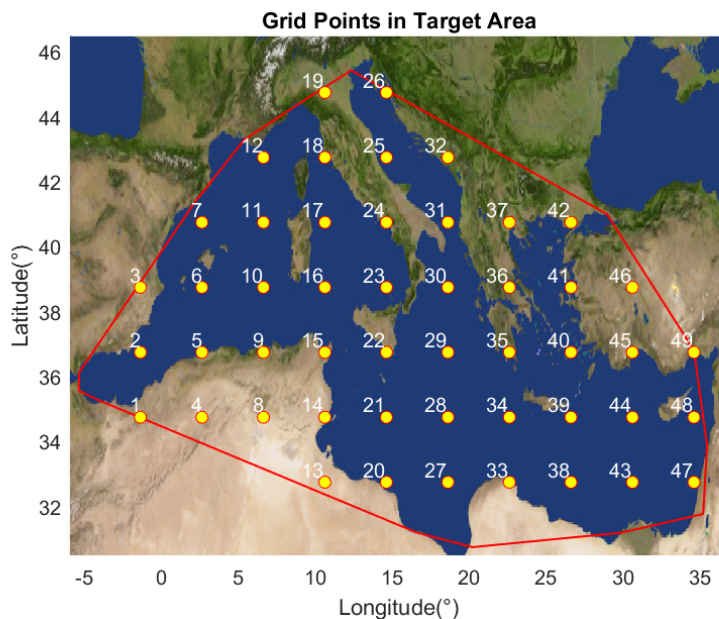
Figure 61: Reference image showing location of each grid point referenced in figure 40

constellation solution would therefore perform the worst of the 3 possible single launch solutions explored in this work.

9.3.2   CMWS Mode

A single-launch CMWS mode constellation would be constrained even further in the number of formations which could be deployed due to the 3 spacecraft formation size and the 5 formation-strong flight used to produce the 150km swath. In this case, each formation consists of 15 satellites and so only 2 formations could be completed with a single launch, with a leftover space of 6 satellites on the launch vehicle. It is possible that this space could be filled with 2 additional formations operating in single-train 30km swath mode, however this possibility of mixed mode constellations was deemed to be outside of the scope of this work.

Inferring from the Pareto plots in section 7.2.1 single-launch CMWS constellation would be capable of achieving revisit rates in the order of 17-18 hours, with an area coverage of 35% at maximum. This would be obtained with a leakage time deviation in the order of 3 hours at best.

9.3.3   Search Mode

As previously discussed, the slew capability of a SAR instrument is what gives the platform a much higher imaging revisit rate than the ground track repeat time of the spacecraft on which it is mounted. As a result it is no surprise that almost all of the constellations from the 20 Pareto points listed in table 15 are capable of meeting the minimum prescribed performance. Under the assumption of this active slew-to-image mode of operation any of these constellations proposed could be implemented using single-train or CMWS configurations. These configurations could achieve the performance of the best individual generated even with just a single launch worth of spacecraft.

9.4   MOGA Performance

With a tolerance of 1e-6 the MOGA ran out of generations before stopping due to the tolerance criterion. Given the size of the search space, the opting of accuracy over compute speed and the limited computational power available this was somewhat expected. Despite this non-ideal optimisation performance, several workable solutions to the problem posed were obtained which all improved in some way upon their manual iteration counterparts. These solutions performed similarly or in some cases better in terms of point revisit time to current commercial solutions. Despite this, improvements in the computational efficiency of the simulation algorithm enabling usage of a larger population and thus better convergence is foreseen as part of future works. This larger number of individuals leading to improved convergence would likely also address the "cloud of points" behaviour shown in several of the Pareto plots, where a quadratic curve shape is expected instead.

9.5   Favoured Inclinations

As can be seen in tables 11, 13 and 15 inclinations for designs favoured by the MOGA appeared to be around the minimum inclination. For the single train configuration this value was 0.7447 radians. This was indeed expected as the target area is larger in longitude than it is in latitude. This means that a ground track diagonally crossing as close to horizontally as possible (while still reaching the minimum latitude necessary to access all of the points as set in section 4.2.9) would be most suitable for visiting the majority of points in the area.

9.6   Impact of Using Walker Constellations

Combinations utilising significantly more planes showed a notable decrease in leakage time deviation as expected due to the dispersed planes increasing the ability of simultaneous area visits by the constellation. The restriction of the Walker constellation design is likely why combinations with 2 or 3 planes are were favoured by the MOGA. Within the set simulation period of 24 hours, the separation of 120-180° between orbital planes of these combinations appear to perform significantly worse than simply adding more satellites to a single plane. Additionally, the setting of the number of planes as a variable for minimisation in the optimisation process also plays a significant role in which combinations are favoured.

It is possible that removing this inter-plane spacing constraint would produce constellations which are more efficient at visiting the target area. However, this would add an additional degree of freedom to the problem, widening an already large search space. This larger search space would require a larger population to be explored efficiently within a similar number of generations. Regardless, combining this with further algorithm refinements and perhaps a semi-analytical approach to the problem could conceivably balance the issue of the increase in required compute time.

This was expected as a limitation of using this global coverage pattern for a regional application, even considering the size of the target area in question. Future works could capitalise on this limitation by examining possible improvements using a regional coverage pattern. The results of this work could be used to set the bounds for a regional pattern investigation, with the expectation that such a solution would likely require less satellites to achieve similar if not better performance across the target area.

9.7   Impact of Simulation Period

The impact of the simulation period and time step chosen on the results favoured by the genetic algorithm was indeed expected, however due to the search algorithm implemented (as outlined in section 6.3 the simulation time was somewhat restricted. To increase the simulation time one would have to increase the time-step used for calculations so as to achieve a similar compute time. Given the likelihood of this causing the simulation to 'skip' the satellite over the target area, the accuracy of the performance prediction would be significantly impacted. This can be seen in the improvement in predicted performance in the manual constellation performance analysis conducted in section 7.1.2, where the average leakage time of the best individual is lower than its listing in section 7.1.1.
For this reason, the impact of the simulation period was simply acknowledged as a penalty of this implementation which could be improved in future works. Regardless, the benefit of increased number of planes was seen to be that of decreased leakage time deviation. This would obviously be important for a case where a maximum revisit time is imposed on the solution, which as discussed before is not the case in this work.

9.8   Preferred Solution

It is clear from section 7.3 that the search mode provides the best performance for any constellation solution. Combining this operational mode with the CMWS configuration would produce the best results for maritime surveillance in this case due to the wider swath imaged and thus the greater capacity to track multiple vessels in a set area without having to re-point (as is done with NOVASAR-S' maritime monitoring mode [37]). That being said, for single point imaging operating a single-train configuration constellation under the specifications of the 14th row of the search mode best individuals represents the minimum satellite constellation capable of providing the prescribed performance.
However, for maritime surveillance purposes generally the location of the vessels at sea are not known a-priori. This case would only arise if the product was using supplementary information from a service such as AIS or perhaps imaging data from other constellations or search and rescue services. This last-known location information is what would enable the search mode but without it the constellation would have to operate in a scanning mode. It is likely that some degree of instrument pointing in the nominal scan mode surveillance case would be adopted so as to maximise the amount of time that each instrument beam spent in the target area as is not done in this work. Considering all of this the best performing solution would be that of the CMWS configuration's best individual operating in a search mode.

Parameter	NovaSAR-S	Sentinel-1	Capella X-SAR	ICEYE-X1	CMWS Search
Satellites in constellation	3	2	36	18	180
Point revisit time (hrs)	14.4	48	≤ 1	20	2.3658
Swath width (km)	20	80	5	30	150

Table 19: Proposed solution performance compared to industry offerings in StripMap mode [40], [45], [42].

As seen in table 20 this solution performs competitively against existing offerings such as Capella X-SAR and ICEYE in terms of revisit rate while eclipsing both in swath size. As neither of the aforementioned services offer a dedicated maritime surveillance mode it is not possible to compare tracking results. However, it is foreseeable that the increased swath size could compensate for the revisit performance advantage that Capella and IC-EYE have over the CMWS search mode solution by allowing better multi-vessel tracking. This should also be investigated as part of future works.

Parameter	NovaSAR-S	Sentinel-1	Capella X-SAR	ICEYE-X1	CMWS Search
S/C mass (kg)	400	2300	40	85	25
Frequency (GHz)	3.1-3.3	5.405	9.4-9.9	9.65	9.45-9.75
Peak power (W)	1800	4800	600	3200	400
Polarisation	quad	quad	HH	VV	VV
Antenna dimensions (m X m)	3 X 1	12.3 X 1.02	3.5 (circular, $\varnothing$)	3.2 X 0.4	2.2 X 0.5
Max bandwidth (MHz)	200	100	500	299	100
Duty Cycle (%)	2	12	10.4	4.6e-3	$\leq$15
Orbit altitude (km)	580	693	485-525	560-580	500
Mean Power (W)	36	576	62.4	14.72	42.8892

Table 20: Proposed solution detailed parameters compared to industry offerings [40], [45], [42].

Despite the significantly higher number satellites used for the constellation population, performance is approximately on par if not better than competing solutions. This is to be considered alongside the benefits of redundancy, flexibility and robustness offered by the formation flight configurations.

9.9   Working Point Comparison

Comparing the outcomes of the MOGA with the working point configurations establishing in section 6.6.1, it is clear that both the single-train and the CMWS configurations conceived by the MOGA are improvements over their working point counterpart. In the case of the single-train configuration, the major improvement is that of the mean revisit time. This was improved by almost 1 hour compared to the working point solution for only a 5 formation, 5 plane penalty. Additionally, a planar inclination reduction of 0.0215 radians was achieved.

The CMWS optimisation produced better results in terms of number of planes, inclination difference, mean leakage time and leakage time deviation while providing approximately the same area coverage against its working point counterpart. A reduction of 10 orbital planes, 0.01217 planar inclination and approximately 0.3 hours in revisit time were obtained for only a single formation more.

9.10   Single-Plane Solution Risks

Something that is noteworthy is that the best solutions produced by the algorithm for search mode and the CMWS configuration employ only a single orbital plane. As discussed in section 9.6 this is likely due to the combination of the simulation time, the Walker constellation constraint and the plane minimisation goal of the optimisation algorithm. The bi-product of this is that the the satellites in the same plane are all exposed to similar collision risks in the event that a self-collision occurs between spacecraft formations. This collision risk compounds with each formation effected due to Kessler Syndrome [96]. The risk also stands in the case of other orbital debris impacting the constellation.
Additionally, with an event such as this occurring the entire service would be disrupted due to the requirement of all spacecraft in the orbital plane to manoeuvre to avoid the debris cloud. Taking this into account, a multiple plane solution may be preferable so as to provide redundancy in the service planes and reduce the service risks. This should be analysed as part of the risk analysis for the service access guarantee sought after the product the constellation seeks to provide is defined in more detail.

9.11   Tracking Performance

The tracking results obtained for each constellation give a high-level insight into the benefits of CMWS for maritime tracking applications. Of all of the constellations simulated, only the 3 of the 5 were capable of meeting the minimum positional uncertainty of 166 km. The CMWS solutions show similar revisit times to the target as was expected from the performance measured in sections 7.2.2, 7.1.2 and 7.3.2 respectively. The main benefit of the wider swath is clearly the reduced maximum revisit time and thus positional uncertainty. This is compounded by the fact that the circular search area (constructed from the last known location of the vessel, its speed and the time elapsed since last identification) assumed for by this tracking algorithm would likely be reduced in size in reality. Adjacent formations passing near the true location and within the area of uncertainty would reduce that area of uncertainty as part of that area would then be considered as searched. Obviously a larger part of this area is searched by a wider swath and so this reduction would be greatest while operating in CMWS configuration.
It is obvious that as discussed, the search mode requires prior knowledge of the target before it can be used. In the case of tracking, it is possible that having first identified a vessel in scan mode a formation could pass the last known location information to the next formation entering the target area. This would enable the operation of that search mode along with the benefits in revisit time and positional uncertainty. CMWS configuration also allows for the tracking of more vessels due to the wider swath, something which is not reflected in this single-vessel tracking simulation. It is expected that the performance difference between CMWS and single-train modes would become more apparent when considering multi-vessel tracking, which should be undertaken as part of further works.
What is of interest is that the single-train working point constellation was capable of almost matching the performance of the CMWS MOGA best individual. In this case the significant increase in the number of orbital planes used compensates for the narrower swath used by the single-train configuration, allowing it to be the only constellation of this configuration to meet the minimum tracking requirement set. It is possible that while this is a more robust solution from the collision avoidance and traffic management point of view, the number of planes which need to be populated in setup and maintenance of the constellation may be result in it being a less favourable solution from a cost point of

view. Again, this is part of a trade-off analysis which must be done at a later stage by the designer for their specific needs.

9.12   Constellation Lifetime

Using the specified cold-gas thrusters, the constellation would only have an operational lifetime of approximately 3 months. Competing solutions such as ICEYE use electrical propulsion systems to achieve much higher service lives, as discussed in section 8.3. It is possible that a longer operational life could be achieved with the cold-gas thruster by increasing the orbital height, which would reduce the impacts of one of the most significant perturbations (drag). However, the trade-off in this case would be that a higher instrument power would be required for the same SNR due to path losses being proportional to the cube of the return distance. Whatsmore, higher orbits are more difficult and thus more costly to reach, making constellation maintenance a more difficult undertaking. This trade-off analysis is something which could be conducted in more detail in future works.

10   Conclusions

This work presented the preliminary design of a MIMO CubeSat SAR constellation for maritime surveillance over the Mediterranean using a multi-objective genetic algorithm (MOGA) and a set of prescribed performances and constraints. A genetic algorithm is a type of optimisation method based on Darwin's theory of natural selection.

The constraints were obtained from literature and a survey of similar active services as well as some which are still in development. The benefits of MIMO CubeSat formations over single monolithic satellites were detailed and a minimum formation capable of achieving the set performances was sized. All formations were assumed to fly in SAR trains.

The performances of interest for the constellation were set to be the point leakage time, the leakage time deviation, area coverage, number of satellites and planes used and finally the difference in inclination of the orbital planes from the minimum launcher inclination at lift-off.

Genetic algorithms usually explore large search areas, so a set of simplifying assumptions were necessary to avoid hundreds of hours of compute time. In this work, Walker patterns were assumed for the constellation to simplify the design process. Walker constellations are usually used for global coverage, but have been used to design for coverage of large regions in existing literature.

This simplification offset the choice of an accurate orbit propagator and instrument geometry which were considered to provide a more meaningful insight into the performance of each constellation proposed. Simulations for the MOGA were run for a 24 hour period at a time step of 60 seconds. A population of 200 and 100 generations were also used. The combination of these choices resulted in some constellations which were single plane only and likely to perform poorly on a global scale while barely meeting regional performance requirements in most cases.

The performance of a set of manually configured working point simulations was compared to the best individuals produced by the MOGA across the set target area as well as in a simulated vessel tracking scenario. One fixed instrument pointing mode of operation called scan mode was considered for 2 possible formation configurations: a single-formation flight covering a 30km swath (single-train) and a larger formation called CubeSat MIMO Wide-Swath (CMWS) covering a 150km swath. The performance of a second operational mode where the instrument could slew to the target (called search mode) was also investigated. After this, the operational lifetimes of the conceived constellations were analysed using the General Mission Analysis Tool (GMAT) from NASA to determine the rate at which satellites in the constellation would need to be replaced. Each spacecraft was assumed to have a cold-gas thruster providing 25 m/s delta-v which proved to be insufficient for sustaining the constellation operational lifetimes to the degree of competitors. An electrical propulsion system was instead recommended.

In analysing the results, the benefits of CMWS over single-train operation became clear. The ability to cover larger swaths at the same time led to a reduced positional uncertainty in vessel tracking and better leakage time performance across the target area versus the single-train counterparts for the most part. This resulted in more of the top-individuals from the final generation meeting the minimum constellation performance with less satellites than similar single-train solutions. In general, utilisation of CMWS formation flights enabled the achievement of a set constellation performance with fewer CubeSats used. Figures 59 and 60 illustrate this and are reproduced here for convenience.

Similarly, as expected the MOGA produced constellations which out-performed the man-
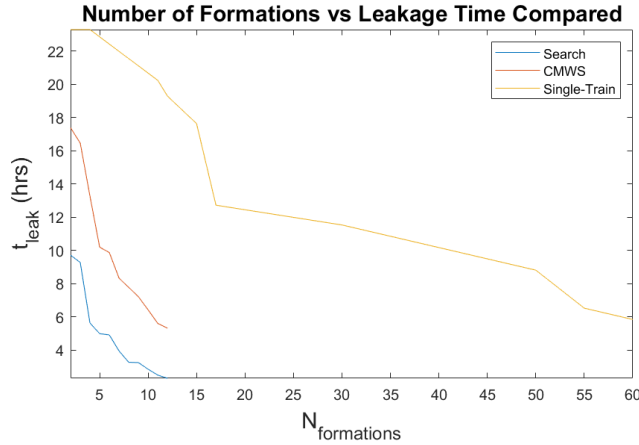
Figure 62: Reproduction of combined Pareto plots of leakage time vs number of formations
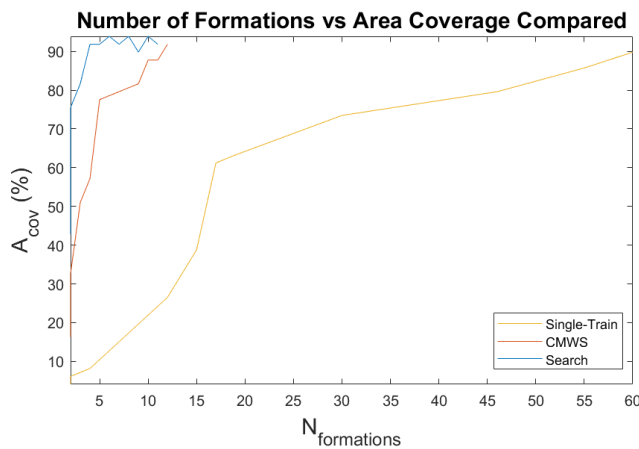
Figure 63: Reproduction of combined Pareto plots of area coverage vs number of formations

ual iterations across the target area. The search mode constellation performance eclipsed those of the scan modes as expected, but this type of operating mode requires supplementary knowledge of target locations in order to work. This may not always be available for maritime surveillance constellations and so may be less preferable as an operating mode in the end. Assuming search mode was possible, the ideal solution was that of the best search mode MOGA individual operating CMWS formations. Its performance compared to industry offerings is demonstrated in table 20 and reproduced here for convenience.

Parameter	NovaSAR-S	Sentinel-1	Capella X-SAR	ICEYE-X1	CMWS Search
Satellites in constellation	3	2	36	18	180
Point revisit time (hrs)	14.4	48	≤1	20	2.3658
Swath width (km)	20	80	5	30	150

Table 21: Reproduction of proposed solution performance compared to industry offerings in StripMap mode [40], [45], [42].

Future work should endeavour to improve the computational efficiency of the algorithm used such that a larger population and number of generations could be used for the same search time. This could be done by semi-analytical methods or otherwise, the benefit of the former being that the impacts of different parameters on constellation performance would be more visible and easier to interpret. The results of this work may also be used as the boundaries for a regional design investigation leveraging streets-of-coverage constellation patterns. These patterns could possibly produce constellations which perform better with fewer satellites. In any case this work has provided a working point for further investigations for constellations leveraging promising developments in CubeSat formation flight and distributed SAR systems, while giving a tangible insight into the performance which could be expected from such a constellation.

Appendices

Appendix A
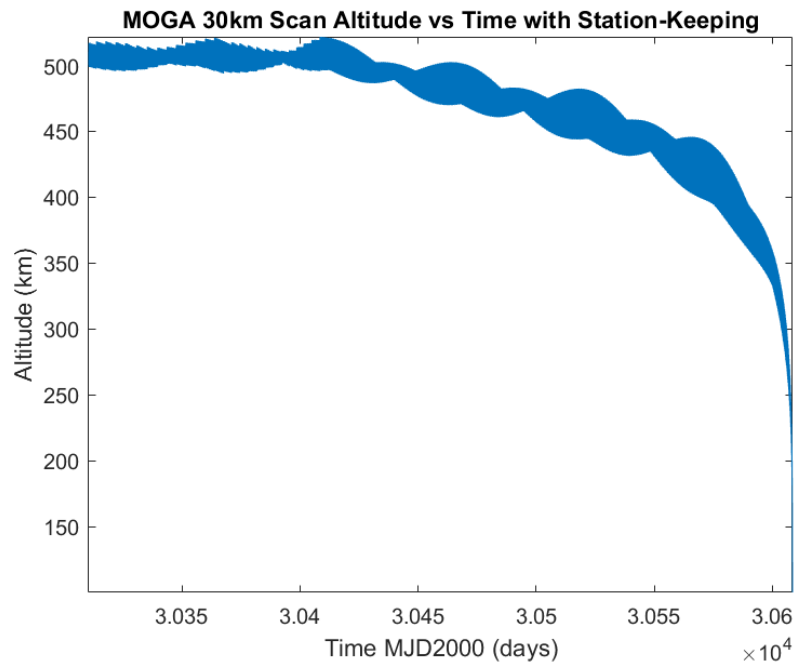
Figure 64: MOGA single-train best individual orbit altitude with stationkeeping over time
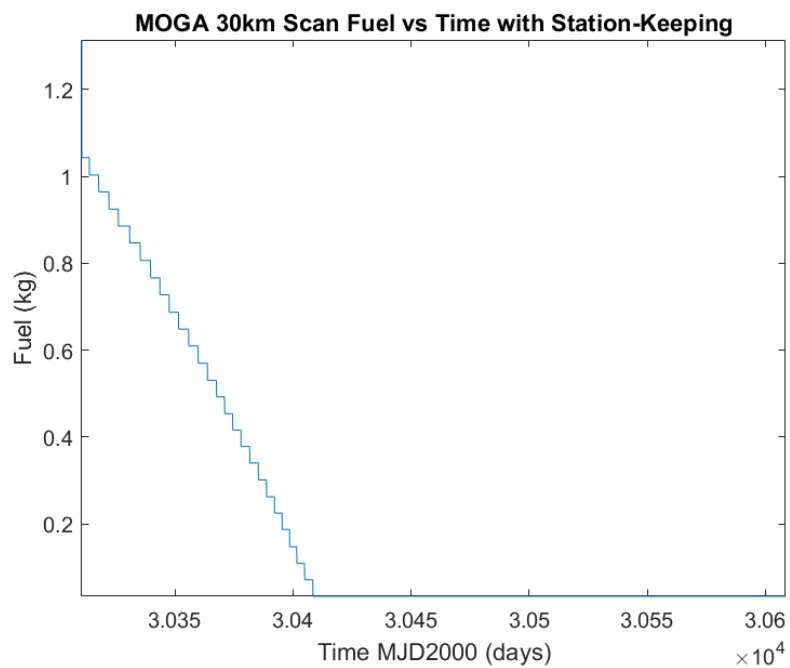
Figure 65: MOGA single-train best individual orbit fuel mass with stationkeeping over time
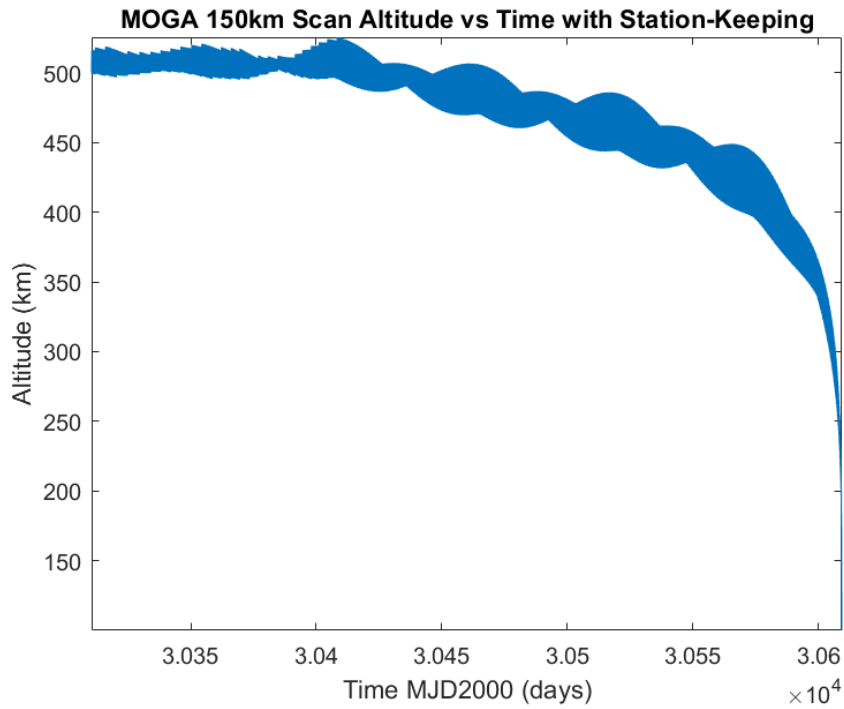
Figure 66: MOGA CMWS best individual orbit altitude with stationkeeping over time
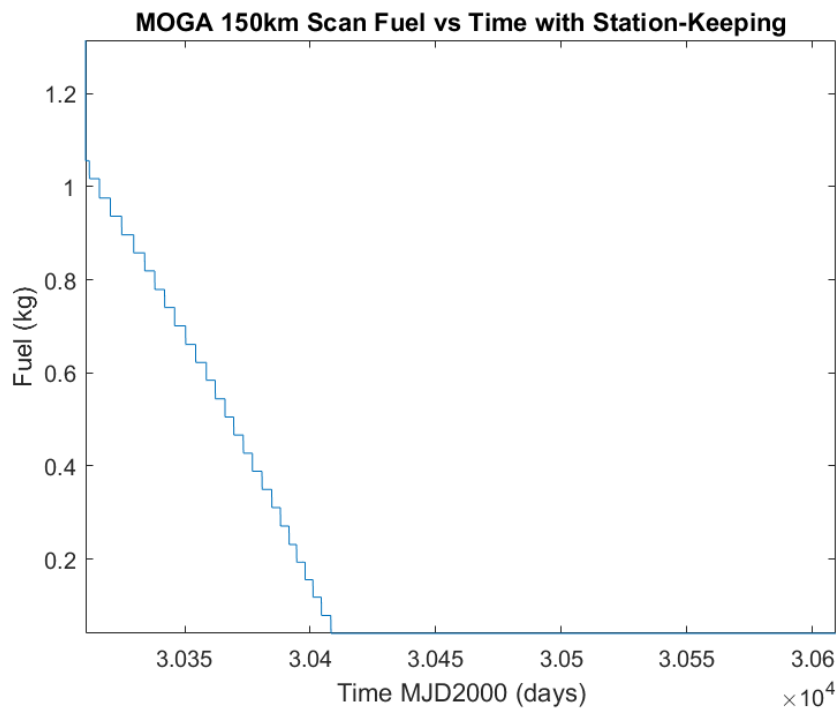
Figure 67: MOGA CMWS best individual orbit fuel mass with stationkeeping over time

Appendix B

Other Single-Train Pareto Plots

Inclination Difference vs Area Covered Single-Train
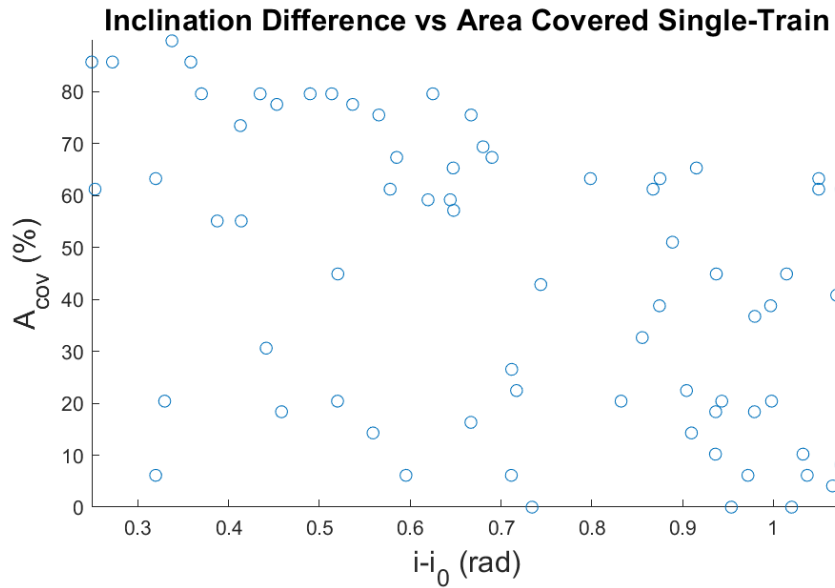
Figure 68: Plot of inclination difference vs area coverage for single-train configuration 30km swath scan mode

Number of Planes vs Area Covered Single-Train
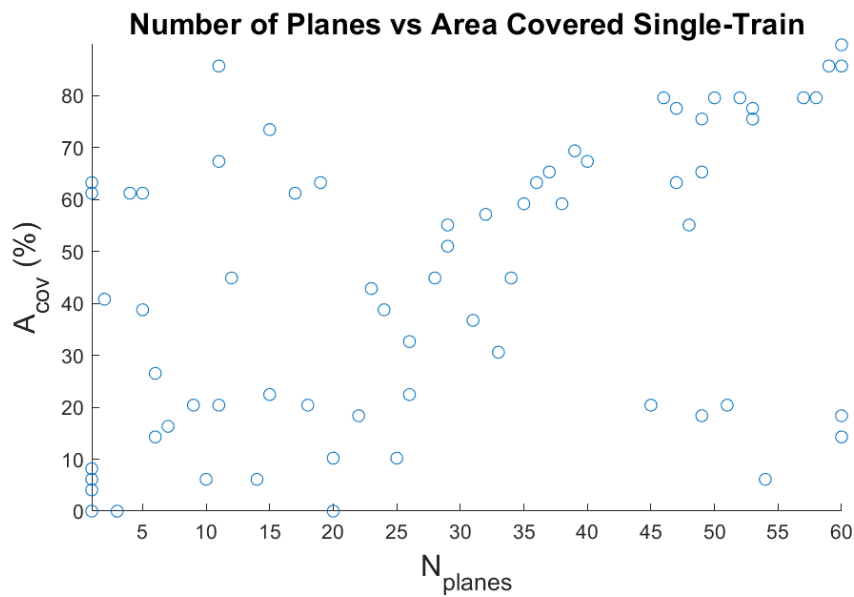
Figure 69: Plot of number of planes vs area covered for single-train configuration 30km swath scan mode
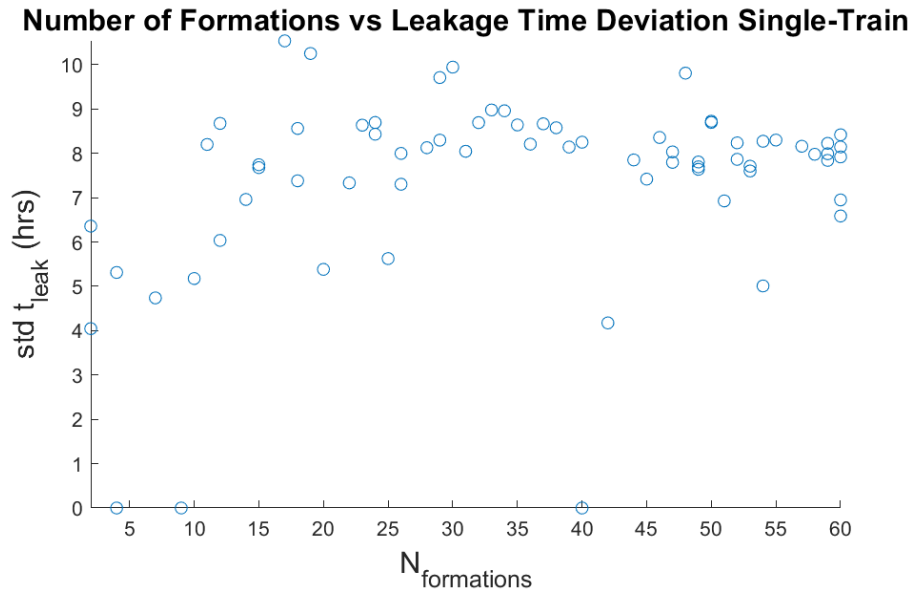
Figure 70: Plot of number of formations vs leakage time for single-train configuration 30km swath scan mode
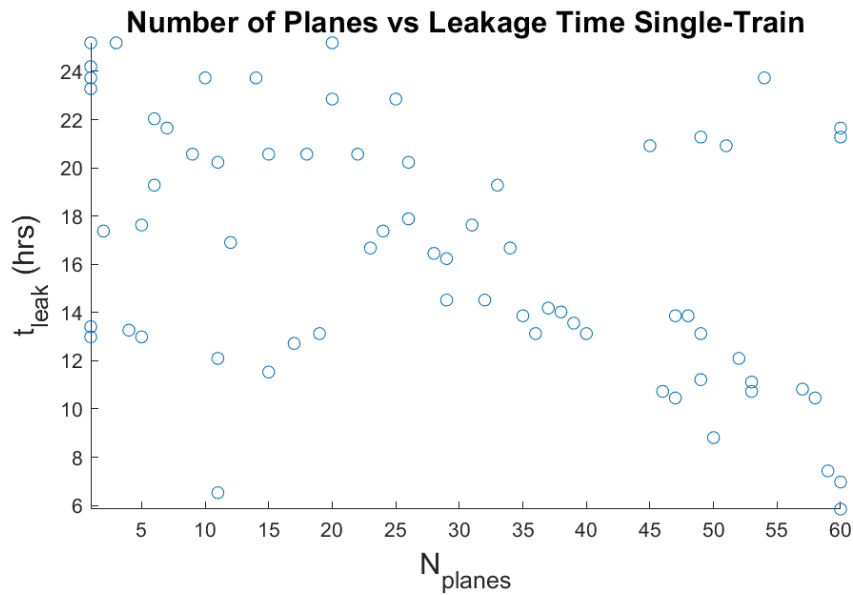
Figure 71: Plot of number of planes vs leakage time for single-train configuration 30km swath scan mode

Other CMWS Pareto Plots
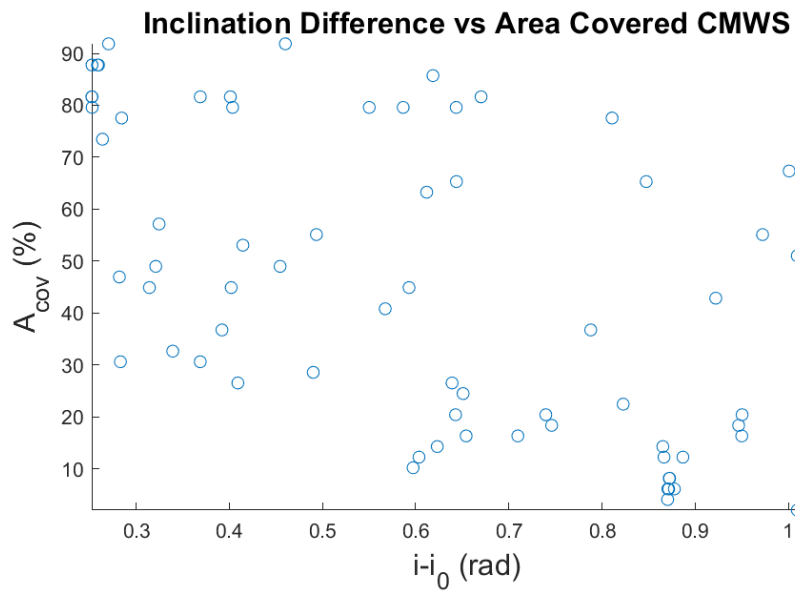
Figure 72: Plot of inclination difference vs area coverage for single-train configuration 150km swath scan mode
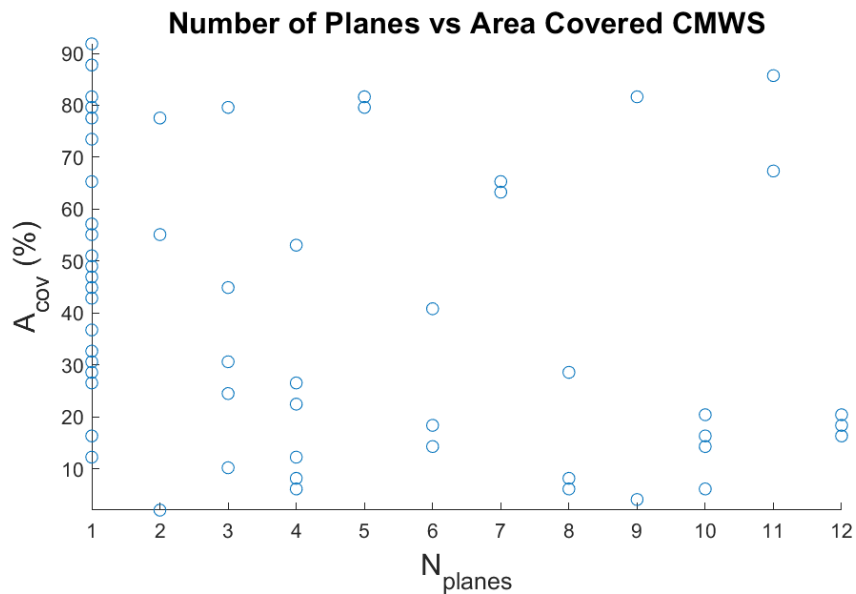
Figure 73: Plot of number of planes vs area covered for single-train configuration 150km swath scan mode
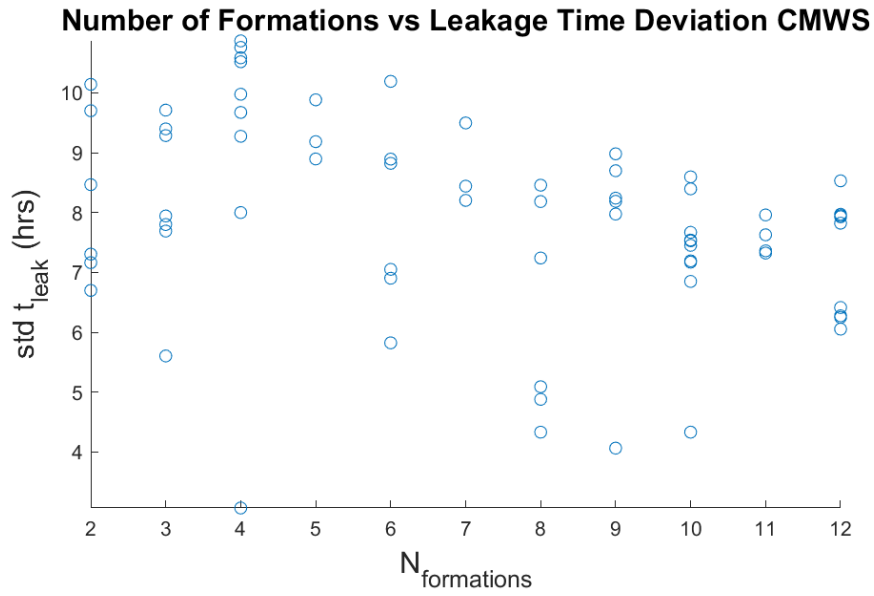
Figure 74: Plot of number of formations vs leakage time for single-train configuration 150km swath scan mode
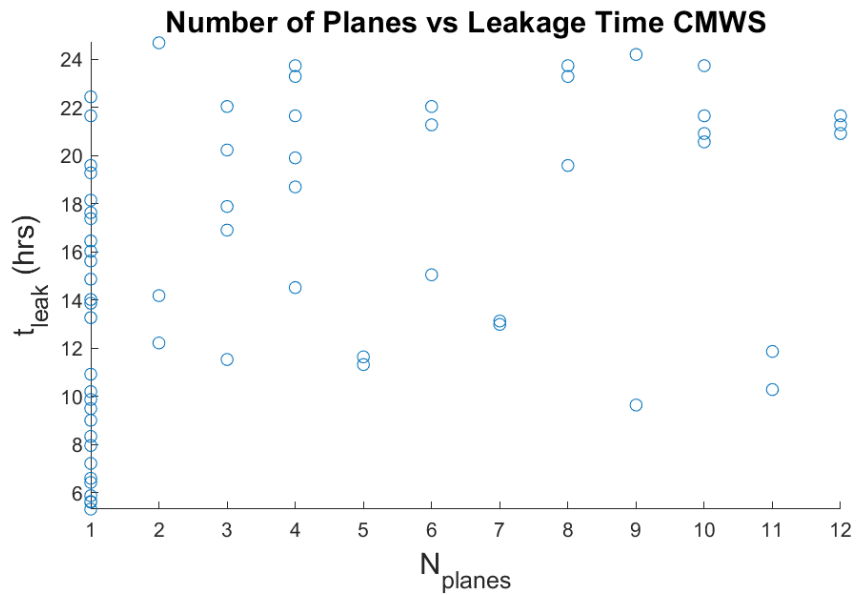
Figure 75: Plot of number of planes vs leakage time for single-train configuration 150km swath scan mode

Other Search Mode Pareto Plots
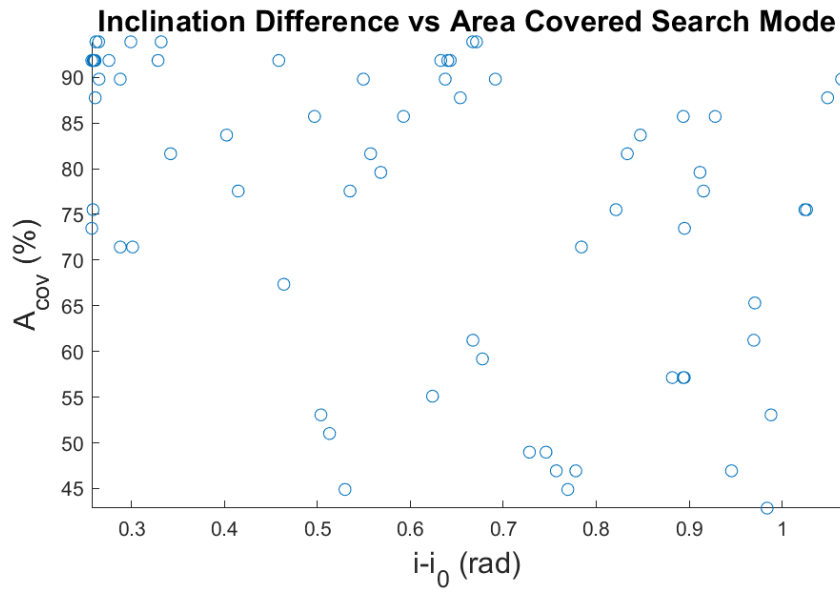
Figure 76: Plot of inclination difference vs area coverage for search mode
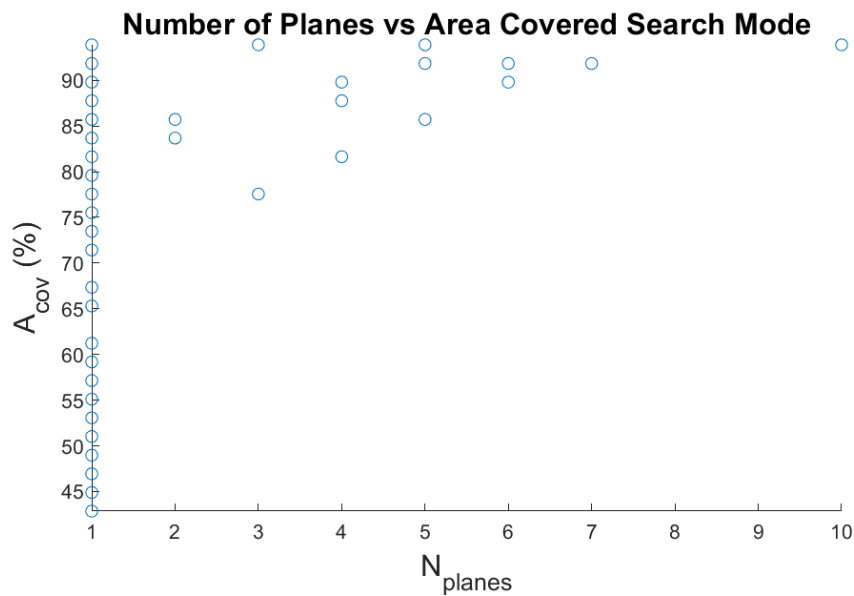
Figure 77: Plot of number of planes vs area covered for search mode

Figure 78: Plot of number of formations vs leakage time for search mode

Figure 79: Plot of number of planes vs leakage time for search mode

Acknowledgements

References

[1] Informationstechnische Gesellschaft im VDE et al. "Proceedings of EUSAR 2016 : 11th European Conference on Synthetic Aperture Radar : 6-9 June 2016." In: ().

[2] Davide Giudici et al. "Compact and Free-Floating Satellite MIMO SAR Formations". In: *IEEE Transactions on Geoscience and Remote Sensing* 60 (2022), pp. 1–12. ISSN: 0196-2892. DOI: 10.1109/TGRS.2021.3062973.

[3] Davide Giudici et al. "An Iso-Frequency MIMO SAR Formation for Wide-Swath Imaging, Interferometry and Tomography". In: *IEEE National Radar Conference - Proceedings* 2020-September (Sept. 2020). ISSN: 10975659. DOI: 10.1109/RADARCONF2043947.2020.9266637.

[4] Maximilian Rodger and Raffaella Guida. "Classification-aided sar and ais data fusion for space-based maritime surveillance". In: *Remote Sensing* 13 (1 Jan. 2021), pp. 1–26. ISSN: 20724292. DOI: 10.3390/rs13010104.

[5] I. A. Courie et al. "Preliminary Design of Imaging Microsatellite for Preventing Illegal Fishing in Indonesia". In: vol. 284. Institute of Physics Publishing, May 2019. DOI: 10.1088/1755-1315/284/1/012042. URL: https://iopscience.iop.org/article/10.1088/1755-1315/284/1/012042/pdf#:~:text=A%20constellation%20of%20imaging%20microsatellite,Indonesia%20during%2024%20hours%20duration..

[6] Kai Xie et al. "LEO space-based radar constellation design using a genetic algorithm". In: *CIE International Conference of Radar Proceedings* (2006). DOI: `10.1109/ICR.2006.343500`.

[7] Peng Zong and Saeid Kohani. "Optimal satellite LEO constellation design based on global coverage in one revisit time". In: *International Journal of Aerospace Engineering* 2019 (2019). ISSN: 16875974. DOI: `10.1155/2019/4373749`.

[8] Xueying Wang et al. "Satellite constellation design with genetic algorithms based on system performance". In: *Journal of Systems Engineering and Electronics* 27 (2 Apr. 2016), pp. 379–385. ISSN: 16711793. DOI: `10.1109/JSEE.2016.00039`.

[9] J. G. Walker. "Satellite Constellations". In: *Journal of the British Interplanetary Society* 37 (Dec. 1984), p. 559.

[10] Tania Savitri et al. "Satellite Constellation Orbit Design Optimization with Combined Genetic Algorithm and Semianalytical Approach". In: *International Journal of Aerospace Engineering* 2017 (2017). ISSN: 16875974. DOI: `10.1155/2017/1235692`.

[11] Andrea Monti Guarnieri. *Electromagnetic Imaging.* 1st ed. Vol. 1. Politecnico di Milano, Oct. 2015, pp. 149–150.

[12] Claude E. Shannon. "Communication in the Presence of Noise". In: *Proceedings of the IRE* 37 (1 1949), pp. 10–21. ISSN: 00968390. DOI: `10.1109/JRPROC.1949.232969`.

[13] Andrea Monti Guarnieri. "Adaptive removal of azimuth ambiguities in SAR images". In: *IEEE Transactions on Geoscience and Remote Sensing* 43 (3 Mar. 2005), pp. 625–633. ISSN: 01962892. DOI: `10.1109/TGRS.2004.842476`.

[14] Bordoni Federica et al. "Performance Investigation on the High-Resolution Wide-Swath SAR System with Monostatic Architecture". In: EUSAR 2010, 2010.

[15] J. Castillo, M. Younis, and G. Krieger. "A HRWS SAR system design with multi-beam imaging capabilities". In: *European Microwave Week 2017: "A Prime Year for a Prime Event", EuMW 2017 - Conference Proceedings; 14th European Microwave Conference, EURAD 2017* 2018-January (June 2017), pp. 179–182. DOI: `10.23919/EURAD.2017.8249176`.

[16] Song Yuepeng and Yang Ruliang. "High resolution, wide swath SAR using sub-aperture sub-band technique". In: *CIE International Conference of Radar Proceedings* (2007). DOI: `10.1109/ICR.2006.343529`.

[17] G Krieger et al. "Advanced Concepts for High-Resolution Wide-Swath SAR Imaging". In: 2010, pp. 1–4.

[18] G. Krieger, N. Gebert, and A. Moreira. "Unambiguous SAR Signal Reconstruction From Nonuniform Displaced Phase Center Sampling". In: *IEEE Geoscience and Remote Sensing Letters* 1 (4 Oct. 2004), pp. 260–264. ISSN: 1545-598X. DOI: `10.1109/LGRS.2004.832700`. URL: `https://ieeexplore.ieee.org/stamp/stamp.jsp?tp=&arnumber=1347118`.

[19] Menon. Ajay. *What Are Coaster Vessels?* Sept. 2020. URL: `https://www.marineinsight.com/types-of-ships/what-are-coaster-vessels/`.

[20] Nathan A. Miller et al. "Identifying global patterns of transshipment behavior". In: *Frontiers in Marine Science* 5 (JUL July 2018). ISSN: 22967745. DOI: `10.3389/FMARS.2018.00240/PDF`.

[21]   Work. R.O. "Small Combat Ships and the Future of the Navy". In: *Issues in Science and Technology* 21 (1 2004). URL: https://issues.org/work/.

[22]   Kulshreshtha. M. *Modern era of naval warfare with Corvettes*. Dec. 2021. URL: https://www.financialexpress.com/defence/modern-era-of-naval-warfare-with-corvettes/2390729/.

[23]   Brimelow. B. *Russia's Navy Is Betting Big on New, Smaller Warships With Missiles*. Apr. 2021. URL: https://www.businessinsider.com/russian-navy-betting-big-on-new-smaller-warships-with-missiles-2021-4?r=US&IR=T.

[24]   P.D.L. Williams, H.D. Cramp, and Kay Curtis. "Experimental study of the radar cross-section of maritime targets". In: *IEE Journal on Electronic Circuits and Systems* 2 (4 1978). ISSN: 03086984. DOI: 10.1049/ij-ecs.1978.0026.

[25]   Di Giacomo. F. and Cook. H. *Mediterranean Human Trafficking and Exploitation Prevalence Survey: IOM | International Organization for Migration*. 2016. URL: https://www.iom.int/news/mediterranean-human-trafficking-and-exploitation-prevalence-survey-iom.

[26]   Pulin. K. *The Mediterranean route: A dream for a better life destroyed by human trafficking - Humanium*. Nov. 2021. URL: https://www.humanium.org/en/the-mediterranean-route-a-dream-for-a-better-life-destroyed-by-human-trafficking/.

[27]   Vulperhorst. V. *The Mediterranean: Illegal fishing in our backyard? | Oceana Europe*. July 2018. URL: https://europe.oceana.org/en/blog/mediterranean-illegal-fishing-our-backyard.

[28]   Holland. J. *NGO: Illegal fishing potentially rife in the Mediterranean | SeafoodSource*. July 2019. URL: https://www.seafoodsource.com/news/environment-sustainability/ngo-illegal-fishing-potentially-rife-in-the-mediterranean.

[29]   RFE/RL. *Six Russian Warships Sailing From Mediterranean To Black Sea For Drills*. Feb. 2022. URL: https://www.rferl.org/a/russia-warships-black-sea-ukraine/31692995.html.

[30]   Sutton. H.I. *Unusual Russian Navy Concentration Seen In Eastern Mediterranean - Naval News*. Feb. 2022. URL: https://www.navalnews.com/naval-news/2022/02/unusual-russian-navy-concentration-seen-in-eastern-mediterranean/.

[31]   Aguttes. J-P. "Formations orientées le long du trajet de satellites SAR". June 2003. URL: https://patents.google.com/patent/EP1369704A1/en.

[32]   Krieger Gerhard et al. "Advanced Concepts for High-Resolution Wide-Swath SAR Imaging". In: EUSAR 2018, 2010.

[33]   TEC-SYE et al. *Concurrent Design Facility Studies Standard Margin Philosophy Description*. ESA, Sept. 2017, pp. 10–10.

[34]   NASA Ames Office of the Chief Engineer. *Space Flight System Design and Environmental Test*. NASA, Dec. 2018. URL: https://www.nasa.gov/sites/default/files/atoms/files/std8070.1.pdf.

[35]   Rennich. P., Wye. L., and Lee. S. *SRI CubeSat Imaging Radar for Earth Science (SRI-CIRES): Initial Flight Demonstrations*. Apr. 2019. URL: http://mstl.atl.calpoly.edu/~workshop/archive/2019/Spring/Day%202/Session%201/PatrickRennich.pdf.

[36] Wye. L. *SRI CubeSat Imaging Radar for Earth Science (SRI-CIRES)*. June 2015.

[37] ESA. *NovaSAR-S*. 2022. URL: https://earth.esa.int/web/eoportal/satellite-missions/n/novasar-s.

[38] SSTL and NRSC. *NovaSAR Data Product Specifications and Format*. Aug. 2021. URL: https://bhoonidhi.nrsc.gov.in/imgarchive/bhoonidhi_videos_help/NOVASAR_PRODUCT_FORMAT_DOCUMENT_V2.pdf.

[39] Capella Space. *Capella Space Homepage*. Mar. 2022. URL: https://www.capellaspace.com/.

[40] Capella Space Proprietary. *CAPELLA SPACE SAR IMAGERY PRODUCTS GUIDE*. June 2020. URL: http://www.edpmedia.com/assets/Capella_Space_SAR_Imagery_Products_Guide.pdf.

[41] ICEYE. *ICEYE SAR Product Guide*. Dec. 2021. URL: https://www.iceye.com/hubfs/Downloadables/ICEYE_SAR_Product_Guide.pdf.

[42] ICEYE. *ICEYE Tasking Imaging Modes*. 2022. URL: https://www.iceye.com/hubfs/Downloadables/ICEYE_Tasking_Imaging_Products.pdf.

[43] ESA. *Geographical Coverage - Sentinel-1 - Sentinel Online - Sentinel Online*. 2022. URL: https://sentinels.copernicus.eu/web/sentinel/missions/sentinel-1/satellite-description/geographical-coverage.

[44] ESA. *Copernicus: Sentinel-1*. 2022. URL: https://earth.esa.int/web/eoportal/satellite-missions/c-missions/copernicus-sentinel-1.

[45] Martin Cohen et al. "NovaSAR-S low cost spaceborne SAR payload design, development and deployment of a new benchmark in spaceborne radar". In: IEEE, May 2017, pp. 0903–0907. ISBN: 978-1-4673-8823-8. DOI: 10.1109/RADAR.2017.7944331.

[46] Hudson. B. *Synthetic Aperture Radar Concept of Operations*. OpenSourceSatellite.org, July 2021, pp. 17–17. URL: https://www.opensourcesatellite.org/downloads/KS-DOC-01202-01_OSSAT_SAR_CONOPs.pdf.

[47] Werner. D. *QA | ICEYE achieves the 'impossible' with miniature radar satellite*. May 2018. URL: https://spacenews.com/qa-iceye-achieves-the-impossible-with-miniature-radar-satellite/.

[48] Kulu. E. *What is a CubeSat other picosatellites*. Mar. 2022. URL: https://www.nanosats.eu/cubesat.

[49] Svarc. J. *Most Powerful Solar Panels 2022*. Mar. 2022. URL: https://www.cleanenergyreviews.info/blog/most-powerful-solar-panels.

[50] Clark.C. and Logan.R. *Power Budgets for Mission Success*. Apr. 2011.

[51] Doerry.A.W. *SAR data collection and processing requirements for high quality coherent change detection*. Sandia National Laboratories, Sept. 2008, pp. 8–8.

[52] Laurila. P. *ICEYE SAR Videos Published: Technical Insights and Highlights*. Mar. 2020. URL: https://www.iceye.com/blog/iceye-sar-videos-published-technical-insights-and-highlights.

[53] VACCO. *VACCO Micro Propulsion Systems*. 2018. URL: https://www.cubesat-propulsion.com/wp-content/uploads/2018/09/VACCO-Micro-Propulsion-Systems-Summary-web2-Sept2018.pdf.

[54]   Cardin. J. and Day. C. *A Standard Micro Propulsion System for CubeSats*. 2020. URL: http://mstl.atl.calpoly.edu/~workshop/archive/2020/Spring/6-Subsystems/ChrisDay.pdf.

[55]   ESA. *Sentinel Online: SAR Instrument*. Mar. 2022. URL: https://sentinels.copernicus.eu/web/sentinel/technical-guides/sentinel-1-sar/sar-instrument.

[56]   Quinn. G.M. "A New X-Band Satellite Groundstation for Remote Sensing". In: Australian International Aerospace Conference, July 2003, pp. 4–4.

[57]   Maiwal. V. et al. *DLR Feasibility Study SolmeX (Solar Magnetism Explorer) - CE Study Report*. DLR, Nov. 2010.

[58]   Tao Wu et al. "Features of X-band radar backscattering simulation based on the ocean environmental parameters in China offshore seas". In: *Sensors (Switzerland)* 18 (8 Aug. 2018). ISSN: 14248220. DOI: 10.3390/s18082450. URL: file:///C:/Users/k2/Downloads/x_band_clutter_sensors-18-02450-v2.pdf.

[59]   Momentus Inc. *Momentus Space Services*. Mar. 2022. URL: https://momentus.space/services/.

[60]   SpaceX. *Falcon User's Guide*. Sept. 2021. URL: https://www.spacex.com/media/falcon-users-guide-2021-09.pdf.

[61]   Itu Radiocommunication Bureau. *Nomenclature of the frequency and wavelength bands used in telecommunications V Series Vocabulary and related subjects*. International Telecommunications Union, Aug. 2015. URL: http://www.itu.int/ITU-R/go/patents/en.

[62]   NRAO. *RFI at X-Band (8-12 GHz) — Science Website*. 2022. URL: https://science.nrao.edu/facilities/vla/observing/RFI/X-Band.

[63]   Zhang. Y. et al. "User-Oriented Energy- and Spectral- Efficiency Tradeoff for Wireless Networks". In: *KSII Transactions on Internet and Information Systems* 7 (2 Feb. 2013), pp. 216–233. ISSN: 19767277. DOI: 10.3837/tiis.2013.02.003. URL: http://itiis.org/digital-library/manuscript/478.

[64]   Manish Varun Yadav, Sudeep Baudha, and Sri Charan Singam. "Multiple Slot Planar Antenna for X-Band Satellite Mobile Communication". In: IEEE, Nov. 2020, pp. 1–4. ISBN: 978-1-6654-0373-3. DOI: 10.1109/UPCON50219.2020.9376539.

[65]   Son Xuat Ta et al. "Planar circularly polarized X-band array antenna with low sidelobe and high aperture efficiency for small satellites". In: *International Journal of RF and Microwave Computer-Aided Engineering* 29 (11 Nov. 2019). ISSN: 1096-4290. DOI: 10.1002/mmce.21914.

[66]   Kyei Anim et al. "High-Efficiency Broadband Planar Array Antenna with Suspended Microstrip Slab for X-Band SAR Onboard Small Satellites". In: *Sensors* 22 (1 Dec. 2021), p. 252. ISSN: 1424-8220. DOI: 10.3390/s22010252.

[67]   Eberhard Gill and Hartmut Runge. "Tight formation flying for an along-track SAR interferometer". In: *Acta Astronautica* 55 (3-9 Aug. 2004), pp. 473–485. ISSN: 00945765. DOI: 10.1016/j.actaastro.2004.05.044.

[68]   A. MONTERO MIÑÁN. "Continuous-time control of multiple-satellite formations using mean relative orbital elements". Politecnico di Milano, July 2021.

[69]   S. Huang, C. Colombo, and F. Bernelli-Zazzera. "Multi-criteria design of continuous global coverage Walker and Street-of-Coverage constellations through property assessment". In: *Acta Astronautica* 188 (Nov. 2021), pp. 151–170. ISSN: 0094-5765. DOI: 10.1016/J.ACTAASTRO.2021.07.002. URL: https://www.sciencedirect.com/science/article/pii/S0094576521003490.

[70]   R. DAVID LUDERS. "Satellite Networks for Continuous Zonal Coverage". In: *https://doi.org/10.25* 31 (2 Feb. 1961), pp. 179–184. DOI: 10.2514/8.5422. URL: https://arc.aiaa.org/doi/pdf/10.2514/8.5422.

[71]   Saeid Kohani and Peng Zong. "LEO constellation design for regional coverage based on the safety of van allen belt radiation". In: *Journal of Space Safety Engineering* 5 (3-4 Sept. 2018), pp. 203–208. ISSN: 2468-8967. DOI: 10.1016/J.JSSE.2018.10.001. URL: https://www.sciencedirect.com/science/article/pii/S2468896718300521.

[72]   Jinyoung Shin et al. "Design of Regional Coverage Low Earth Orbit (LEO) Constellation with Optimal Inclination". In: *Journal of Astronomy and Space Sciences* 38 (4 2021), pp. 217–227. ISSN: 20931409. DOI: 10.5140/JASS.2021.38.4.217. URL: http://koreascience.or.kr/article/JAKO202101961791796.pdf.

[73]   I Meziane-Tani et al. *Optimization of small satellite constellation design for continuous mutual regional coverage with multi-objective genetic algorithm.* 2016. DOI: https://dx.doi.org/10.1080/18756891.2016.1204112. URL: https://hal.archives-ouvertes.fr/hal-01347277.

[74]   Yuri Ulybyshev. "Satellite constellation design for complex coverage". In: *Journal of Spacecraft and Rockets* 45 (4 2008), pp. 843–849. ISSN: 15336794. DOI: 10.2514/1.35369. URL: https://www.researchgate.net/publication/234368325_Satellite_Constellation_Design_for_Complex_Coverage.

[75]   Reza Zardashti and Shiva Emami. "Spatial geometry design of a low earth orbit constellation for iranian regional navigation satellite system". In: *Journal of Aerospace Technology and Management* 13 (2021). ISSN: 21759146. DOI: 10.1590/jatm.v13.1215. URL: https://www.scielo.br/j/jatm/a/gs44FgMDg8kS3LjJVwkqdPk/?format=pdf&lang=en.

[76]   Andrew E. Turner. "Constellation design using walker patterns". In: *AIAA/AAS Astrodynamics Specialist Conference and Exhibit* (2002). DOI: 10.2514/6.2002-4636. URL: https://arc.aiaa.org/doi/abs/10.2514/6.2002-4636.

[77]   Jintao Liang, Aizaz U. Chaudhry, and Halim Yanikomeroglu. "Phasing Parameter Analysis for Satellite Collision Avoidance in Starlink and Kuiper Constellations". In: (Sept. 2021).

[78]   Heavens-Above.com. *SENTINEL 1B - Orbit.* 2022. URL: https://www.heavens-above.com/orbit.aspx?satid=41456.

[79]   N2YO.com. *SENTINEL 1B Satellite details 2016-025A NORAD 41456.* 2022. URL: https://www.n2yo.com/satellite/?s=41456.

[80]   GMES Sentinel-1 Team. *GMES Sentinel-1 System Requirements Document.* ESA, Mar. 2009, pp. 19–20.

[81]   Howard D Curtis et al. *Orbital Mechanics for Engineering Students Third Edition Butterworth-Heinemann is an imprint of Elsevier.*

[82] David Mostaza Prieto, Benjamin P. Graziano, and Peter C.E. Roberts. "Spacecraft drag modelling". In: *Progress in Aerospace Sciences* 64 (Jan. 2014), pp. 56–65. ISSN: 0376-0421. DOI: 10.1016/J.PAEROSCI.2013.09.001. URL: https://www.sciencedirect.com/science/article/abs/pii/S0376042113000754?via3Dihub.

[83] ESA. *Capella X-SAR*. 2022. URL: https://directory.eoportal.org/web/eoportal/satellite-missions/content/-/article/capella-x-sar.

[84] Marita Markkula. *ICEYE: Hightlights of 2021*. Dec. 2021. URL: https://www.iceye.com/blog/highlights-of-2021#.

[85] Faber. J. et al. *Regulated Slow Steaming in Maritime Transport: An Assessment of Options, Costs and Benefits*. CE Delft, Feb. 2012, pp. 59–59. URL: https://www.transportenvironment.org/wp-content/uploads/2021/07/Slow%20steaming%20CE%20Delft%20final.pdf.

[86] Vrajitoru.D. *Large Population or Many Generations for Genetic Algorithms? Implications in Information Retrieval*. University of Neuchatel,EPFL. URL: https://www.cs.iusb.edu/~danav/papers/LargePop.pdf.

[87] Hang Woon Lee et al. "A Semi-Analytical Approach to Satellite Constellation Design for Regional Coverage". In: Mar. 2018.

[88] S. Suffian, R. Dzombak, and Khanjan Mehta. "Future directions for nonconventional and vernacular material research and applications". In: *Nonconventional and Vernacular Construction Materials: Characterisation, Properties and Applications* (Jan. 2020), pp. 63–80. DOI: 10.1016/B978-0-08-102704-2.00003-2.

[89] Ranajeet Mohanty, Shakti Suman, and Sarat Kumar Das. "Modeling the Axial Capacity of Bored Piles Using Multi-Objective Feature Selection, Functional Network and Multivariate Adaptive Regression Spline". In: *Handbook of Neural Computation* (Jan. 2017), pp. 295–309. DOI: 10.1016/B978-0-12-811318-9.00016-8.

[90] MarineTraffic.com. *MarineTraffic: Global Ship Tracking Intelligence | AIS Marine Traffic*. URL: https://www.marinetraffic.com/en/ais/details/ships/shipid:6407591/mmsi:229862000/imo:9851086/vessel:FRAMURA.

[91] ESA. *ESA - Mitigating space debris generation*. 2022. URL: https://www.esa.int/Safety_Security/Space_Debris/Mitigating_space_debris_generation.

[92] NASA. *General Mission Analysis Tool (GMAT) v.R2016a(GSC-17177-1) | NASA Software Catalog*. 2016. URL: https://software.nasa.gov/software/GSC-17177-1.

[93] ESA. *ICEYE-X1*. Mar. 2022. URL: https://directory.eoportal.org/web/eoportal/satellite-missions/i/iceye-x1.

[94] Lawler. R. *After Sending 2 'Doves' Into Orbit, Planet Labs Prepares Largest Satellite Constellation For Launch*. Nov. 2013. URL: https://techcrunch.com/2013/11/26/planet-labs-flock-1/.

[95] Alexander Reissner. "The IFM 350 Nano Thruster - Introducing very high Δv Capabilities for Nanosats and Cubesats". In: American Institute of Aeronautics and Astronautics, July 2016. ISBN: 978-1-62410-406-0. DOI: 10.2514/6.2016-5044.

[96]   Donald J Kessler et al. "THE KESSLER SYNDROME: IMPLICATIONS TO FU-
        TURE SPACE OPERATIONS". In: *Advances in the Astronautical Sciences* 137
        (2010). URL: https://aquarid.physics.uwo.ca/kessler/Kessler%20Syndrome-
        AAS%20Paper.pdf.